Characterisation of Single Biomolecules With Optoplasmonic Resonators

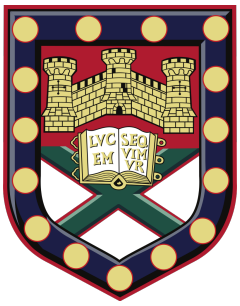

Submitted by **Serge Mathieu Vincent** to the University of Exeter
as a thesis for the degree of
Doctor of Philosophy in Physics

I certify that all material in this thesis which is not my own work has been identified and that no material has previously been submitted and approved for the award of a degree by this or any other University.

Signature: Serge Vincent

Digitally signed by Serge Vincent
DN: cn=Serge Vincent, o=University of Exeter, ou=Living Systems Institute, email=sv316@exeter.ac.uk, c=NL
Date: 2020.10.16 09:21:35 +02'00'

October 2020

To my loving partner, Evie.
You are all my reasons.

Acknowledgements

Countless things have changed over the course of my PhD journey. There were triumphs, there were tragedies, and the whole spectrum of emotion was felt. A diamond forms under pressure, however, and so this degree provided an opportunity for me to solidify my identity. Firstly I would like to thank my supervisor, Frank Vollmer, for supporting me during my research. He gave me the space to pursue my own ends and the tools to do so without financial hindrance. I believe the ambition of my projects was carried out with diligence and, although some questions remain unanswered, this thesis successfully pushes beyond the boundaries of scientific knowledge. With this in mind, I am grateful for his enthusiasm and mentorship.

The endeavours summarised here were also carried out in two places: the Max Planck Institute for the Science of Light in Erlangen, Germany and the Living Systems Institute at the University of Exeter in England. I consider myself privileged to have enjoyed working in both of these settings, as they offered fond memories and staged plentiful, stimulating conversations. To my fellow colleagues, Sivaraman Subramanian, Simona Frustaci, Narima Eerqing, Callum Jones, Aneeth Kakkanattu Arunkumar, Katya Zossimova, Ying-Jen Chen, Martin Baaske, Eugene Kim, Ali Mahdavi, Jolly Xavier, Hsin-Yu Wu, Rithvik Gutha, Gema Cabello, Deshui Yu, Monika Pietrzyk, Nikita Toropov, Samir Vartabi Kashanian, Keisuke Watanabe, Tom Constant, Arturo Bianchetti, Mariana Serrano, Matias Rafti, Fabian Meder, Matthew Foreman, Tobias Zech, Paul Roth, Silvan Englisch, Ulrike Schöler, and Roman Guliaev, I value each and every social/academic interaction we've had as they were enriching. I must also thank our collaborators, Peter Rakitzis, the ULTRACHIRAL team, Xin Jiang, Philip Russell, and Rémy Soucaille, who helped round out my research. You have all kept me focused in order for me to stay the course.

To my family and friends, near and far, I am fortunate to be close to so many precious individuals. You have reminded me to stay grounded and to be mindful. It is because of you that I have embraced my curiosity and followed my passion to explore the unknown. I am truly blessed to have such kind, considerate pseudo-parents in Mark and Fiona. My heart goes out to my parents, Daniel and Marie-Antoinette, and grand-père, Bernard, who have suffered a great deal of hardship over these past $\sim$4 years. Especially for Gail, Melanie,

Denis, and Fernande, we will never forget. Rest assured that a day will come when we can put the losses of the past behind us to embrace the bright future that lies ahead. You've instilled patience and hope in me that has been indispensable during these uncertain times. We will bask in the sunlight again.

Last but not least, I dedicate this thesis to my other half, Evie. My life has transformed since we've met. I would never trade an alternate universe for the one in which we are together. You bring out my humanity and paint the world with colour. This vivid reality we share is a gift, which I am lucky Nick Gaunt encouraged me to find. Your courage and my wonder are one of many pairings that makes this relationship extraordinary. I love you dearly, now and always, and look forward to the endless adventures we have in store.

Abstract

Biomolecules can be detected through induced changes in the optical whispering-gallery mode (WGM) resonance in a circularly symmetric dielectric. The spatial and temporal confinement of light in a WGM is further complemented by coupling to the localised surface plasmons (LSPs) of metallic nanoparticles attached to the WGM resonator. LSP-WGM hybridisation allows for the optical readout of single-molecule surface reactions on gold nanoantennae, the mechanisms for which are not yet fully understood from a theoretical perspective. The specificity of this modality is, moreover, a subject of intense research. In this thesis, we propose three strategies for characterising molecules with light. The first strategy is a prototype polarimeter that differentiates chirality based on a signal-reversible Faraday effect in a magneto-optical WGM microcavity. Thermal tuning integrated into the resonator minimises geometrical birefringence, in turn maximising Faraday rotation to optimise chiral sensitivity. There we endeavour to resolve single-molecule chirality. Without engineering reconsiderations, however, the polarimeter is found to be limited to bulk chiral analysis. The second strategy is an (optoplasmonic) LSP-WGM resonator with chiral gold nanoantennae. Signals from the molecules conjointly show a correlation with the molecular weight and diffusivity of detected DL-cysteine and poly-DL-lysine. Aside from these features, the sensing site heterogeneity on the chiral gold nanoparticles impedes chiral discrimination. The third strategy is a novel reaction scheme adapted to the optoplasmonic sensor. Aminothiol linkers functionalise the gold surface via amine-gold anchoring, setting up cyclical interactions with thiolated analytes by thiol/disulfide exchange. Unexpected perturbations in the LSP-WGM resonance are observed, such as linewidth oscillation without resonance shift attributed to optomechanical coupling between LSPs and the vibrational modes in a given analyte. This offers a new form of spectroscopy wherein single biomolecules could be characterised by their mass, size, and composition through monitoring secondary parameters of the optoplasmonic resonance.

Table of contents

List of figures

Chapter 1

Introduction

Molecules co-exist in a turbulent world. Harsher still, biomolecules are thrust in the middle of it as living systems shuffle to self-organise and self-replicate. Molecular machines perform intricate functions in this environment with precision and fidelity virtually unmatched by synthetic means. It can thus be difficult to imagine how meaningful information can be extracted from the simplest of compounds, such as amino acids, when they are subject to a constant state of flux. Signals may be relayed in a cell and a group of biomolecules could be whisked across vast potentials through a membrane protein, all the while succumbing to their innate molecular dynamics. A time-averaged measurement of a molecule's position, orientation, or conformation will wash out or become convolved with noise, like Brownian motion. Component atoms and their arrangement, namely symmetries, are obfuscated.

Multicellular life has thrived in the presence of light. Plants harvest energy through photosynthesis, while mammals can perceive the universe through photoreceptors and interconnections that link these to their visual cortex. Light also serves to decode nature's more hidden secrets, like the composition of stars through emission spectra or the structure of a cell nucleus through fluorescence imaging. Were it not for technologies that use light as vessel to transfer data throughout time and space, the evolution of humankind would be altogether alien. It is therefore natural for us to posit light as a medium to characterise molecules.

The diffraction limit, however, sets a lower bound on what we can resolve using conventional optics. In 1873, the German physicist Ernst Abbe reasoned that light will converge to a spot with radius [1]:

$$d = \frac{\lambda}{2\mathrm{NA}} \tag{1.1}$$

in the lateral plane, where λ is the optical wavelength and NA is the numerical aperture. This means that we need to play a few technical tricks to discern spatial features beyond

diffraction. Innovations such as super-resolution fluorescence microscopy reliably bridged the gap to look at minuscule entities, as small as a single pentacene in a p-terphenyl crystal at liquid helium temperature [2]. Later on, super-resolution techniques proceeded to image cytoskeletal networks in cells [3] and single fluorescent molecules at room temperature [4]. Whether it is through stochastic optical reconstruction microscopy (STORM) [5] or photo-activated localisation microscopy (PALM) [6, 7], we can overcome the diffraction limit by exploiting photophysics in the way we turn on random subsets of fluorophores. It is also feasible to account for interference between the scattered light field $|E_s|$ from a single molecule and a background $|E_b|$, as in interferometric and plasmonic scattering microscopy (iSCAT [8] and PSM [9]). The interference term in either case is

$$2|E_b||E_s|\cos\beta \tag{1.2}$$

where the phase difference is β and the contrast has a cubic (rather than sextic) dependence on the particle diameter.

A loftier goal would be to map out the energy landscape of a molecule as it transitions between states. Instruments that measure these dynamics at room temperature, without chemical labelling, are few and tend to stop short of molecules in an ensemble [10, 11, 12]. There are force spectroscopy methods [13], such as those that add constraints via magnetic/electromagnetic tweezing [14, 15] or a contacting tip [16, 17, 18], which permit us to observe molecules contort under strain or torsional stress. Even so, blind questions like what the handedness of a particular glyceraldehyde is or, rather, what type of molecule is actually near a sensor's transducer, are often left unanswered. By building on earlier milestones [19, 20, 21, 22], this thesis strives to defy such limitations through optoplasmonics: the intersection between optical micro-resonators and plasmonic nano-resonators.

1.1 Overview of Thesis Chapters

The work presented in this thesis was carried out by the author in collaboration with colleagues from within and outside the research group. Each chapter is succinctly described here and, when relevant, an indication of the relative contributions is given.

Chapter 2 is a review of the physics behind optical microcavities and nanoplasmonics. The burgeoning field of optoplasmonics melds these two research areas together, and so we cover topics such as whispering-gallery modes, their analytical solutions for a dielectric sphere, mode confinement parameters, loss channels, nonlinear phenomena, mode splitting, and localised surface plasmon resonances.

Chapter 3 lays out schemes for single-molecule detection. Attention is devoted to optoplasmonic sensors consisting of a glass microcavity with a guided whispering-gallery mode coupled to plasmonic nanoantennae with localised surface plasmon resonances. Perturbations to the hybrid resonance due to biomolecular activity are quantitatively described, alongside hypothesised mechanisms for molecular characterisation and single-molecule event analysis.

Chapter 4 concerns techniques for measuring chirality. The Faraday effect, as it applies to whispering-gallery mode resonators and chiral polarimetry, is highlighted. An *Applied Physics Letters* publication on the intracavity Faraday effect in a soft-glass whispering-gallery mode microsphere with thermal tuning is included [23]. This was made possible with magneto-optical glasses and support from Dr. Xin Jiang in Prof. Philip Russell's group at the Max Planck Institute for the Science of Light. The paper and its experiments/simulations were completed by the thesis author.

Chapter 5 shows results for the optoplasmonic detection of single chiral molecules on chiral gold nanoantennae. The gold 432 helicoid III nanoparticles, first designed in another published study [24], were synthesised by Dr. Fabian Meder at the Istituto Italiano di Tecnologia. Transient interactions of single amino acids and polymers at the detection sites are inspected for a significant number of events (i.e. > 1,000 per trace) towards extracting molecular characteristics.

Chapter 6 puts forward a thiol/disulfide exchange pathway for regulating surface reactions on the gold nanoantennae of an optoplasmonic sensor. The signal response due to single thiolated perturbers exhibits hybrid resonance lifetime broadening and narrowing. These findings, which imply a specific coupling between localised surface plasmons of the nanoantennae and vibrational modes of the molecules, are reported in a *Nature Communications* publication [25]. The thesis author devised and conducted the experiments, while the data was interpreted with assistance from Sivaraman Subramanian in Prof. Frank Vollmer's group at the University of Exeter.

Chapter 7 summarises key aspects of the thesis, exchanging some closing thoughts and proposing prospective directions for the research.

Appendix A derives a full-vector finite-difference mode solver and then applies it to modelling the Faraday effect in magneto-optical WGM microcavities. Numerical outputs from this solver are found in Chapters 2 and 4.

Appendix B focuses on WGM microresonator fabrication using exotic cavity materials. The integration of a metallic conducting wire and the complications it brings in the context of glass crystallisation are discussed.

Chapter 2

Combining Optical Microcavities with Plasmonic Nanoparticles

2.1 Optical Whispering-Gallery Modes

Light has extraordinary potential to be captured in time and shrunken in space. Outside of the black holes in our universe, however, trapping optical energy is destined to be imperfect. What is instead typical is a degree of trapping parameterised by an electromagnetic field's mode volume V_m and quality factor Q. The size-dependent, resonant recirculation of light in a microscale cavity can be accomplished in several ways: through a Fabry-Pérot etalon, photonic crystal, or a whispering-gallery mode (WGM) resonator, among others. Coupling and manipulation of photons in an optical microcavity gives rise to rich physics, such as spontaneous emission surpression [26] or enhancement [27], low-threshold lasing [28], and strong-coupling cavity quantum electrodynamics [29]. In this section we will focus on the optical WGM: a guided mode at the periphery of what is usually an axially symmetric dielectric structure. A proper description of such resonances dates back to a 1910 paper written by Lord Rayleigh, wherein he describes the constructive interference of pressure waves guided by the interior gallery of St. Paul's Cathedral (i.e. depicted in Figure 2.1) in London, England [30]. Scientists soon explored this phenomenon in the optical domain, in spherical structures, many decades later [31, 32, 33, 34]. Theory for the optical analogue will be described here first, followed by the platforms developed thus far and their practical uses.

Figure 2.1: Whispering gallery in St. Paul's Cathedral. Acoustic waves at particular frequencies travel along the curved wall and are audible along the entire periphery. The above photograph is taken from [35].

2.1.1 Modal Structure and Solutions

The classical interpretation of light is that it is an electromagnetic wave. It consists of an oscillating electric field $\vec{E}$ and magnetic field $\vec{B}$ governed by Maxwell's equations. Separately, these equations are known as Faraday's law, Ampère's law, Gauss's law of electrostatics, and Gauss's law of magnetostatics:

$$\nabla \times \vec{E}(\vec{r},t) = -\frac{\partial \vec{B}(\vec{r},t)}{\partial t} \tag{2.1}$$

$$\nabla \times \vec{H}(\vec{r},t) = \vec{j}(\vec{r},t) + \frac{\partial \vec{D}(\vec{r},t)}{\partial t} \tag{2.2}$$

$$\nabla \cdot \vec{D}(\vec{r},t) = \rho(\vec{r},t) \tag{2.3}$$

$$\nabla \cdot \vec{B}(\vec{r},t) = 0 \tag{2.4}$$

with dependence on position $\vec{r}$ and time t. The respective electric and magnetic displacement vectors are $\vec{D} = \varepsilon_0 \varepsilon_r \vec{E}$ and $\vec{H} = \vec{B}/\mu_0$ (disregarding magnetic materials), the free current density is $\vec{j}$, the free charge density is ρ, the vacuum permittivity is $\varepsilon_0 = 8.85 \times 10^{-12}$ F/m,

the medium's relative permittivity is ε_r, and the vacuum permeability is $\mu_0 = 4\pi \times 10^{-7}$ H/m. The response of matter to an electromagnetic field is expressed by the constitutive relations

$$\vec{D}(\vec{r},t) = \varepsilon_0 \vec{E}(\vec{r},t) + \vec{P}(\vec{r},t) \tag{2.5}$$

$$\vec{H}(\vec{r},t) = \frac{1}{\mu_0}\vec{B}(\vec{r},t) - \vec{M}(\vec{r},t) \tag{2.6}$$

Polarisation $\vec{P} = \varepsilon_0 \chi_e \vec{E}$ and magnetisation $\vec{M} = \chi_m H$ relate to the electric susceptibility χ_e and magnetic susceptibility χ_m. We assume that $\chi_m = 0$ and hence $\vec{M} = \vec{0}$; however, for completeness, we note that $\chi_m > 0$ for paramagnetism and $\chi_m < 0$ for diamagnetism cases. The permittivity ε=$\varepsilon_0\varepsilon_r = \varepsilon_0(\chi_e + 1)$ will be further investigated later on as it is intimately tied to polarisability, i.e. the primary WGM sensing parameter, through the Clausius–Mossotti relation. In chiral media, the constitutive relations are complicated by cross-coupling terms:

$$\vec{D}(\vec{r},t) = \varepsilon \vec{E}(\vec{r},t) + i\chi_c \vec{H}(\vec{r},t) \tag{2.7}$$

$$\vec{B}(\vec{r},t) = \mu \vec{H}(\vec{r},t) - i\chi_c \vec{E}(\vec{r},t) \tag{2.8}$$

The chiral parameter χ_c has a real and imaginary part that represent optical rotary dispersion and circular dichroism, respectively. When free charges and currents are absent, equations (2.2) and (2.3) are simplified by $\rho = 0$ and $\vec{j} = \vec{0}$. By taking the curl of (2.1) and (2.2), utilising the vector identity $\nabla \times (\nabla \times \vec{\psi}) = \nabla(\nabla \cdot \vec{\psi}) - \nabla^2 \vec{\psi}$, then substituting in (2.3) and (2.4), one can obtain two vectorial Helmholtz equations

$$\nabla^2 \vec{E}(\vec{r},t) = \mu_0 \varepsilon_0 \varepsilon_r \frac{\partial^2 \vec{E}(\vec{r},t)}{\partial t^2} \tag{2.9}$$

$$\nabla^2 \vec{B}(\vec{r},t) = \mu_0 \varepsilon_0 \varepsilon_r \frac{\partial^2 \vec{B}(\vec{r},t)}{\partial t^2} \tag{2.10}$$

The refractive index $n = \sqrt{\varepsilon_r}$ (without loss) slows an electromagnetic wave's phase speed according to $v_p = \frac{1}{\sqrt{\mu_0 \varepsilon_0 \varepsilon_r}} = \frac{c}{\sqrt{\varepsilon_r}} = \frac{c}{n}$ where $c = 3.00 \times 10^8$ m/s is the vacuum speed of light. If attenuation is accounted for, the refractive index becomes complex with squared value

$$\tilde{n}^2 = (n + i\kappa)^2 \tag{2.11}$$

where $i = \sqrt{-1}$ and the imaginary part κ is referred to as the attenuation coefficient. In a spherical coordinate system, the Helmholtz equation $\nabla^2\vec{\psi} + k_0^2\varepsilon_r\vec{\psi} = 0$ takes the form

$$\frac{1}{r^2}\frac{\partial}{\partial r}\left(r^2\frac{\partial\vec{\psi}}{\partial r}\right) + \frac{1}{r^2\sin\theta}\frac{\partial}{\partial\theta}\left(\sin\theta\frac{\partial\vec{\psi}}{\partial\theta}\right) + \frac{1}{r^2\sin^2\theta}\frac{\partial^2\vec{\psi}}{\partial\phi^2} + k_0^2\varepsilon_r\vec{\psi} = 0 \tag{2.12}$$

with vacuum wavelength λ_0 and wavenumber $k_0 = 2\pi/\lambda_0$. By sequential separation of variables, we infer $|\vec{\psi}(r,\theta,\phi)| = R(r)V(\theta,\phi)$ from

$$\frac{\partial}{\partial r}\left(r^2\frac{\partial\vec{\psi}}{\partial r}\right) + k_0^2\varepsilon_r r^2\vec{\psi} = -\frac{1}{\sin\theta}\frac{\partial}{\partial\theta}\left(\sin\theta\frac{\partial\vec{\psi}}{\partial\theta}\right) - \frac{1}{\sin^2\theta}\frac{\partial^2\vec{\psi}}{\partial\phi^2} = \text{Constant} \tag{2.13}$$

The function $V(\theta,\phi) = \Theta(\theta)\Phi(\phi)$ then arises from further rearrangement:

$$V\sin^2\theta\left[\frac{1}{R}\frac{\partial}{\partial r}\left(r^2\frac{\partial R}{\partial r}\right) + k_0^2\varepsilon_r r^2\right] + \sin\theta\frac{\partial}{\partial\theta}\left(\sin\theta\frac{\partial V}{\partial\theta}\right) = -\frac{\partial^2 V}{\partial\phi^2} = \text{Constant} \tag{2.14}$$

One can glean that a WGM has the dependence $\Phi(\phi) = e^{\pm im\phi}$ along its propagation direction. In all, there are three separated formulae

$$\frac{\partial}{\partial r}\left(r^2\frac{\partial R}{\partial r}\right) + \left[k_0^2\varepsilon_r r^2 - l(l+1)\right]R = 0 \tag{2.15}$$

$$\frac{1}{\sin\theta}\frac{\partial}{\partial\theta}\left(\sin\theta\frac{\partial\Theta}{\partial\theta}\right) + \left[l(l+1) - \frac{m^2}{\sin^2\theta}\right]\Theta = 0 \tag{2.16}$$

$$\frac{\partial^2\Phi}{\partial\phi^2} + m^2\Phi = 0 \tag{2.17}$$

that allow us to define the integer m as the azimuthal mode number and integer l as the polar mode number. Analytical solutions to these equations are a linear combination $R(r) = A_l j_l(k_0\sqrt{\varepsilon_r}r) + B_l y_l(k_0\sqrt{\varepsilon_r}r)$ and associated Legendre polynomial $\Theta(\theta) = P_l^m(\cos\theta)$, where $l \geq m$. The spherical Bessel functions of the first kind j_l and second kind y_l, with coefficients A_l and B_l, multiplied by P_l^m construct the general eigenfunction

$$\psi_{N,l,m}(r,\theta,\phi) = \sum_l \left[A_l j_l(k_0\sqrt{\varepsilon_r}r) + B_l y_l(k_0\sqrt{\varepsilon_r}r)\right]P_l^m(\cos\theta)e^{\pm im\phi} \tag{2.18}$$

with radial mode number N derived from the zeros of the spherical Bessel functions. This last integer is imposed by the cavity's boundary conditions.

In pursuit of a tractable mode profile, we will choose to consider a spherically symmetric cavity. There are two polarisations under scalar approximation: the transverse electric (TE) mode $\psi(\vec{r}) = \vec{r}\cdot\vec{E}(\vec{r})$ and transverse magnetic (TM) mode $\psi(\vec{r}) = \vec{r}\cdot\vec{H}(\vec{r})$. The resulting

eigenmodes from Mie theory are

$$\psi_{N,l,m}(r,\theta,\phi) = \begin{cases} A j_l(k_c r) P_l^m(\cos\theta) e^{\pm im\phi}, & r \le a \\ B h_l(k_s r) P_l^m(\cos\theta) e^{\pm im\phi}, & r > a \end{cases} \tag{2.19}$$

These guided modes are composed of photons trapped by an effective radial potential and so are bounded by evanescent field regions. The characteristic equations that account for the permittivity discontinuity at the boundary are

$$\frac{\frac{\partial}{\partial(k_c a)}\left[(k_c a) j_l(k_c a)\right]}{j_l(k_c a)} - \frac{\frac{\partial}{\partial(k_s a)}\left[(k_s a) h_l(k_s a)\right]}{h_l(k_s a)} = 0 \quad \text{for } \vec{r}\cdot\vec{E}(\vec{r}) = 0 \tag{2.20}$$

$$\frac{\frac{\partial}{\partial(k_c a)}\left[(k_c a) j_l(k_c a)\right]}{j_l(k_c a)} - \frac{k_c}{k_s}\frac{\frac{\partial}{\partial(k_s a)}\left[(k_s a) h_l(k_s a)\right]}{h_l(k_s a)} = 0 \quad \text{for } \vec{r}\cdot\vec{H}(\vec{r}) = 0 \tag{2.21}$$

where $h_l = j_l + i y_l$ is a spherical Hankel function of the first kind, a is the sphere radius, $k_c = n_c k_0$ is the cavity wavenumber, and $k_s = n_s k_0$ is the surrounding medium's wavenumber. Examples of the WGM intensity distributions for various mode numbers are given in Figure 2.2. The resonant eigenfrequencies of these eigenmodes can also be approximated as per asymptotic expansion of the characteristic equations. This involves approximation of spherical Bessel and Hankel functions as Airy functions, wherein we expand ka as a Taylor series [36, 37]:

$$\begin{aligned} nk_0 a \approx \left(l+\frac{1}{2}\right) + \frac{\alpha_s}{2^{1/3}}\left(l+\frac{1}{2}\right)^{1/3} - \frac{P}{(n^2-1)^{1/2}} + \frac{3}{10}\frac{\alpha_s^2}{2^{2/3}}\left(l+\frac{1}{2}\right)^{-1/3} \\ - \frac{\alpha_s}{2^{1/3}}\frac{P\left(n^2-2P^2/3\right)}{(n^2-1)^{3/2}}\left(l+\frac{1}{2}\right)^{-2/3} + \dots \end{aligned} \tag{2.22}$$

where α_s are roots of the the Airy function $\mathrm{Ai}(-z)$, and $P = n$ for $\psi(\vec{r}) = \vec{r}\cdot\vec{E}(\vec{r})$ or $P = 1/n$ for $\psi(\vec{r}) = \vec{r}\cdot\vec{H}(\vec{r})$. WGM resonance metrics are rapidly calculated using equation (2.22) by retaining a subset of its terms. The number of terms kept and hence accuracy of the calculation comes from factors such as the refractive index profile near the cavity interface and what higher-order effects are at play.

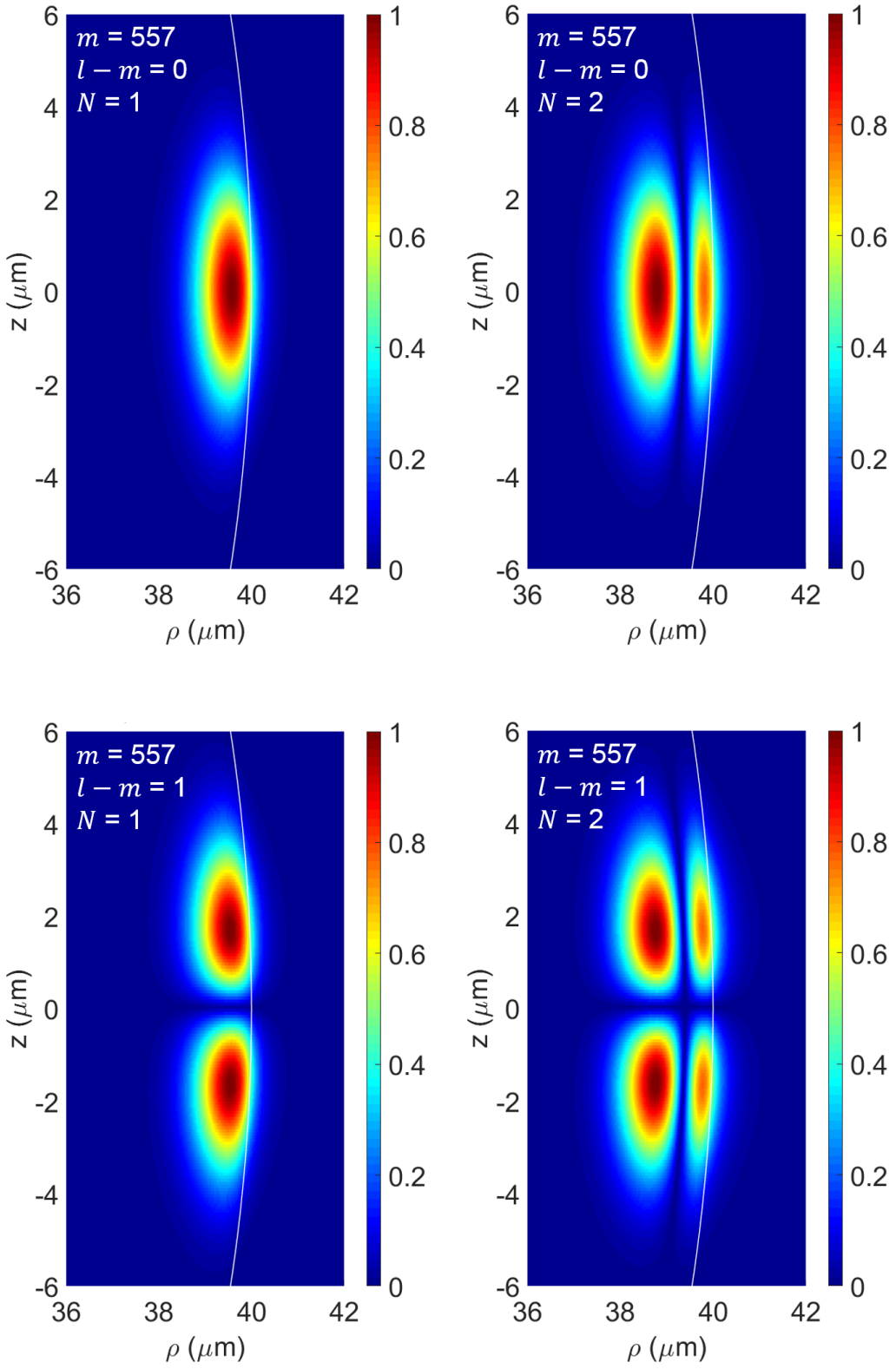

Figure 2.2: Cross-sectional WGM intensity profiles inside a 40-μm radius glass microsphere near $\lambda = 642$ nm. These quasi-TE modes, computed by a finite-difference mode solver (cf. Appendix A), have an aqueous external medium and a major electric field component in the z-direction.

A physical picture of the free spectral range (FSR) emerges from conceptualising the optical path length at the periphery of the cavity. Each round trip, constructive interference of a given mode is satisfied by packing m resonant wavelengths $\lambda_{Res} = 2\pi c/\omega_{Res}$ along the propagation path. By retaining the first term of (2.22), we can express the angular frequency separation between families of resonances as

$$\Delta\omega_{FSR} = \left|\omega_{Res,m} - \omega_{Res,m+1}\right| \approx \frac{c}{2\pi na} \tag{2.23}$$

Resonator performance is expressed by dividing equation (2.23) by the spectral bandwidth. This dimensionless number, coined as finesse, conveys similar information as the quality factor and has a value that is always smaller than the quality factor.

At the cavity boundary, total internal reflection occurs at an incidence angle above $\phi_c = \sin^{-1}(n_s/n_c)$ to generate an exponentially decaying evanescent field. The decay length of this field is also on the order of 100's of nm. All factors considered, by estimation of the effective refractive index n seen by a WGM, a perturbation of the surrounding medium that brings about $n + \Delta n$ thus translates to a proportional shift in the resonant wavelength $\lambda_{Res} + \Delta\lambda_{Res}$. It is therefore possible, by fluctuations in the path length of a WGM resonance, to fashion the optical microcavity as a sensor by inferring change in the surrounding medium's refractive index. A few nano-Kelvin of change in temperature, for instance, can be detected through nonlinear predisposition to thermal effects [38, 39]. Molecules or particles adsorbed to the microcavity surface can similarly introduce a detectable Δn.

2.1.2 Mode Volume

The spatial extent of the WGM is parameterised by the modal volume V_m. It is, by estimation, the volume within which the mode's peak energy density $u(\vec{r})|_{max}$ would be homogeneously distributed:

$$V_m = \frac{\int_V u(\vec{r})d\vec{r}}{u(\vec{r})|_{max}} = \frac{\int_V \varepsilon(\vec{r})\left|E(\vec{r})\right|^2 d\vec{r}}{\varepsilon(\vec{r})\left|E(\vec{r})\right|^2\Big|_{max}} \tag{2.24}$$

There are other modal volume expressions with greater accuracy and that are applicable to open systems [40]. Despite this, the phenomenological V_m of equation (2.24) is reasonable enough to model a system that is not strongly influenced by optical nonlinearities. WGM sensing and its dependence on V_m, including hybridisation with localised surface plasmon modes, will be discussed in Chapter 3.

2.1.3 Loss Mechanisms and Coupling

Temporal confinement of a WGM is quantified by its quality (Q) factor. A resonator's Q-factor conveys the ratio between the energy stored and the energy dissipated per cycle (i.e. round trip). For a lifetime τ, a resonant lineshape with spectral position ω_{Res} and linewidth $\delta\omega$ provides a means to calculate

$$Q = \frac{\omega_{Res}}{\delta\omega} = \tau\omega_{Res} \tag{2.25}$$

Non-ideal systems that store photons will do so for a finite amount of time. Dissipation, as in the majority of real-world processes, comes from multiple sources: absorption, radiation, scattering, and external coupling losses. All but the last of these sources are intrinsic, originating from cavity material/adsorbent absorption, photon tunneling into radiative modes, and surface scatterers/inhomogeneities, respectively. The total quality factor

$$Q = \frac{Q_0 Q_{ext}}{Q_0 + Q_{ext}} \tag{2.26}$$

has intrinsic (Q_0) and extrinsic (Q_{ext}) contributions. We further decompose Q_0 by first accounting for absorption (Q_{abs}) – a significant component to loss, which has been shown to be [41]:

$$Q_{abs} = \frac{2\pi n}{\alpha_{abs}\lambda_{Res}} \tag{2.27}$$

where α_{abs} is the linear absorption coefficient. In parallel to the formulation of (2.22), the radiation loss (Q_{rad}) related to the cavity size and profile can also be approximated [36]. Generally, smaller radii of curvature that result in more restrictive, cross-sectional cavity profiles will lower Q_{rad}. The benchmark for absorption-limited Q-factors is $0.8 \pm 0.1 \times 10^{10}$ for large 500-1000 μm-diameter microspheres at a wavelength of 633 nm [41]. Scattering (Q_{scat}) then completes the intrinsic Q_0 via

$$Q_0^{-1} = Q_{abs}^{-1} + Q_{rad}^{-1} + Q_{scat}^{-1} \tag{2.28}$$

to summarise the dominant channels for modal photon loss. At the critical coupling point, where $Q_0 = Q_{ext}$, power is transferred completely to the WGM and the transmission past the cavity vanishes due to total destructive interference.

Free-space coupling to an optical microcavity suffers from poor efficiency due to the contrasting phase velocities in silica and in air. This generally holds true for other cavity materials and external media as well, such as silicon nitride in water. Evanescent coupling

to WGMs is the common solution to this problem by way of a employing a tapered optical fiber [42] or prism coupler [43]. In each case, wavevectors are phase matched and the evanescent field is proximate enough to the cavity to couple efficiently into a WGM. This power transferred can be formulated via coupled mode theory [44, 45]. From an experimental point of view, the resonant light recirculation in the cavity can be monitored by the light transmission T (illustrated in Figure 2.3) past the WGM microcavity [46]:

$$T = \left(\frac{\tau_{ext} - \tau_0 - i\Delta\omega}{\tau_{ext} + \tau_0 + i\Delta\omega} \right)^2 \tag{2.29}$$

that is defined given a detuning $\Delta\omega = \omega - \omega_{Res}$, intrinsic/cavity decay rate $\tau_0 = Q_0/\omega$, and extrinsic/coupling decay rate $\tau_{ext} = Q_{ext}/\omega$. Undercoupling occurs for $\tau_0^{-1} > \tau_{ext}^{-1}$, overcoupling for $\tau_0^{-1} < \tau_{ext}^{-1}$, and critical coupling for $\tau_0^{-1} = \tau_{ext}^{-1}$. Once the coupling decay rate is equal to the cavity decay rate, we find the output field acquires a π phase-shift which is carried into the overcoupled regime.

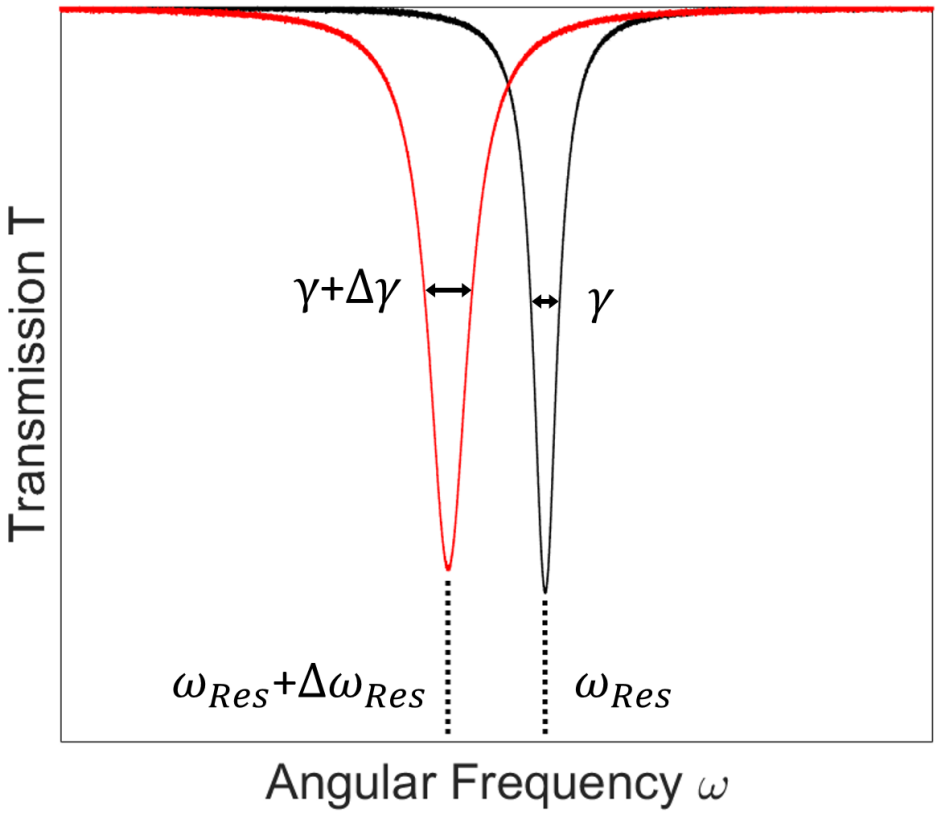

Figure 2.3: The shift and broadening of a Lorentzian WGM resonance lineshape from a dielectric perturber. The resonant angular frequency ω_{Res} and linewidth $\gamma = \delta\omega$ together determine the resonator's total quality factor $Q = \omega_{Res}/\gamma$.

2.1.4 Nonlinearities

The build-up of optical energy in a WGM resonator greatly reduces nonlinearity thresholds down to microwatts of power. With a low modal volume V_m and ultrahigh Q, this becomes accessible as common thresholds ($\propto V_m/Q^2$) are related to the Purcell factor ($\propto Q/V_m$). R. K. Chang and A. J. Campillo identified such nonlinearities early on by low-efficiency excitation of high-Q microdroplets with a free-space beam [47, 48, 49, 50, 51], observing stimulated Brillouin scattering [48], induced Raman oscillations [48, 50, 51], and cascaded Raman scattering [48]. A material's nonlinear optical response is derived from higher-order polarisation terms of the Taylor series

$$\vec{P}(t) = \varepsilon_0 \left[\chi^{(1)} \vec{E}(t) + \chi^{(2)} \vec{E}^2(t) + \chi^{(3)} \vec{E^3}(t) + \dots \right] \tag{2.30}$$

where $\chi^{(1)} = \chi_e$ is the linear susceptibility we usually treat as a scalar. The susceptibilities $\chi^{(n)}$, however, are in fact tensors with rank $n+1$. Terms with $n > 1$ cross-link various frequencies of the field $\vec{E}(t)$, allowing frequency conversions, oscillations, and modulations in the form of processes such as second-harmonic generation ($\chi^{(2)}$), two-photon absorption ($\chi^{(3)}$), coherent Raman scattering ($\chi^{(3)}$), and the Kerr electro-optic effect ($\chi^{(3)}$). Conversions are classified into two categories: parametric and non-parametric, based on whether or not the light fields exchange energy or momentum. Stimulated optical scattering processes, for example, are non-parametric since they repopulate the quantum mechanical states of a system.

Unsuprisingly, the enhanced circulating power of a WGM triggers absorption-based thermal nonlinearities. Heat is generated from the resonant mode and thermal conductivity primarily transfers this energy throughout the cavity and its environment. According to thermorefractivity (dn/dT) and the thermal expansion (dL/dT) of the optical path length L, a temperature drift ΔT will shift the resonant wavelength by

$$\Delta\lambda_{Res} = \Delta T \left(\frac{1}{n}\frac{dn}{dT} + \frac{1}{L}\frac{dL}{dT} \right) \lambda_{Res} \tag{2.31}$$

Fused silica, as a reference, possesses $(1/n)(dn/dT) + (1/L)(dL/dT) = 8.83 \times 10^{-6}\ \mathrm{K}^{-1}$ at 1540 nm [52]. In addition to a WGM microcavity's sensitivity to temperature change, scanning past a thermally broadened resonance can induce hysteretic and bistable behaviour. It is possible to compensate for thermal noise in a wavelength upscan as a decrease in pump power will be met with an increase in absorbed power [53]. These optothermal dynamics in the blue-detuned region may create a negative feedback, as per a Pound-Drever-Hall technique, to lock the laser to the cavity resonance.

2.1.5 Mode Splitting

An ideal WGM resonator can support a pair of degenerate eigenmodes with positive and negative m. Each sign of m is associated with a possible field propagation direction, i.e. the clockwise (CW) or counterclockwise (CCW) directions with respect to the plane of propagation. Adsorbed scatterers within the evanescent field of the WGM can backscatter a portion of the energy back into the cavity. If the coupling rate is above the cavity decay rate, a scatterer of polarisability α can produce a symmetric and asymmetric standing wave doublet split by

$$g = -\frac{\alpha f^2(\vec{r})\omega}{2V_m} \tag{2.32}$$

where ω is the originally degenerate eigenfrequency and $f(\vec{r})$ is the overlap of the nanoparticle with the WGM [54]. Such a self-reference enables particle sizing and common mode noise rejection, e.g. supression of probe laser jitter, as well as multiplexing granted by the field nodes/antinodes of the symmetric-asymmetric standing wave eigenmode basis. We note that the dipole approximation used to arrive at (2.32), however, underestimates the interaction strength – greater accuracy is attained for small scatterers by way of a renormalised Born approximation [55].

2.1.6 Applications

WGM architectures are central building blocks for many integrated platforms. The frequency comb [56], that serves as an optical ruler for metrology, has been achieved by microcavities using the Kerr effect [57]. In this scheme, parametric oscillation allows an optical pump frequency to generate a lower and higher frequency that then all self-interact by nondegenerate four-wave mixing to construct a comb spectrum. Lasing mediated by a WGM has been investigated, through means such as upconversion in a Er^{3+}-doped silica microtoroid [58], stimulated Brillouin scattering in a crystalline CaF_2 resonator [59], or Raman scattering in a standard glass microsphere [28]. An advantage of lasing is that the WGM resonance linewidth narrows, which can improve device performance for applications that involve lossy elements. For example, tuning to exceptional points has been done by balancing absorption [60] or scattering [61] with optical gain to resolve split modes. The study of mechanical modes in a WGM resonator excited by radiation pressure is yet another active field of research. WGM cavity optomechanics, first reported in 2005 [62, 63] and its use in cooling in 2006 [64], has been examined in capillaries [65], microdroplets [66], and highly damped environments [67].

2.2 Nanoplasmonics

Applications of plasmonics arose as early as the 4th century with the glass staining of the Lycurgus cup in ancient Rome [68]. The dichromatism of the cup dependent on illumination comes from the fact that electrons travelling in the conduction band of metallic matter are prone to excitation by light. From a semi-classical perspective, the dispersion relations that describe this response set the stage for quantised oscillations and electromagnetic surface waves. Noble metals, such as gold and silver, also have interband transitions at photon energies above 1 eV (i.e. $\lambda \leq 1\ \mu$m) which bring about strong absorption. Gold and silver are common plasmonic materials in the literature due to their stability and small ohmic losses in the visible. Silver supports surface plasmons throughout the visible spectrum, while copper and gold suffer from an onset of intraband and interband transitions that restricts their operating range. Further, palladium [69] and platinum [70] are attractive alternatives if catalytic activity is needed. In this section we will outline the role of plasmonics at the nanoscale for the purposes of light field enhancement and confinement.

2.2.1 General Theory

Surface plasmon polaritons (SPPs) can be described by first considering a planar interface that exists between a conductive and non-conductive material. The dielectric will have real ε_d and the metal will incur ohmic losses with an attenuation coefficient κ_m (hence complex $\varepsilon_m = \varepsilon_m' + i\varepsilon_m''$ with $|\varepsilon_m''| \ll |\varepsilon_m'|$) below the metal's bulk plasmon frequency ω_p. The real part of the metal's permittivity ε_m' is necessarily negative, so that an SPP can propagate along the interface with parallel wavevector component:

$$k_{||} = k_{||}' + ik_{||}'' \approx \frac{\omega}{c}\sqrt{\frac{\varepsilon_m'\varepsilon_d}{\varepsilon_m' + \varepsilon_d}}\left[1 + i\frac{\varepsilon_m''\varepsilon_d}{2\varepsilon_m'(\varepsilon_m' + \varepsilon_d)}\right] \tag{2.33}$$

The SPP dispersion relation lies in the real part of this wavevector, such that the wavelength

$$\lambda_{SPP} = \frac{2\pi}{k_{||}'} \approx \lambda\sqrt{\frac{\varepsilon_m' + \varepsilon_d}{\varepsilon_m'\varepsilon_d}} \tag{2.34}$$

Resulting surface-bound SPPs will propagate to a finite length determined by $1/k_{||}''$, roughly equal to 10 μm for gold and 60 μm for silver at an optical wavelength $\lambda = 633$ nm [71]. Perpendicular to the interface, however, we find the field's $1/e$ decay length to be much

smaller inside and outside of the metal. To first order in $|\varepsilon_m''|/|\varepsilon_m'|$, the half-spaces have

$$k_{m,\perp} \approx \frac{\omega}{c}\sqrt{\frac{\varepsilon_m'^2}{\varepsilon_m'+\varepsilon_d}}\left(1+i\frac{\varepsilon_m''}{2\varepsilon_m'}\right) \tag{2.35}$$

$$k_{d,\perp} \approx \frac{\omega}{c}\sqrt{\frac{\varepsilon_d^2}{\varepsilon_m'+\varepsilon_d}}\left[1-i\frac{\varepsilon_m''}{2\left(\varepsilon_m'+\varepsilon_d\right)}\right] \tag{2.36}$$

with $1/k_{Au,\perp} = 28$ nm and $1/k_{Air,\perp} = 328$ nm for gold, while $1/k_{Ag,\perp} = 23$ nm and $1/k_{Air,\perp} = 421$ nm for silver [71]. The free-space light line $\omega = ck_{||}$ does not intersect the SPP dispersion curve. If the neighbouring dielectric's refractive index n is raised, the light line $\omega = ck_{||}/n$ can be sufficiently titled as to excite SPPs. Additionally, the smaller dimensions of a plasmonic nanoparticle/nanostructure may fall below the electron mean free path and increase ε_m'' due to increased interface scattering.

Nanoplasmonics with noble metals is often exploited at visible frequencies to confine light beyond the diffraction limit. In this way, plasmonic nanoparticles inherit tuneable resonances based on their shape and size. Under the assumption that a metallic particle has dimensions much smaller than the wavelength of light, its dominant localised surface plasmon (LSP) resonance can be modelled using the quasi-static approximation. Treating the local electric field $\vec{E} = -\nabla\Phi$ with a potential Φ that satisfies $\nabla^2\Phi = 0$, the scattered field becomes equivalent to that of an eletrostatic field emanating from the nanoparticle. A plasmonic nanosphere of radius r_m in this context therefore has a polarisability:

$$\alpha(\omega) = 4\pi\varepsilon_0 r_m^3 \frac{\varepsilon_m(\omega)-\varepsilon_d}{\varepsilon_m(\omega)+2\varepsilon_d} \tag{2.37}$$

The resonance or Frölich condition is met when the denominator of the polarisability becomes zero, i.e. $\varepsilon_d = -2\varepsilon_m$, which excludes any size/shape dependence. To fully capture LSP spectral features, one can apply Mie theory in order to incorporate field retardation inside the metal and include multipolar excitation [72]. Less rigorously, if we extend the nanostructure to an ellipsoid with semi-axes $a_x < a_y < a_z$, the polarisabilities along all three axes are

$$\alpha_i(\omega) = \frac{4}{3}\pi\varepsilon_0 a_x a_y a_z \frac{\varepsilon_m(\omega)-\varepsilon_d}{\varepsilon_d + L_i\left[\varepsilon_m(\omega)-\varepsilon_d\right]} \tag{2.38}$$

where $i = x$, y, or z, and

$$L_i = \frac{a_x a_y a_z}{2} \int_0^\infty \frac{dq}{\left(a_i^2 + q\right) f(q)} \tag{2.39}$$

$$f(q) = \sqrt{\left(a_x^2 + q\right)\left(a_y^2 + q\right)\left(a_z^2 + q\right)} \tag{2.40}$$

$$\sum L_i = 1 \tag{2.41}$$

It is then easy to see that, for a plasmonic nanorod or prolate spheroid, its dimensions $a_x = a_y < a_z$ will lead to

$$L_z = \frac{1 - e^2}{e^2}\left(\frac{1}{2e} \ln \frac{1+e}{1-e} - 1\right) \tag{2.42}$$

with eccentricity $e = \sqrt{1 - (a_{x,y}/a_z)^2}$ and aspect ratio $a_z/a_{x,y}$.

The longitudinal and transverse LSP resonance conditions are $\varepsilon_d = \varepsilon_m L_z/(L_z - 1)$ and $\varepsilon_d = \varepsilon_m L_{x,y}/(L_{x,y} - 1)$, respectively. Such resonances are measurable by extinction spectra, as in Figure 2.4, that are separated into absorption and scattering components with cross sections [71]:

$$\sigma_{abs} = \frac{k}{\varepsilon_0} \mathrm{Im}\left[\alpha(\omega)\right] \tag{2.43}$$

$$\sigma_{scat} = \frac{k^4}{6\pi\varepsilon_0^2} \left|\alpha(\omega)\right|^2 \tag{2.44}$$

These plasmon resonances can be tuned as far as into the near-infrared by exaggerating the aspect ratio. Therefore, it is straightforward to operate an optical microcavity coupled to plasmonic nanoparticles near LSP resonance within the visible spectrum.

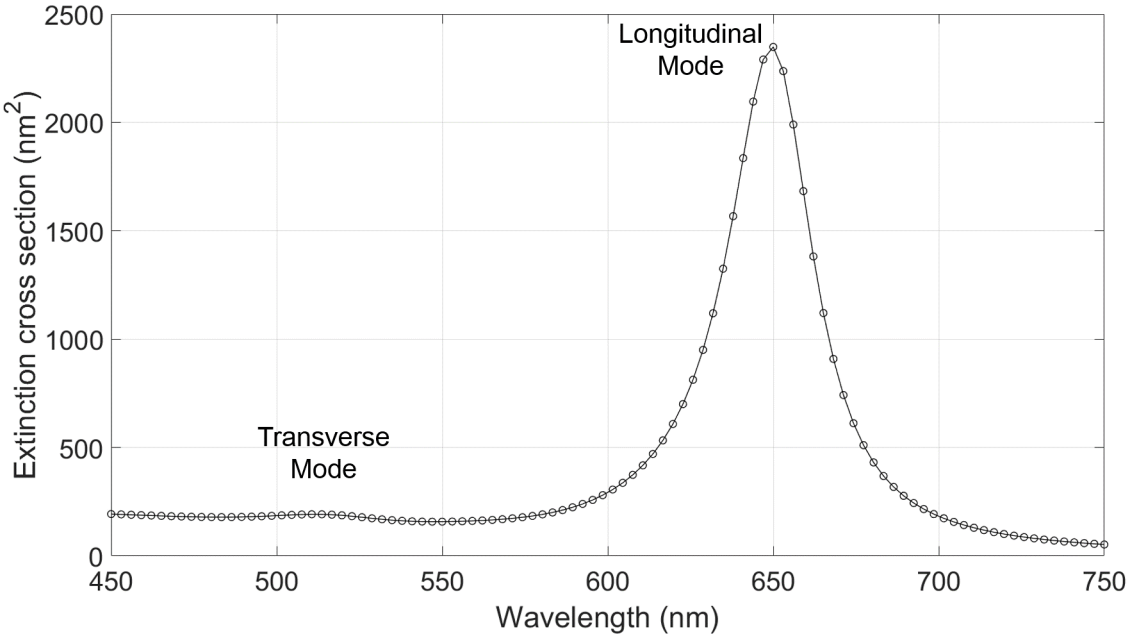

Figure 2.4: Computed extinction cross sections $\sigma = \sigma_{abs} + \sigma_{scat}$ of a gold nanorod, with a diameter of 10 nm and a length of 24 nm, in water.

2.2.2 Plasmonic Nanoparticles as Nanoantennae

The curved surface of a plasmonic nanoparticle exerts a restoring force on the electron oscillations driven by light, amplifying the light intensity in hotspots near the nanoparticle surface. The extinction cross sections of such plasmonic nanoparticles can be on the order of 1,000's of nm^2. Deposition of gold nanoparticles onto a WGM microcavity hence, from absorption and scattering losses, entails significant Q-factor degradation by an order of magnitude for a few adsorbed nanoparticles alone (see Figure 2.5). The desirable trade-off instead lies in the extent of field enhancement/minification gained relative to this loss. It is well-established that, as shown in the simulated intensity distribution of Figure 2.6, gold nanorods have LSP-enhanced near fields that decay within less than 10 nm and enhance the local field intensity by at least a factor of 100 [73]. This makes plasmonic nanoparticles suitable candidates for nanoantennae on an optical WGM microcavity, as they improve the Q/V_m ratio and so increase the Purcell factor. In this thesis we are particularly interested in how plasmonic nanoantennae coupled to an optical WGM can be used to sense subsequent interactions between light and biological matter. This is of fundamental importance not only because we can look at surface reactions taking place on the plasmonic nanoantenna, yet also because we wish to arrive at the limits of nanochemistry and will attempt to characterise biomolecules individually.

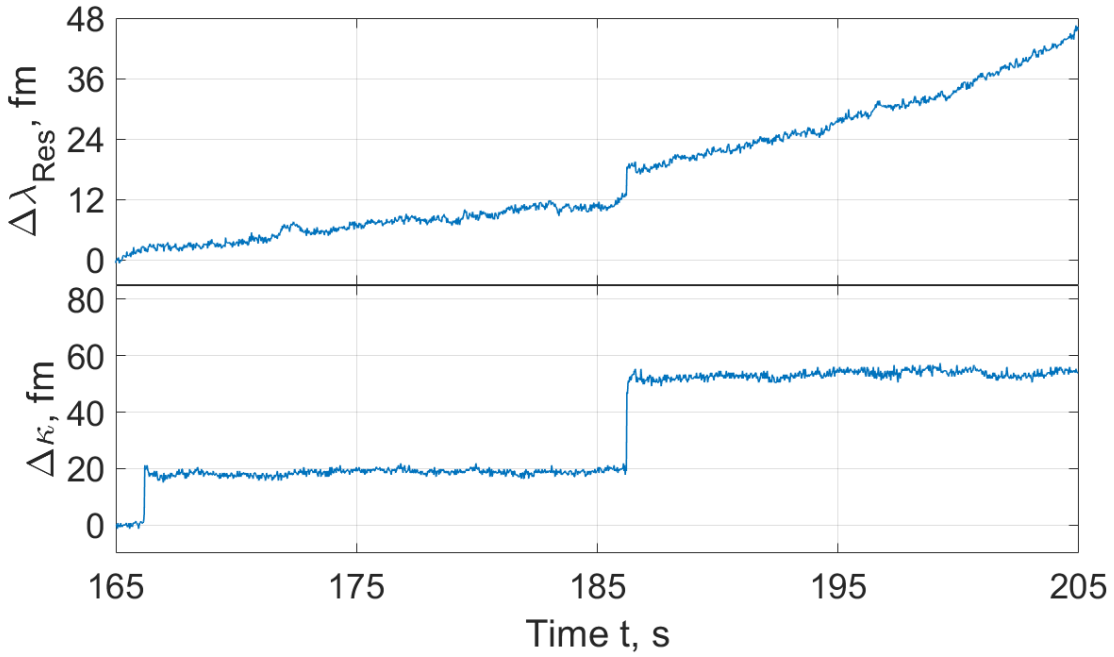

Figure 2.5: Added losses observed in a tracked WGM resonance (cf. Figure 2.3) when gold nanorods adsorb to the glass microspherical resonator in solution. Positive steps in $\Delta\kappa$ are attributed to the adhesion of these highly absorbing/scattering nanoparticles. Laser light input is swept accross the resonance's transmission dip, with initial position λ_{Res} = 642.006358 nm and full width at half maximum κ = 229 fm, while the nanorods have an average radius = 10 nm and length = 24 nm with plasmon resonance wavelength around 650 nm.

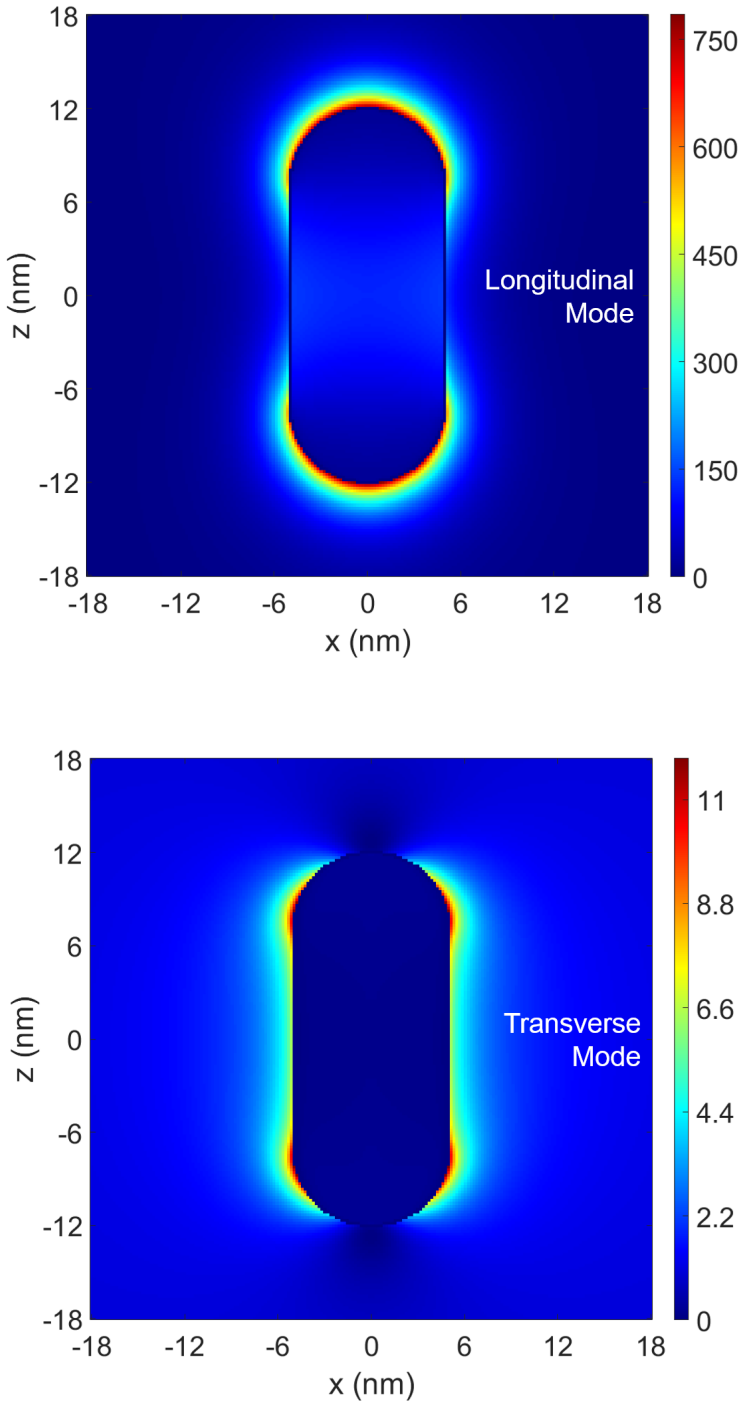

Figure 2.6: Near-field intensity enhancement from localised surface plasmon resonance of a gold nanorod, with a diameter of 10 nm and a length of 24 nm, in water. The distribution is plotted via boundary element method and the excitation wavelength is at $\lambda = 642$ nm.

Chapter 3

Single-Molecule Sensors

3.1 Current Methodologies

In the same way microorganisms became visible with the invention of the optical microscope in the 16th century, humanity ventured into the realm of nanoscale biology in the turn of the 21st century. We can consider the advent of the optical tweezer in 1986 a step forward [74], wherein a direct means to manipulate single biomolecules was formalised. Today, kinesin tethered to a dielectric bead can be trapped with a beam gradient-force to study the protein's motion on microtubules [75]. Such technology allows for the isolation of intricate biomechanics that underlie the function of a living cell. It is, on the other hand, arguably more important even to understand these dynamics by proper techniques to visualise them. Often we can lift the apparently stochastic behaviour of a ensemble by tracking chemical species one at a time. This is our aim in this chapter: the sensing of single molecules.

A number of viable avenues for single-molecule sensing were developed over the last four decades. Using free-space light, we can do this without labels through surface-enhanced Raman scattering (SERS) [76, 77] or photothermal microscopy [78] of gold nanoparticles. Electrically, we can measure the conductance of a molecular junction between gold tips [79], a molecule binding onto a graphene membrane [80], or the infinitesimal coating of a carbon nanotube [81]. Atomic force can be exerted by a molecule onto a scanned tip [82], the mechanical resonance frequency of a cantilever can shift with protein loading [83], or the mass of a molecule can effectuate enough surface stress to be detected [84]. Only recently, the heat transport through an alkanedithiol junction was assessed [85]. These advancements collectively offer a toolbox to characterise biomolecules in terms of their various physical properties. Nevertheless, no one methodology can exclusively and elegantly reconstruct a molecule in space and in time — a challenge that the diffraction limit is partly to blame for. A molecular scanning device with this capability so far remains an ideality.

3.2 Towards Optoplasmonic Sensors

An optical WGM resonance shifts in the presence of biomolecules that overlap with its evanescent field. Work is done by the light field by polarising the dielectric analyte, distorting the electronic distribution in the material and inducing a dipole moment. The near field $\vec{E}$ is then weakly perturbed, and so we can apply first-order perturbation theory to calculate the shift $\Delta\lambda_{Res}$ caused by the analyte's excess polarisability α_{ex} positioned at $\vec{r}_p$ [86]:

$$\frac{\Delta\lambda_{Res}}{\lambda_{Res}} \approx \frac{\mathrm{Re}\{\alpha_{ex}\}}{2} \frac{f\varepsilon_s \left|\vec{E}(\vec{r}_p)\right|^2}{\int_v \varepsilon(\vec{r}) \left|\vec{E}(\vec{r})\right|^2 d\vec{r}} \tag{3.1}$$

in a host medium of permittivity ε_s. The above mechanism is dubbed the reactive sensing principle, wherein the form factor f corrects for analytes of larger size relative to the WGM's evanescent field [87, 88]. If we model the analyte as a dielectric nanoparticle with polarisability of the same form as expression (2.37), it becomes clear that one can correlate resonance perturbations in time with biomolecule adsorption onto the bare cavity sensor. In parallel, the WGM linewidth is broadened by the analyte as per [89]:

$$\frac{\Delta\gamma_{abs}}{\omega_{Res}} \approx \mathrm{Im}\{\alpha_{ex}\}\,\varepsilon_s \frac{\left|\vec{E}(\vec{r}_p)\right|^2}{\int_v \varepsilon(\vec{r}) \left|\vec{E}(\vec{r})\right|^2 d\vec{r}} \tag{3.2}$$

alongside scattering changes from what is effectively a dipole scatterer [22]:

$$\Delta\gamma_{scat} \approx \frac{n_s^5 \omega_{Res}^4 |\alpha_{ex}|^2}{6\pi c^3} \frac{\left|\vec{E}(\vec{r}_p)\right|^2}{\int_v \varepsilon(\vec{r}) \left|\vec{E}(\vec{r})\right|^2 d\vec{r}} \tag{3.3}$$

the latter contributor of which was foreshadowed in Chapter 2 and can lead to a mode split. We note that the angular frequency linewidth $\gamma = \delta\omega \approx \frac{2\pi c}{\lambda_{Res}^2}\delta\lambda$ for a narrow wavelength linewidth $\kappa = \delta\lambda$. From formula (2.32), the coupling strength $|g|$ corresponding to the energy redistribution between clockwise- and counterclockwise-propagating WGMs also defines two regimes for the linewidth change observed experimentally: unresolved ($2\Delta\omega_{Res} \lesssim \omega_{Res}/Q_0$) or resolved ($2\Delta\omega_{Res} \gg \omega_{Res}/Q_0$) mode splitting. This extra loss term $\Delta\gamma_{split}$ in the former regime may give rise to an apparent linewidth broadening/narrowing that convolves the identity of the perturbation, e.g. absorption or scattering, with the overall lineshape distortion.

Unfortunately, in view of noise sources, there are limits to the size of single entities that can be detected by plain WGM based sensing. The theoretical minimum number of detectable bioparticles through mode shift and broadening have been shown to be [90]:

$$N_{\lambda_{Res}} = \frac{\left(n_c^2 - n_s^2\right)}{\mathrm{Re}\left\{\alpha_{ex}\right\}} \frac{a^3}{\left|Y_{ll}\left(\pi/2\right)\right|^2} \frac{F_0}{Q_0} \frac{\left(1 + Q_{ext}/Q_0\right)^3}{4Q_{ext}^2/Q_0^2} \tag{3.4}$$

and

$$N_{\gamma_{scat}} = \frac{6\pi c^3 \left(n_c^2 - n_s^2\right)}{\left|\alpha_{ex}\right|^2 n_s^5 \omega_{Res}^3} \frac{a^3}{\left|Y_{ll}\left(\pi/2\right)\right|^2} \frac{F_0}{Q_0} \frac{\left(1 + Q_{ext}/Q_0\right)^3}{4Q_{ext}^2/Q_0^2} \tag{3.5}$$

far from molecular resonances (i.e. scattering dominates over absorption) and with a microspherical cavity of radius a. The spherical harmonic $Y_{ll}\left(\pi/2\right)$ is evaluated at the equator and the measurement acuity constant F_0 encapsulates noise, e.g. from the detector or thermorefractivity. Besides squeezed states of light, we clarify that optical sensing instrumentation is ultimately limited by shot noise [91]:

$$\frac{\Delta\omega_{Res}}{\omega_{Res}} \geq \frac{1}{Q_0} \sqrt{\frac{\hbar\omega_{Res}}{P_0 T \eta \tau}} \tag{3.6}$$

given the reduced Planck constant $\hbar = 1.05 \times 10^{-34}$ J·s, the optical input power P_0, the on-resonance T, the photodetector quantum efficiency η, and the averaging time τ. More practically, detector noise is affected by sources such as probe laser instability before ever reaching quantum limits. A lower bound for detectable polystyrene nanoparticle size is shown in Figure 3.1 in terms of mode shifting, broadening, and splitting channels. Above a cavity Q-factor of 0.5×10^8, the limit of detection for solid polystyrene nanoparticles settles just below a radius of 10 nm. Ergo, the finer contents in a cell nucleus, such as histone deacetylase or a strand of deoxyribonucleic acid (DNA), perturb the WGM too weakly and so escape detection. It was in the early 2010's that this pitfall was overcome by adopting a hybrid photonic-plasmonic platform [19, 20, 21, 22, 92]. Merging these modalities was motivated by raising Q/V_m, dually localising and intensifying the WGM near field through coupling to the LSP resonances of plasmonic nanoantennae. Chemical species as simple as zinc and mercury ions have measurably interacted with such optoplasmonic sensors [93].

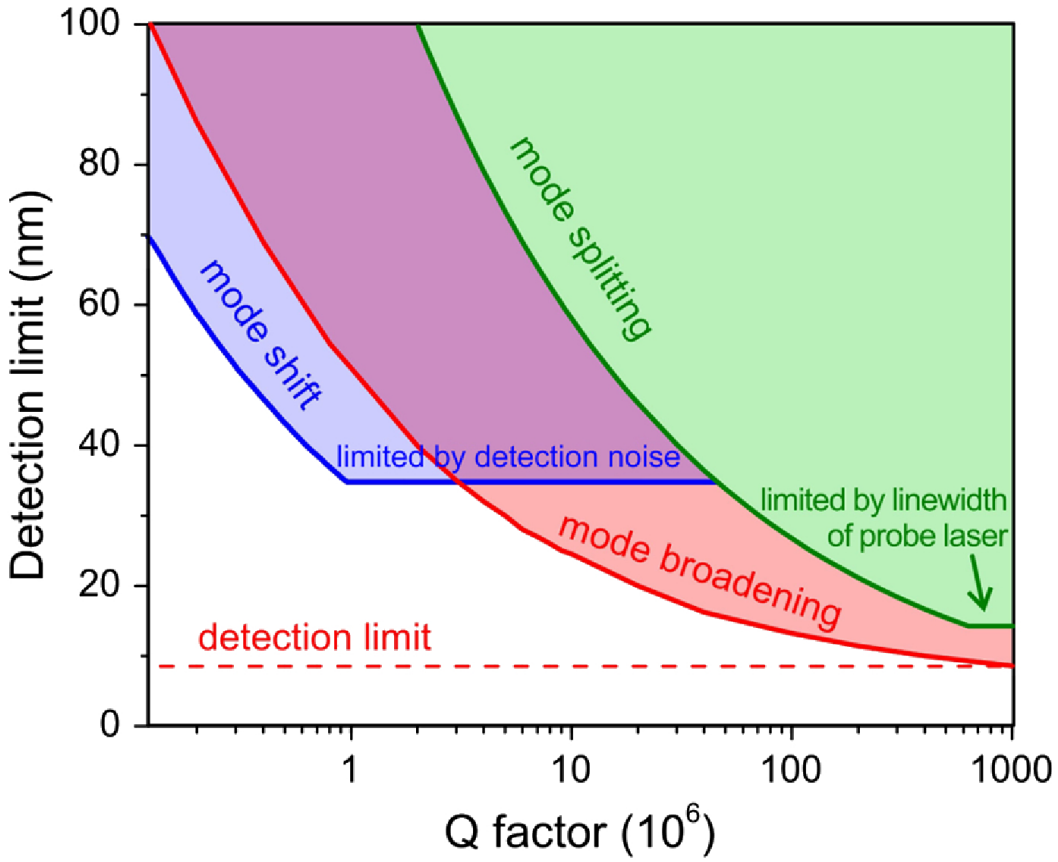

Figure 3.1: Theoretical limits of detection for sensing polystyrene nanospheres in air using WGM resonance shifting (blue), mode broadening (red), and mode splitting (green) parameters. This plot was published in [94] using data from [95].

3.2.1 LSP-WGM Hybridisation

The curious case of modal coupling between WGMs and LSPs has been touched upon in the literature. In the context of photothermal absorption spectroscopy, the back-action of WGMs (without waveguided pumping) on an LSP of an excited plasmonic nanoparticle absorber has been described [96]. For the optoplasmonic sensor of this thesis, however, a pump continually supplies energy to WGMs which in turn excite the LSP. With a generalised momentum $p_0(t)$ of the LSP and generalised momenta $p_n(t)$ of the WGMs, the conceivable equations of motion for n WGMs of an optoplasmonic sensor are

$$\ddot{p}_0 + \gamma_0 \dot{p}_0 + \omega_0^2 p_0 + \sum_n g_n^2 \omega_0^2 p_n = 0 \tag{3.7}$$

$$\ddot{p}_n + \omega_n^2 p_n + g_n^2 \omega_n^2 p_0 = \omega_n^2 \sqrt{V_n} E_{ext} e^{-i\omega t} \tag{3.8}$$

denoting g_n as the coupling terms, ω_0 as the LSP resonant angular frequency, γ_0 as the plasmon decay rate, ω_n as the WGM resonant angular frequencies, V_n as the modal volume of the n^{th} WGM, and E_{ext} as the pump laser field of angular frequency ω. Newton's differential notation $\dot{x} = \frac{dx}{dt}$ and $\ddot{x} = \frac{d^2x}{dt^2}$ is used here for brevity. The broad LSP, with mode volume V_0, and the near-discrete WGMs can constructively and destructively interfere as to result in Fano asymmetries. In the case of free-space excitation of a plasmonic nanoantenna, the absorption spectrum of the nanoantenna undergoes Fano interference [96]:

$$\sigma_{abs}(\omega) = \frac{4\pi V_0 \omega}{c} \mathrm{Im}\left\{ \frac{\omega_0^2\left(\omega_1^2 - \omega^2\right)}{\left(\omega_1^2 - \omega^2\right)\left(\omega_0^2 - \omega^2 - i\omega\gamma_0\right) - g_1^4\omega_1^2\omega_0^2} \right\} \tag{3.9}$$

derived by relation to the time-averaged oscillator strength. LSP-WGM hybridisation is simplified here to a single WGM where the rapid WGM phase variation dictates the asymmetry by an approximate factor of $(2/\gamma_0)(\omega_1 - \omega_0)$. Based on equations of motion (3.7) and (3.8) of our own system, the absorption cross-section of a plasmonic nanoantenna for a WGM pumped by the waveguide is deduced to be:

$$\sigma_{abs}(\omega) = \frac{4\pi\sqrt{V_1}\sqrt{V_0}\omega}{c} \mathrm{Im}\left\{ \frac{g_1^2\omega_1^2\omega_0^2}{\left(\omega^2 - \omega_1^2\right)\left(\omega_0^2 - \omega^2 - i\omega\gamma_0\right) + g_1^4\omega_1^2\omega_0^2} \right\} \tag{3.10}$$

Unlike in equation (3.9), dependence on V_1 implies that the modal structure of the WGM directly impacts the nanoantenna's absorption cross-section. A question then arises as to whether a single molecule interacting with a plasmonic nanoantenna can significantly perturb this absorption cross-section to broaden or narrow the hybrid LSP-WGM resonance linewidth. If an LSP resonance redshifts due to a locally increased refractive index from protein binding, as previously demonstrated by photothermal assay in [78], it is understood that the extinction spectrum will shift and so the overall loss rate of a WGM resonance coupled to the LSP will change. Such photothermal experiments found that the plasmon shift scaled nonlinearly with molecular weight. Expanding on the argument that there is reduced overlap for larger biomolecular complexes, given any spatial extent of the analyte on the order of a few nm, a complete mechanistic description of the plasmon response is required.

3.2.2 Optomechanical Plasmon-Vibration Coupling

Molecules vibrate according to the anharmonic potentials defined by their composition, distribution of atoms, and the surrounding environment. At high occupancy these vibrational modes couple to one another as to internally redistribute the vibrational states of the excited molecule [97]. A feedback model for LSP and molecular vibrational modes can be formulated

without anharmonicity, however, to good approximation as described by Kippenberg *et al.* [98]. A molecule that is constantly subjected to thermal forces δF_{th} under ambient conditions, in conjunction with a time-dependent force δF_p exerted by an LSP, has its vibrational modes displaced by δx_v and hence its polarisability is altered by $\delta\alpha$ through Raman activity $\partial\alpha/\partial x_v$. The possibility of dynamical backaction amplification and the feedback loop that underlies this are highlighted in Figure 3.2. Red-detuning of the excitation laser from plasmon resonance decreases the damping rate and amplifies molecular motion [63], while blue-detuning increases the damping rate and cools the molecule [64].

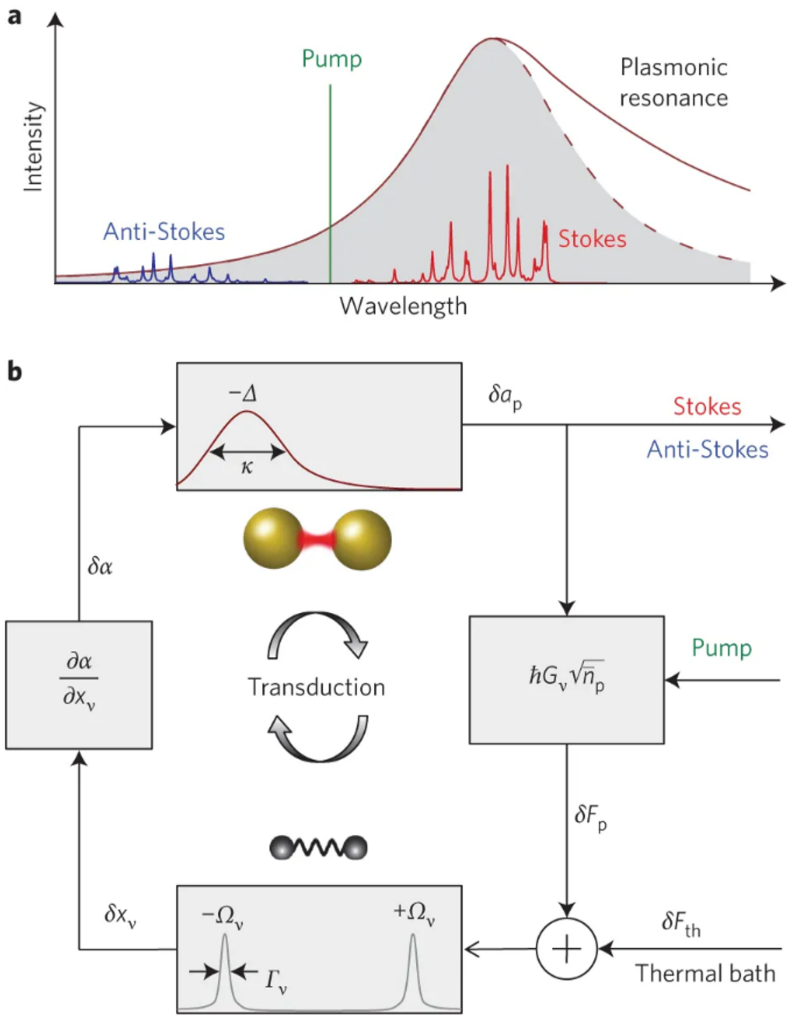

Figure 3.2: Optomechanical coupling between plasmon and molecular phonon modes. (a) Selective enhancement of Stokes lines in a Raman spectrum. (b) Transduction scheme for an LSP and molecular vibrational resonance, with detuning $\Delta = \omega - \omega_0$, LSP linewidth κ, field fluctuation δa_p, coupling rate G_v, time-averaged plasmon occupancy $\bar{n}_p$, and mechanical resonance fequencies $\pm\Omega_v$ with linewidth Γ_v. These schematics appear in [98].

The LSP resonance frequency ω_0 is then tied to a molecular vibration, i.e. with effective mass = m_v and mechanical frequency = Ω_v, such that the vacuum optomechanical coupling rate is [98]:

$$g_{v,0} = \omega_0 \frac{\partial \alpha}{\partial x_v} \frac{1}{V_m \varepsilon_0} \sqrt{\frac{\hbar}{2 m_v \Omega_v}} \tag{3.11}$$

given the field's effective mode volume V_m. For instance, thiophenol with a vibrational mode frequency $\Omega_v = 188$ THz [99] inside a gold dimer's gap plasmon mode of volume $V_m \approx 1.5 \times 10^{-6}\ \mu\text{m}^3$ at $\lambda_p = 900$ nm [100] has a projected optomechanical coupling rate $g_{v,0} = 132$ GHz. Results in Chapter 6 will revisit this coupling hypothesis as it applies to the optoplasmonic detection of single molecules. Energy landscapes for molecular vibrational states contain features that are distinct with respect to single-molecule perturbations predictable solely from the intense local fields of a plasmonic nanoparticle.

3.3 Experimental Protocol for Single-Molecule Detection

To create the glass WGM micravity, we utilise a pulsed CO_2 laser (with 10.6 μm emission line) to melt a commercial, single-mode optical fiber. The absorption of mid-infrared light heats the glass fiber as to raise its temperature above the glass melting temperature. One end of the fiber is held in tension by the weight of a small ceramic ferrule and a stem is made by tapering to a width of 10 μm for a length of 500 μm, at which point a sphere (cf. Figure 3.3a) is formed after severing by irradiation with a high-power cycle. At a sphere diameter of 80 μm and at probing wavelength $\lambda = 780$ nm, a balance is struck between the radiation and absorption losses in the WGM; it is therefore advantageous to achieve this cavity size to optimise sensitivity [90]. The suspended sphere-stem is then lowered into a chamber bounded by a U-shaped polydimethylsiloxane layer sandwiched between an N-SF 11 coupling prism and glass window.

A condensed schematic of the sensor setup is shown in Figure 3.3b. Light is focused onto the back face of a prism to couple to and from the cavity's WGMs, while the optical transmission is captured within the output arm of the setup. A fundamental WGM resonance of the microcavity is located in the transmission spectrum and monitored using LabVIEW software. The Lorentzian resonance dip of Figure 3.4a is tracked using a centroid method with fixed transmission threshold [93, 101], wherein the threshold is the green horizontal line overlayed onto the spectrum. The WGM scattering pattern on the microsphere, e.g. the distribution of lobes, that is seen through the camera allows for classification of the WGM with regard to its polar extent $l - m$. Although split modes can appear as in Figure 3.4a

and can be dissected in real time into two separate sets of traces for the split mode pair, the overall resonance lineshape is tracked to avoid tracking errors due to fluctuating splitting and/or transmission depths.

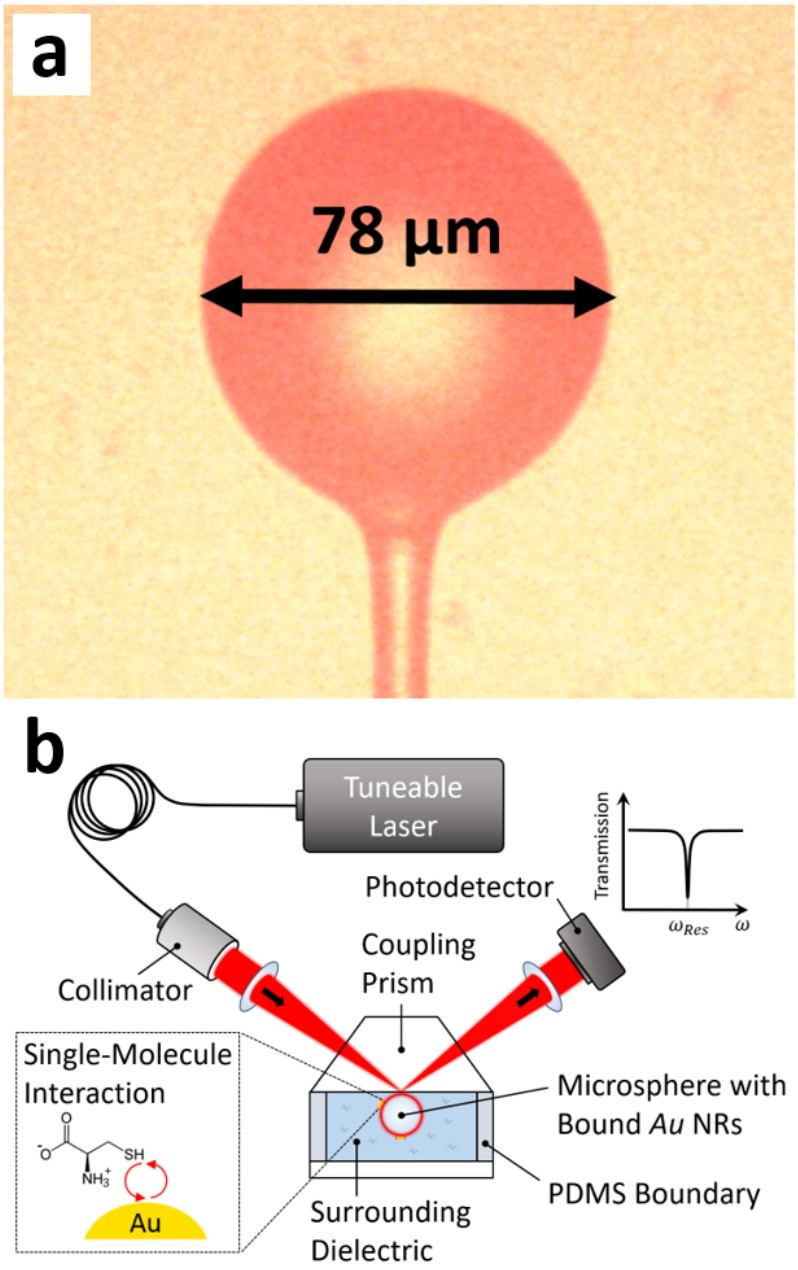

Figure 3.3: Microcavity fabrication and the hybrid photonic-plasmonic resonator based sensing platform. (a) A typical silica WGM microsphere, with approximate radius of 39 μm, fabricated by CO_2 laser reflow. A red light-emitting diode illuminates the sphere and its stem as to provide image contrast. (b) Experimental setup for single-molecule detection.

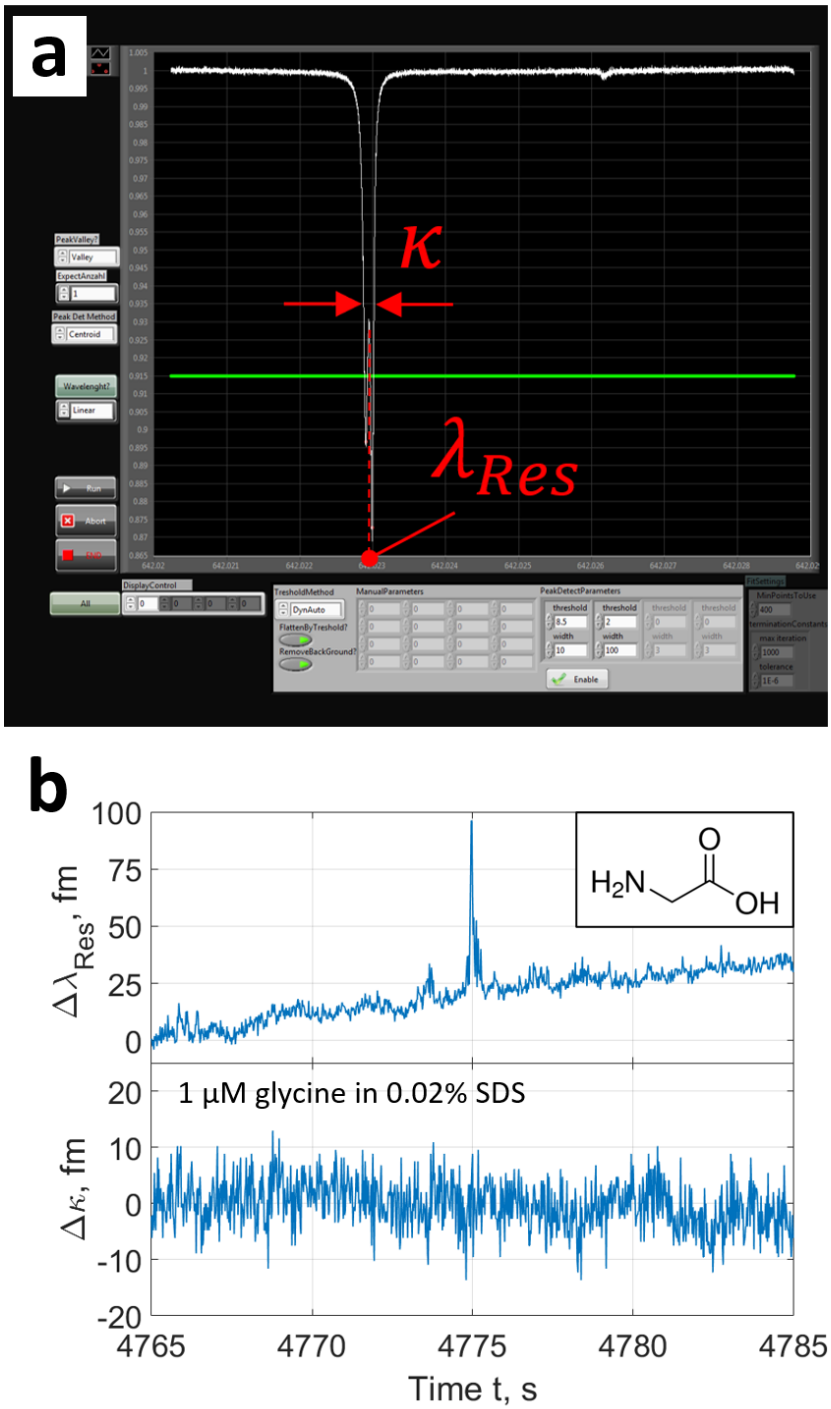

Figure 3.4: Optoplasmonic biodetection methodology. (a) Experimentally measured transmission spectrum and WGM resonance. (b) Single-glycine events in 0.02% SDS due to glycine diffusion near LSP-resonant plasmonic nanoannea coupled to the WGM. Note that this trace is not yet been detrended to remove noise such as thermal background drift.

At pM concentrations in aqueous solution, gold nanoparticles may be deposited onto the microcavity surface as nanoantennae (i.e. Figure 2.5 of the previous chapter). This is often done through electrostatic absorption by lowering the environmental pH to reach the isoelectric point of glass. An accumulated loss of 50 fm in the resonance linewidth from adsorption was determined, over numerous experiments and regardless of nanoparticle type, to correlate to the number of detection sites necessary to resolve single-molecule events on the nanoantennae. Biomolecules with functional groups that interact with gold, such as the amino acid glycine, can then be mixed into the surroundings. Diffusion of 1 μM glycine in 0.02% sodium dodecyl sulfate (SDS) entails short-lived interactions with the gold nanoantennae as in Figure 3.4b. The spike packet with amplitude > 50 fm at $t = 4775$ s appears disproportionate for such a minute species with molecular weight of 75.07 g/mol. If these events are from single molecules, they follow Poisson statistics like in Figure 3.5 and the event frequency scales linearly with concentration. This surface nanochemistry will be further scrutinised, under more complex reaction pathways, in the chapters to come.

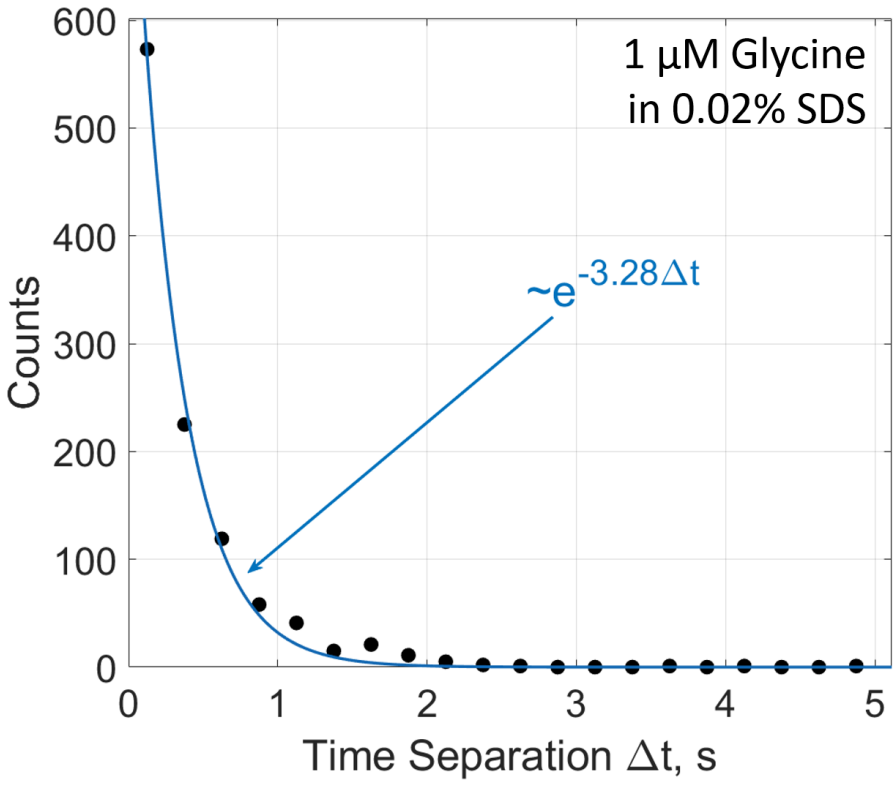

Figure 3.5: Poisson distribution for single-glycine transit events at gold nanoparticles of an optoplasmonic sensor.

Chapter 4

Chiral Detection

4.1 Origins of Chirality

All living organisms exhibit chirality. Louis Pasteur was aware of this over 170 years ago while studying tartaric acid, remarking that plane-polarised light rotated when passing through the crystalline acid [102]. Simpler molecules, such as hydrogen peroxide, can be chiral by virtue of the relative position of their atoms or their bond angles. Enantiomers or chiral molecule pairs have identical physical and chemical characteristics; however, when encountering other chiral substances, they begin to differentiate themselves in their interactions. Amino acids are left-handed and sugars are right-handed – perhaps the result of evolutionarily driven homochirality. The mathematical framework postulated for this development has included the likes of autocatalysis [103] or, in particular, Soai reactions with intensified enantioselectivity [104, 105]. Other sources have proposed that an extraterrestrial enantiomer excess arose due to exposure to infrared circular polarisation from ultraviolet light scattering off reflection nebulae in Orion OMC-1 [106]. This excess could have arrived on Earth via exogenous delivery, e.g. interplanetary dust particles, during the late heavy bombardment. Even the atom, a basic constituent one would be tempted to regard as achiral (i.e. a Dirac spinor's invariance under parity inversion), violates parity symmetry due to the nature of the weak nuclear force. In 1957, this was discovered by Wu *et al.* in a cobalt-60 decay experiment wherein $\sim$60% of gamma rays were emitted in one direction versus the other [107]. This was in clear violation of parity as the electron emission direction was biased relative to nuclear spin. Overall, chirality can exist on a fundamental interaction, molecular, or higher-order structural level. The prevalence and importance of chirality hence justifies technology capable of assessing it in a sophisticated way.

4.2 Methods for Measuring Chirality

The standard techniques for determining chirality are circular dichroism (CD) and optical rotary dispersion (ORD). In CD left- and right-hand circularly polarised light, abbreviated as LHC and RHC, is directed towards a chiral sample and an absorption difference

$$\Delta A = A_{LHC} - A_{RHC} \tag{4.1}$$

is measured. Since an electromagnetic wave's electric field linearly displaces charge and its magnetic field sets charge in circular motion, a electron inside this field would be compelled to trace a helical trajectory. The dipole moment operators acting on charged particles in effect create a permittivity/absorption discrepancy for LHC and RHC polarisation states of light. Figure 4.1 depicts a representative CD spectrum obtained for lysozymes in 10 mM sodium phosphate at pH 7.0 [108]. Wavelength selection allows for the probing of various structures or processes, such as proton-coupled electron transfer in the ultraviolet to visible range [109], d-d electron transitions in metals in the near-infrared [110], or investigations of a protein's three-dimensional structure in the infrared [111].

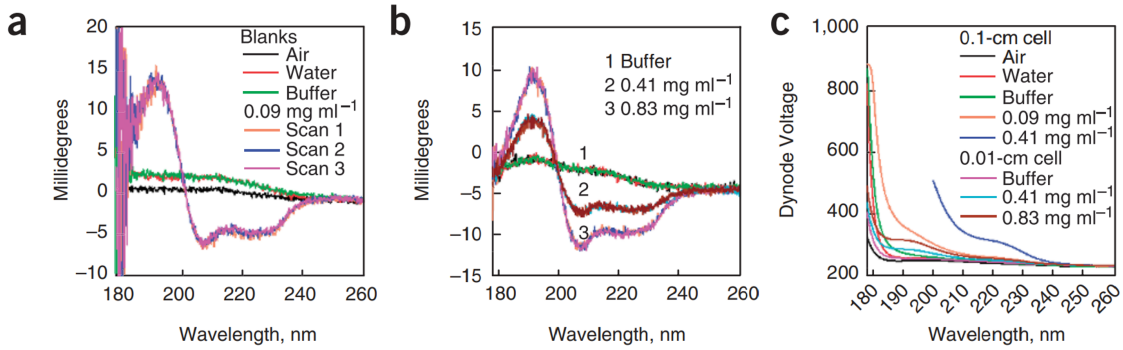

Figure 4.1: Background and lysozyme CD spectra. (a) CD spectra for air (black), water (red), sodium phosphate buffer (green), and lysoszymes at a concentration of 0.09 mg/mL (orange, blue, and magenta) in a 0.1-cm cell. (b) CD spectra of the buffer (black, red, and green) and lysozymes at a concentration of 0.41 mg/mL (purple, cyan, and brown) and 0.83 mg/mL (orange, blue, and magenta) in a 0.01-cm cell. The measured CD is reported as ellipticity, wherein the mean residue ellipticity $\Delta\varepsilon = [\theta]/3298$ can be calculated from the molar ellipticity $[\theta]$ = millidegrees / (path length $\times$ concentration of protein $\times$ number of residues). (c) Photomultiplier tube dynode voltage versus wavelength for different cell conditions. These data curves belong to [108].

ORD instead involves linearly polarised light, i.e. a linear superposition of two opposite but equally contributing circularly polarised components, making use of circular birefringence

$n_{LHC} - n_{RHC}$ to collect a rotation angle

$$\phi_c = (n_{LHC} - n_{RHC}) \frac{\pi l}{\lambda} \tag{4.2}$$

when passing through a chiral sample of length l at an optical wavelength λ. Recent alternatives for chiral detection have emerged as well, using photoionization [112], femtosecond laser pulses [113], and superchiral fields [114]. Chiral quantification can reveal information about protein folding, that is, conformational changes such as those from heat treatment, pH, or denaturants.

Despite the widespread use of these methods, CD and ORD have small signals that can be buried beneath spurious birefringence and prone to inadequate background suppression. A chiral sensitivity of about 1 μg/mL with a time resolution of 1 min. is typical [115]. It is therefore imperative that improvements, like successive instances of symmetry breaking to isolate for the signal of interest, be implemented to broaden applications and push the field towards single-molecule chirality.

4.2.1 Open Cavity Ringdown Polarimetry

To increase the specific rotation acquired from a sample, one can introduce a cavity geometry. For a stream of photons this equates to adding mirrors to intercept the stream and promote repeated interaction with the chiral species. A high-finesse bowtie ring cavity, in contrast to a two-mirror cavity, can achieve this by permitting light to counterpropagate and to reach 1000's of cavity passes [116, 117]. If a Faraday rotator is then placed in the second arm of the cavity, what we call a "signal reversal" (i.e. the switching of the magnetic field direction via a strong electromagnet) can be applied to generate two Faraday rotations that are equal but opposite in sign ($\pm\theta_F$). Irrespective of the sign of the longitudinal B-field, the total angle accrued per pass is $\theta_F \pm \phi_c$ wherein ϕ_c depends on the propagation direction. This strategy published by Rakitzis *et al.* (cf. Figure 4.2) with a pulsed laser offers multiple degrees of symmetry breaking with rapid channel subtraction and without sample removal. The Faraday rotation is reciprocal while the optical activity is non-reciprocal. An exponential decay envelope of the oscillating intensity is measured at two separate detectors in the time domain, a shift in the oscillation frequency for which gauges chirality. Over the round-trip cavity length L, these angular frequencies $\omega_{CW}(\pm B) = (\pm\theta_F + \phi_c)c/L$ and $\omega_{CCW}(\pm B) = (\pm\theta_F - \phi_c)c/L$ for polarisation rotation can be subtracted such that $\Delta\omega(\pm B) = |\omega_{CW}(\pm B)| - |\omega_{CCW}(\pm B)| = \pm 2\phi_c c/L$. The chiral signature is then quadrupled to $\Delta\omega(+B) - \Delta\omega(-B) = 4\phi_c c/L$ per pass. Signal reversals with this setup were performed for (+)- and (-)-α pinene vapours, with or without pressure control, as well as for maltodextrin, fructose, and glycerol-water solutions

flowed over a prism [118]. Locking of a continuuous-wave laser to a stable cavity of this type renders subnanolitre volumes dectectable, eventually towards shot-noise limits of 3×10^{-13} rad [119].

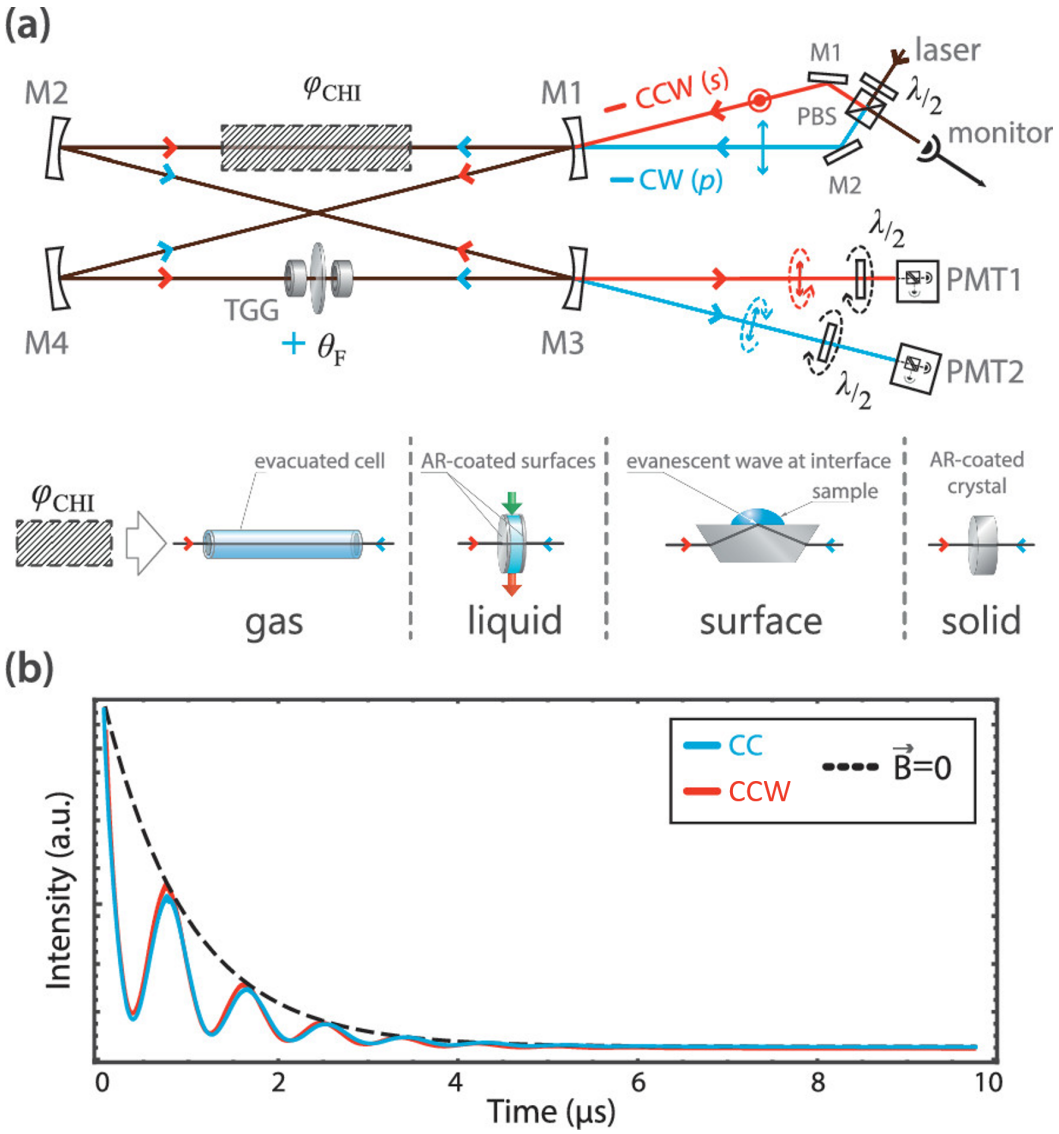

Figure 4.2: Ensemble chiral sensing with open cavity ringdown polarimetry. (a) Schematic of the polarimeter with a Faraday rotator consisting of a terbium gallium garnet (TGG) crystal. As for an evanescent wave probing a chiral medium in the prism configuration, the Goos-Hänchen shift converts into optical rotation. (b) Ringdown signals for the clockwise (CW) and counterclockwise (CCW) rotating beams. When the B-field is set to 0, a pure exponential decay is recorded as to calculate total cavity losses. For large $B > 0.1$ T, polarisation beating is observable. These technical drawings were published in [120].

4.2.2 Intracavity Faraday Effect

From the onset of my PhD research, we had planned to transpose chiral polarimetry to the optical WGM resonator in an attempt to resolve single-molecule chirality. The magneto-optic Faraday effect in matter relates an applied magnetic field of strength B to the polarisation rotation θ_F of the oscillation plane of polarised light when $\vec{B}$ is parallel/antiparallel to the propagation direction. A linear proportionality $\theta_F = vBl$ exists where v is the material's Verdet constant and l is the length of the path traversed through said material. The magnetic permeability tensor is nondiagonal here and, in principle, the effect should be transposable to the optical WGM with its curvilinear coordinate system. Comparing this geometry to the open cavity ringdown polarimeter, there are a few immediately identifiable differences: an evanescent field is present along the entire path length and Faraday rotation is continuous over the course of the photon lifetimes. Bidirectional propagation in the bowtie cavity is also mimicked by mode splitting. The predictive model of the Faraday effect in a ultahigh-Q WGM resonator has been formulated using coupled mode theory [121]; however, unlike light in an unconstrained geometry, there are quasi-TE and quasi-TM modes in the microcavity that are inherently nondegenerate [122]. Modal intensity profiles are dominated by a major field component that is either parallel or perpendicular to the cavity interface. The dielectric boundary conditions result in different penetrations depths into the external medium and thus there is a geometrical birefringence $\Delta n_g = n_{TE} - n_{TM}$ that severely quenches the rotation θ_F at the coupler. If we consider the input and output fields at the coupling junction in terms of x (TE) and y (TM) components, we can calculate the rotation due to a B-field tangential to the optical path from the closed-form matrix equation [121]:

$$\begin{bmatrix} E_{out}^x \\ E_{out}^y \end{bmatrix} = \begin{bmatrix} t - |\kappa|^2 \left[f(\theta,\gamma) - i\frac{\Delta\beta}{\phi} g(\theta,\gamma) \right] & |\kappa|^2 \frac{2F}{\phi} g(\theta,\gamma) \\ -|\kappa|^2 \frac{2F}{\phi} g(\theta,\gamma) & t - |\kappa|^2 \left[f(\theta,\gamma) + i\frac{\Delta\beta}{\phi} g(\theta,\gamma) \right] \end{bmatrix} \begin{bmatrix} E_{in}^x \\ E_{in}^y \end{bmatrix} \quad (4.3)$$

as we define the phase shift per round trip $\theta = 4\pi^2 na/\lambda$, loss factor $\alpha_L = \exp\left[-2\pi^2 na/(\lambda Q_0)\right]$, Faraday rotation per unit length $F = vB$, quenching $\Delta\beta = 2\pi\Delta n_g/\lambda$, and remaining terms

$$\phi = 2\sqrt{\left(\frac{\Delta\beta}{2}\right)^2 + F^2} \quad (4.4)$$

$$\gamma = \pi\phi a \quad (4.5)$$

$$f(\theta,\gamma) = \frac{\alpha_L e^{-i\theta}\cos(\gamma) - \alpha_L^2 e^{-i2\theta}}{\left(\alpha_L e^{-i\theta} t^*\right)^2 - 2\alpha_L e^{-i2\theta} t^* \cos(\gamma) + 1} \tag{4.6}$$

$$g(\theta,\gamma) = \frac{\alpha_L e^{-i\theta}\sin(\gamma)}{\left(\alpha_L e^{-i\theta} t^*\right)^2 - 2\alpha_L e^{-i2\theta} t^* \cos(\gamma) + 1} \tag{4.7}$$

for an effective refractive index n and cavity diameter $2a$. We assume coupling is lossless, so the complex transmission t and coupling κ coefficients are related via $|t|^2 + |\kappa|^2 = 1$.

4.2.3 Publication I on a Geometrical Birefringence Reduction Scheme

In the next section, a manuscript that compiles experiments on the Faraday effect in WGM resonators is presented [23]. Two composite glasses with non-negligible Verdet constants were tested as cavity materials in terms of their glass transition when heated by convection: tellurite ($78TeO_2$-$12ZnO$-$10Na_2O$) and germanate ($56GeO_2$-$31PbO$-$9Na_2O$-$4Ga_2O_3$). The constituent with greater atomic number, i.e. TeO or PbO, is responsible for raising the composite's Verdet constant while stability is obtained from the overall composition of the glass. These soft glasses were initially drawn into capillary fibres by our collaborators. In order to later provide conduction based tuning and induce local magnetic fields, we inserted metallic conducting wires (e.g. tungsten, copper, silver, or gold) inside the capillaries prior to microcavity preparation. A current-controlled CMH-7019 ceramic microheater was employed to melt the fibre tip with protruding wire — a procedure further detailed in Appendix B. During heating protocols, the tellurite crystallised due to nucleation sites that developed near the metal-glass interface. For the majority of heating rates, germanate capillaries (with inner gold wires) successfully melted into droplets in the microheater with a desirable isotropy near their surface. One of these cavity-wire structures was integrated onto a biasing chip, then installed in a modified sensor setup with a titanium dioxide prism coupler. Quasi-TE and quasi-TM WGMs were thermally tuned as to minimise geometrical birefringence and to amplify the Faraday effect. The platform was developed by the thesis author, experiments were also designed and performed by the thesis author, the soft glass capillaries were fabricated by Xian Jiang in Philip Russell's research group, and Frank Vollmer surpervised the work. The thesis author wrote the manuscript with editorial contributions from all authors.

4.3 Thermally Tuneable Whispering-Gallery Mode Cavities for Magneto-Optics

Serge Vincent*, Xin Jiang†, Philip Russell†, and Frank Vollmer*

*Living Systems Institute, School of Physics, University of Exeter, Exeter EX4 4QD, UK
†Max Planck Institute for the Science of Light, Staudtstrasse 2, 91058 Erlangen, Germany
Email: sv316@exeter.ac.uk; f.vollmer@exeter.ac.uk

Abstract

We report the experimental realisation of magneto-optical coupling between whispering-gallery modes in a germanate (56GeO2-31PbO-9Na2O-4Ga2O3) microspherical cavity due to the Faraday effect. An encapsulated gold conductor heats the resonator and tunes the quasi-transverse electric (TE) and quasi-transverse (TM) polarized modes with an efficiency of ∼65 fm/V at a peak-to-peak bias voltage of 4 V. Signal parameters for a number of heating regimes are quantified to confirm sensitivity to the generated magnetic field. The quasi-TE and quasi-TM resonance frequencies stably converge near the device's heating rate limit (equivalently, bias voltage limit) in order to minimise inherent geometrical birefringence. This functionality optimises Faraday rotation and thus enables the observation of subsequent magneto-optics.

Introduction

Optical devices that exploit whispering-gallery modes (WGMs) have gradually become ubiquitous [123]. The WGM cavity has demonstrated strong optomechanical interactions [124, 63], lased at ultralow thresholds [28], established parity-time symmetric systems [60], and detected single atomic ions near plasmonic nanoantennae [93]. Tuning of WGMs outside of irreversible modification [125, 126] has been achieved by refractive index modulation, such as from mechanical strain/pressure [127, 128, 129, 130], electro-optics [131, 132, 133], or thermal effects [134, 135, 136, 137, 138]. Thermo-optical control is typically realised by selecting a high-thermo-optic coefficient material for the cavity [136, 137] or relying on absorption based heating [134, 135], wherein the former involves an integrated heating element. Tuning of glass WGM cavities through an internal metallic conductor, however, can be intractable due to glass crystallisation during fabrication. While melting the dielectric at a temperature below the conductor's melting point, nucleation sites develop and with crystal growth inhibit WGM circulation. For sensing applications in a stochastic environment, there

is also a need for laser jitter suppression when detecting nanoparticles [139] and the removal of background drift when thermally characterising polymers [140].

By way of optomechanics and magnetostriction, on-chip WGM based magnetometers [141] have detected magnetic fields with sensitivities as small as 100's of pT/$\sqrt{\text{Hz}}$ [142]. More generally, magneto-optical coupling in a WGM resonator has been studied for transported magnetic fluids [143, 144] and for the resonator material itself [145]. Cavity optomagnonics in yttrium iron garnet (YIG) microspheres [146, 147] offers coherent magnon-to-photon interconversion at optical and microwave frequencies, justifying the use of magnons as information carriers. An applied magnetic field B modifies the cavity dielectric tensor by first and second order magnetisation, respectively known as the Faraday and Voigt effects [148]. The quasi-transverse electric (TE) and quasi-transverse (TM) magnetic WGM resonance frequencies are split by the cavity boundary conditions, i.e. by a geometrically induced birefringence Δn_g, and are mixed by the Faraday effect [121]. One conclusion that was drawn in [121] was that Δn_g quenches the overall Faraday rotation. Minimising Δn_g in turn maximises the magnetic field sensitivity and so polarisation rotation at the output coupler becomes significant. Cavity-enhanced polarimetry [118] is an extension of this operational principle through which chiral measurement can be considered.

In this paper, we present a WGM sensing platform that dually incorporates thermal tuning and magneto-optical responsivity. A germanate (56GeO2-31PbO-9Na2O-4Ga2O3) microsphere with high Verdet constant is fabricated with a central gold conducting wire to modulate the WGM resonance via heating and induce a magnetic field on the order of 1 G. The cavity-wire structure is fashioned by inserting a sub-millimetre diameter gold wire into a germanate capillary, then a capillary segment with wire protrusion is melted inside a ceramic microheater. Convection and surface tension promote the formation of a germanate microspherical profile around the wire (with cavity radius on the order of 100's of μm) and glass isotropy is ensured by the germanate's slower crystallisation rate. The wire geometry creates a B-field that is parallel or antiparallel to the WGM propagation direction throughout current reversal in time. Critically, as the cavity refractive index (n_c) profile guides quasi-TE and quasi-TM modes differently, we show that Δn_g decreases with thermal conductance throughout the cavity with increasing root-mean-square amplitude of the oscillating bias voltage. This WGM tuneability scheme excludes large and expensive electromagnets in order to limit the device footprint.

Results

Scans were performed across WGM resonances using a tuneable external cavity laser of central wavelength $\lambda = 642$ nm in the geometry shown in Figure 4.3. Light is focused onto

the internal surface of a rutile prism and, through frustrated total internal reflection, couples to the germanate microsphere at 5% efficiency in order to excite WGMs. We note that the prism is birefringent with ordinary refractive index n_o and extraordinary refractive index n_e above that of the germanate ($n_c < 2 < n_o < n_e$) within the chosen optical bandwidth. The WGM microsphere in contact with this prism is doubly-clamped above a metal-on-insulator biasing chip (Figure 4.3a) and the enclosed 150-μm diameter gold wire supports actuating currents of up to a few amperes.

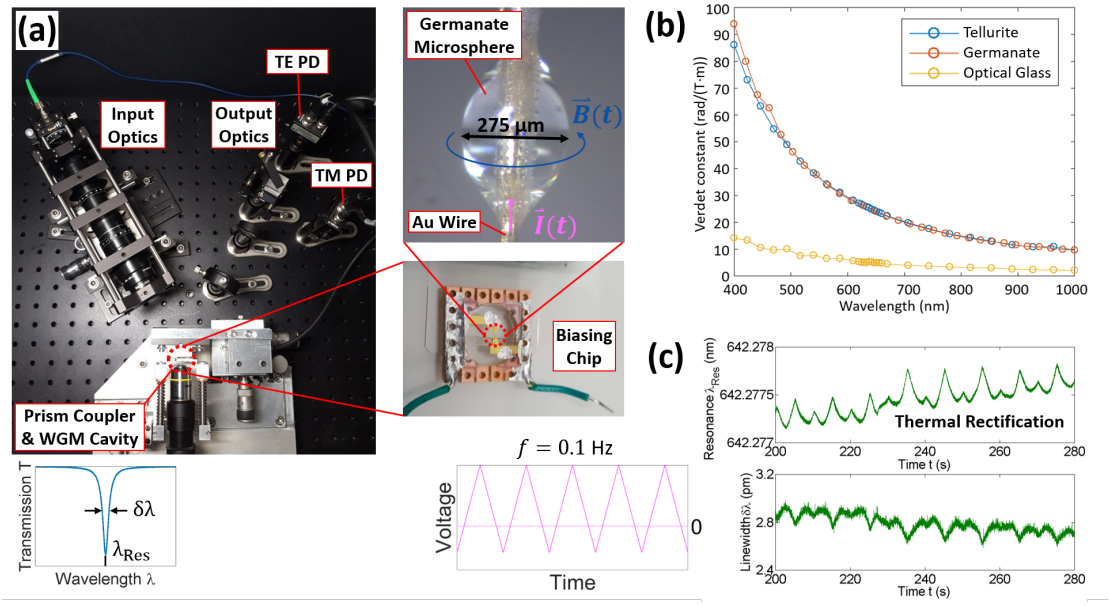

Figure 4.3: WGM excitation in a magneto-optical microsphere with a confined conductor. (a) Experimental setup. (b) Measured Verdet constant spectra for optical and soft glasses. (c) Device operation with a triangular wave current input. Heat generated by the electrical conductor results in a WGM resonant wavelength shift proportional to the square of the voltage, such that the resonance oscillation frequency is exactly twice that of the current when there is no DC offset.

Spectral characterisation of the germanate's Verdet constant (Figure 4.3b) determined a value of ~25 rad/(T·m) near WGM resonances. Nevertheless, initial peak tracking of the resonance lineshape in Figure 4.3c for a triangular bias voltage $V(t)$ suggests dominant thermal influences. In principle, for a local temperature change ΔT, signal rectification arises from Joule heating:

$$\Delta\lambda_{Res}(t) \propto \Delta T(t) \propto V^2(t) \tag{4.8}$$

Linewidth narrowing and broadening follows the heating cycle with a π phase delay with respect to the resonant wavelength λ_{Res}. When the suspended microsphere contacts the prism, forces acting on the sphere-stem cantilever [149] from capacitance at the soft glass interface and flexion from heating can vary the coupling to the WGM and hence alter the linewidth. The magnetic field oscillation frequency f_M is not equal to that of the recorded response of Figure 4.3c — what is instead observed is a WGM perturbation at $2f_M$ due to heat conduction that is independent of current direction. The trace's noise floor in the 10's of fm range, in this case derived from the cavity quality factor $Q = \lambda_{Res}/\delta\lambda \approx 2 \times 10^5$, exceeds the laser phase noise.

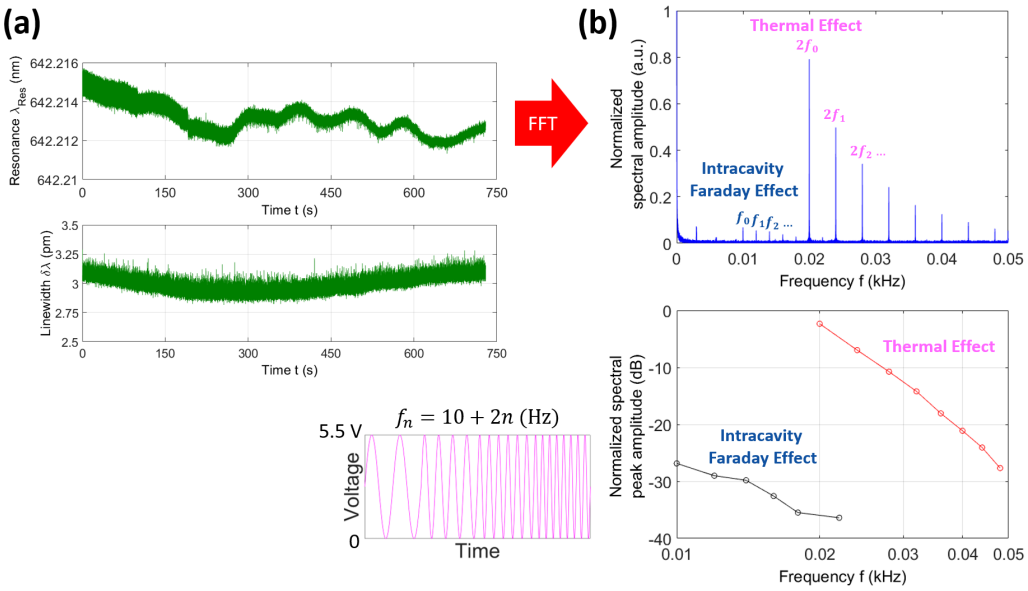

Figure 4.4: Fast Fourier transform (FFT) of the WGM resonance response to frequency ramping. (a) Time trace for a sinusoidal current input. The oscillation frequency is increased from 10 to 24 Hz in discrete steps of 2 Hz. (b) Fourier spectrum and semi-log plot of the normalised spectral amplitude versus frequency.

Further investigation of the perturbed WGM resonance was carried out by frequency domain analysis. The entire resonance trace of Figure 4.4a was decomposed into its frequency components (Figure 4.4b), revealing the expected DC component and $2f_M$ peaks for a full-wave rectified resonance signal response. These peaks originate from thermal nonlinearities; however, f_M peaks also exist within the spectrum. Normalised spectral peak amplitude versus frequency curves in Figure 4.4b for the two separate series of peaks differ in bandwidth, thus indicating separate time constants. The model proposed in [121] derived from coupled mode theory contextualizes this disparity: once the B-field is sufficient to overcome the geometrical birefringence Δn_g, mode mixing produces deviations in quasi-TE and quasi-TM WGM

eigenfrequencies away from degeneracy. Consequently, a partial-wave rectified resonance shift pattern from a weak intracavity Faraday effect would exhibit the f_M peak seen in our experiment. With lower Δn_g, coupling between quasi-TE and quasi-TM WGMs is detected at lower magnetic field thresholds.

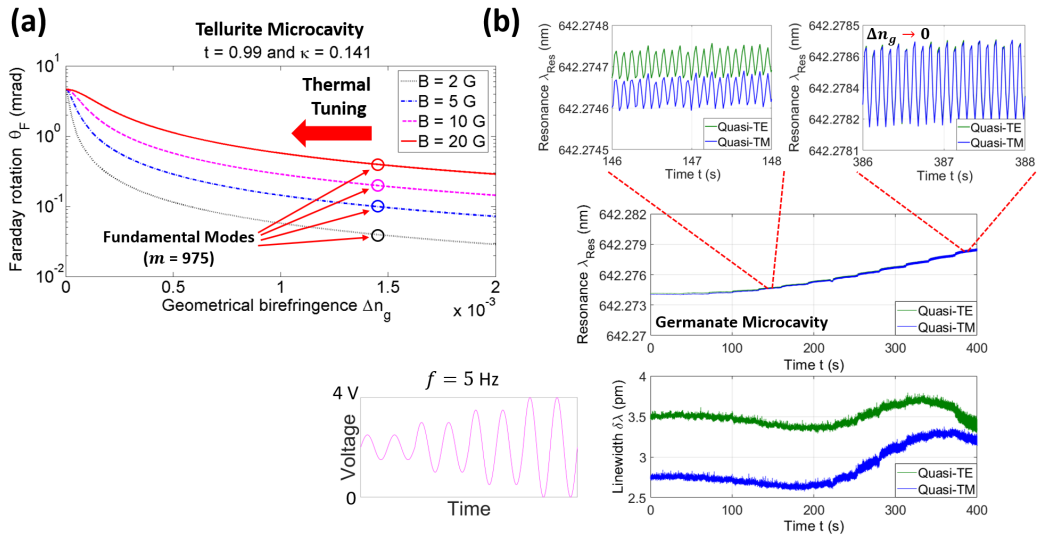

Figure 4.5: Thermal tuning of quasi-TE and quasi-TM WGMs to minimise geometrical birefringence. (a) Computed Faraday rotation versus geometrically induced birefringence for a 50-μm radius tellurite microspherical cavity. The transmission coefficient t =0.99 and coupling coefficient κ =0.141 match simulations from [121]. (b) Converging quasi-TE and quasi-TM WGM resonant wavelengths with increasing amplitude of the sinusoidal current input. Note that the resonant wavelength traces are in-phase.

Faraday rotation θ_F is optimised in the unquenched regime ($\Delta n_g = 0$) and is highly dependent on the magnetic field strength. Calculations in Figure 4.5a outline that θ_F and hence the shift $\Delta\lambda_{Res}$ for a tellurite WGM microsphere are linear with the B-field. Simulated fundamental quasi-TE and quasi-TM WGMs with azimuthal mode order $m = 975$ (i.e. near the experimental operating wavelength) places the operating points at $\Delta n_g = 0.00146$, neglecting the cavity index profile variation from thermo-refractivity and thermal expansion. Accounting for this tuning, on the other hand, can lead to displacement in the radial position of the guided WGM intensity maxima. Figure 4.5b depicts the experimental resonance trace when increasing the root-mean-square amplitude of the bias voltage. By fixing the duty cycle of the electrical signal, the time-averaged heating of the microsphere enforces a radial thermal gradient that equalises the quasi-TE and quasi-TM WGM eigenfrequencies. These modes begin with different penetration depths into the external dielectric and with precise thermal feedback may converge towards minimal geometrical birefringence. At a

peak-to-peak bias voltage $V_{pp} = 4$ V the tuning efficiency reaches ∼65 fm/V and the modes differ in resonant wavelength by less than 1 pm. The amplitude of in-phase shift $\Delta\lambda_{Res}$ for these modes scales linearly with V_{pp} and the signal undergoes a steeper rise towards the peak, in agreement with thermal and intracavity Faraday effect superposition. WGM resonant linewidths are similar in oscillation and close in value (≤ 0.5 pm at $V_{pp} = 4$ V), remaining synchronous irrespective of the superimposed perturbations.

Conclusion

The findings in this study provide preliminary evidence for the optical WGM resonator analogue of polarisation rotation in a soft glass cavity. A cost-effective microheater with electrical interfacing was used to tune the WGM resonances and reduce geometrically induced birefringence. The latter enhances the quasi-TE and quasi-TM polarisation coupling per round-trip in the presence of a proximate magnetic field aligned with mode propagation. Magnetisation dynamics could be explored, such as the possibility of lasing by way of magnon Brillouin scattering. Nonreciprocal Brillouin scattering can bring selective creation and annihilation of magnons in the Kittel mode, alongside chiral features embedded in the spin dynamics of a ferromagnetic YIG microcavity [146, 147]. Due to the solubility of the germanate glass, any WGM measurement in solution may require the coating of a protective layer (e.g. a perfluoro(1-butenyl vinyl ether) polymer) around the cavity. By satisfying this criterion we anticipate future chiral sensing of enantiomers layers on the cavity surface. Distinguishing the chirality of and detecting Faraday rotation from single molecules will, however, necessitate greater specificity and signal enhancement. Single-molecule chirality is largely unattainable in cavity polarimetry schemes [118] as the requisite resolution falls below the shot noise. A signal-reversing WGM biosensor based on the intracavity Faraday effect may circumvent this pitfall by isolating for a weak yet local chiral signal. This is afforded by exceptional points [60] and/or mode hybridisation through coupling to localised surface plasmons of metallic nanoparticles [93]. Plasmonic nanoantennae from [93] may be functionalised with organic molecules possessing a substantial Verdet constant (e.g. 1,3,5-trimethyl-2,4,6-tris[2-(4-nitrophenyl)ethynyl]benzene/TTB [150]), as they would be individually detectable and responsive to magnetic field fluctuations in the optoplasmonic system. Another promising avenue is the detection of magnetic field-dependent protein behaviour, such as cryptochrome signalling [151]. Spin states correlated to such biochemical reactions could be manipulated with the local magnetic field and probed according to the magneto-optical coupling of the resonator, i.e. through resolvable discrepancies between the quasi-TE and quasi-TM WGM resonance response.

Acknowledgements

The authors would like to thank Rémy Soucaille for his contribution in characterising the glasses' Verdet constants. S. V. also thanks Peter Rakitzis and Matthew Foreman for their valuable discussions. Resonance peaks in the measured spectra were tracked and analysed using software developed by Martin Baaske. This work was supported by a H2020 FET Open grant (ULTRACHIRAL, ID: 737071) issued by the European Research Council.

4.3.1 Comments on Publication I

Considerable design challenges were raised for the immersion of the cavity-wire sensor in liquid, as they also were for a chamber that contains a gas around the system. These factors combined with a limited Faraday effect contribution to the signal response encouraged a direct approach to chiral discrimination: optoplasmonics with chiral plasmonic nanoantennae. We soon set off towards characterising molecular chirality by optoplasmonic detection, given that the technique was grounded in single-molecule interrogation. Fundamentally, a chiral interaction is mixed in terms of the electric and magnetic dipole moments

$$\vec{p}_e = \alpha\vec{E} - i\xi\vec{B} \tag{4.9}$$

$$\vec{p}_m = \chi_m\vec{B} + i\xi\vec{E} \tag{4.10}$$

with a mixed electric-magnetic dipole polarisability ξ, connected to the optical chirality factor [152]:

$$C = -\frac{\varepsilon_o\omega}{2}\mathrm{Im}\left\{\vec{E}^* \cdot \vec{B}\right\} \tag{4.11}$$

Probing chirality with light therefore benefits from having the E- and B-field be out of phase by $\pm\frac{\pi}{2}$, aligned, and proportionately large. The time-even pseudoscalar quantity C switches sign under parity inversion similar to how a chiral molecule's handedness switches when it is mirrored. A circularly polarised electromagnetic wave, for example, has

$$C_\pm = \pm\frac{\varepsilon_o\omega}{2c}E_0^2 \tag{4.12}$$

where $+$ is the left-handed and $-$ is the right-handed variant. A standing wave pattern formed by counterpropagating beams with these polarisations produces so-called superchiral light, with enantioselectivity surpassing $|C_\pm|$. The suggestion at this stage was whether the chiral near fields of a plasmonic nanoparticle could resolve the chirality state of a single molecule.

Chapter 5

Chiral Gold Nanoparticles for Sensing Chiral Molecules

5.1 Plasmonic Nanoparticles Synthesised by Biomolecules

To list but a few options, chirality in plasmonics can stem from helicity [153, 154], planar chiral metamaterials [155], chiral stacks made up of achiral or chiral nanostructures [156, 157], the ordering of nanorods in a scaffold [158, 159], or gold nanoparticles arranged via DNA origami [160, 161]. One type of nanoparticle with unusual dissymetry factor ≈ 0.2 ($\propto$ the ratio of the circular dichroism to extinction value) at $\lambda = 622$ nm is the 432 helicoid III with pinwheel-like crevices on each of its faces [24]. During synthesis, it was reported that amino acids and peptides may interact with the nanoparticle surfaces enantioselectively to impart asymmetric growth and to form chiral helicoid morphologies. Finite-difference time-domain simulations of a gold 432 helicoid III cube in Figure 5.1 had confirmed the nanoparticle's CD spectral response and associated near fields. As there are detection sites with overlapping B- and E-field enhancements near 642 nm in Figure 5.1h and 5.1i, implementing 432 helicoid III as a chiral nanoantenna for our optoplasmonic sensor was considered. A far-field CD measurement is related to the near-field optical chirality factor C through the absorption rate's proportionality to $\mathrm{Im}\left\{\vec{E}^* \cdot \vec{B}\right\}$, hence chiral states of single biomolecules may be locally resolvable on the nanoparticle. In regions of the gold 432 helicoid III's near field where $\vec{E}^* \cdot \vec{B}$ is amplified, the signal responses from an enantiomer pair (with nonzero mixed polarisabilities) should diverge from one another. Nanoparticles modified with enantiomeric recognition and separation can also constrict analytes to selective surface coordination due to homochiral interactions. An $\vec{E}^* \cdot \vec{B}$ optimum can be targeted to

enhance C while adapting surface chemistry protocols from our group's past work [22, 93, 162, 163].

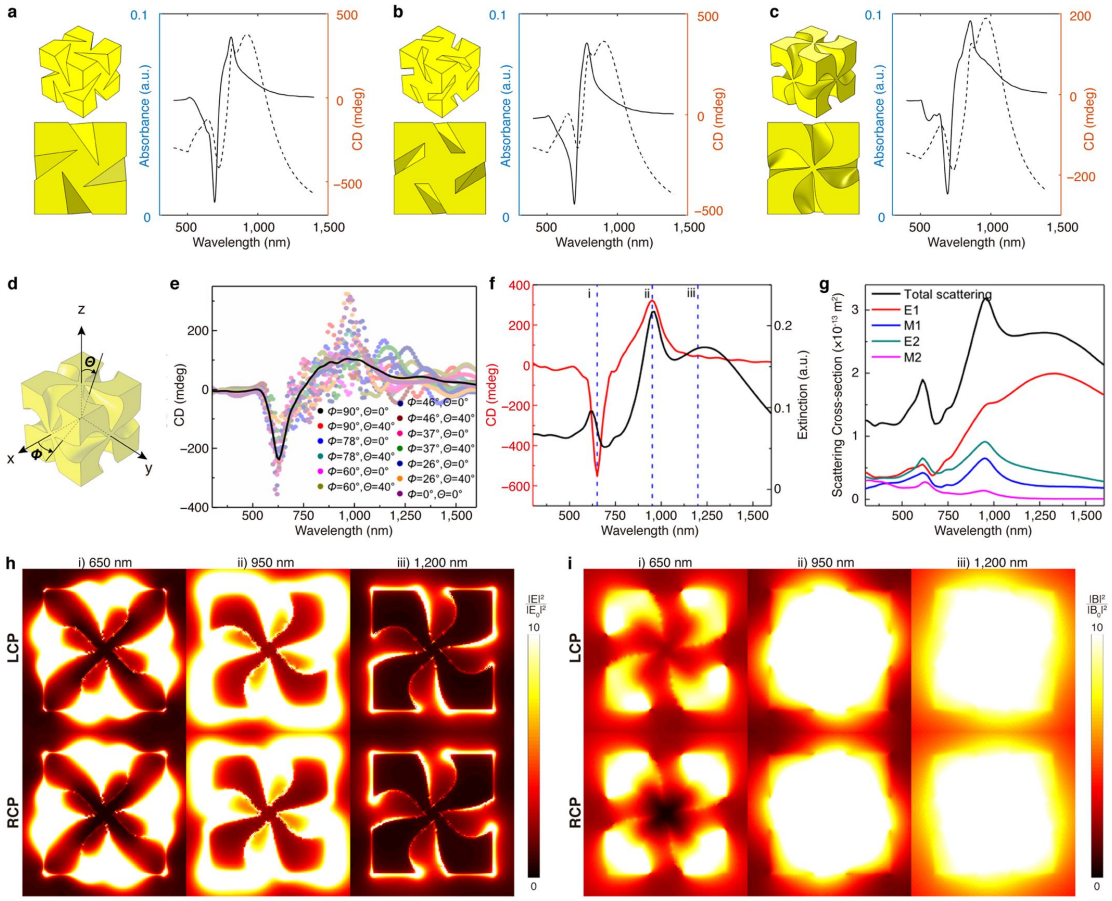

Figure 5.1: Simulated optical response of 432 helicoid III. (a)-(c) Computed absorption and CD spectra for (a) triangular, (b) rectangular, and (c) curved crevices. (d) A 3D model for case (c). (e) CD spectra for particular (dots) and averaged (solid line) nanoparticle orientations. (f) Absorbance and CD values for normal incidence. (g) Multipole analysis of the scattering cross section, with electric dipole mode (E1) near 1,200 nm, and magnetic dipole mode (M1) and electric quadrupole mode (E2) near 650 nm and 950 nm. (h)-(i) Normalised intensity distributions for the electric and magnetic fields at normal incidence for $\lambda = 650$ nm, 950 nm, and 1,200 nm. These finite-difference time-domain simulations are published in [24].

5.2 Characterising Single Amino Acids

Our collaborator synthesised a set of gold 432 helicoid III nanoparticles with L-glutathione using octahedral seeds. These samples were dispersed in 1 mM cetrimonium bromide (CTAB) in water with a yield conveyed in Figure 5.2. CTAB micelles are formed around the

nanoparticles to sterically hinder agglomeration, maintaining the average nanoparticle side length of 200 nm and limiting deformity to a comparable extent as that in [24].

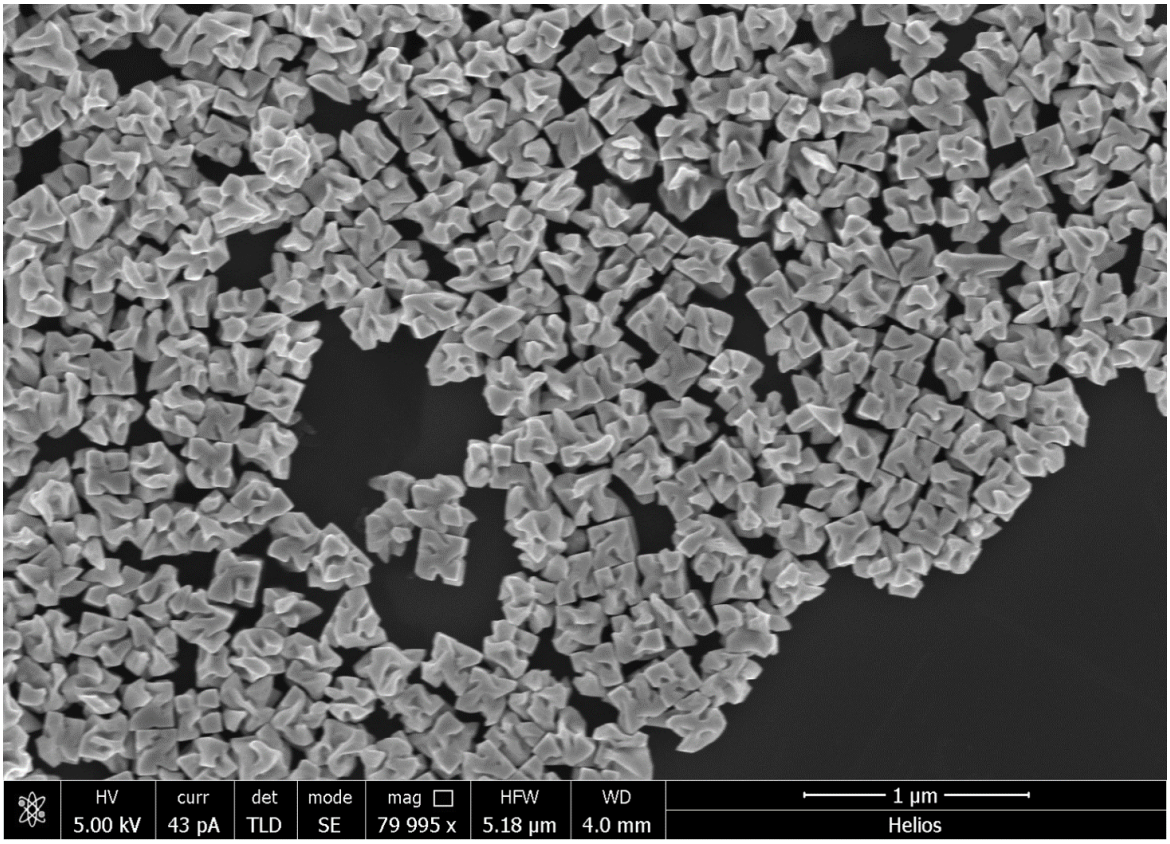

Figure 5.2: Scanning electron micrograph of gold 432 helicoid III nanoparticles. These structures were first shown in [24] to have a circular dichroism peak near 642 nm, indicative of a high chirality factor C.

Experiments were then initiated to investigate the interactions of small chiral molecules with these chiral gold nanoantennae on the optoplasmonic sensor. Under the same setup as that of Figure 3.3b, gold 432 helicoid III nanoparticles were deposited onto the microspherical cavity. A solution of 0.02% (w/w) SDS in water was chosen to facilitate molecular transport to the gold nanoparticles; nonetheless, the concentration was held below the critical micelle concentration = 0.2% (w/w) for SDS in water [164]. Once reducing agent was added to cleave the L-cystine dimers and the pH was lowered to an acidic value of $\sim$2.7, it was clear from Figure 5.3 that the charge of L-cysteine at 2 μM allowed it to bind as well as react transiently near the surface of the gold chiral nanoparticles. This is linked to the fact that cysteine contains thiol and amine groups that interact with gold, whose respective interaction probabilities can depend on the molecular charge and ionic strength.

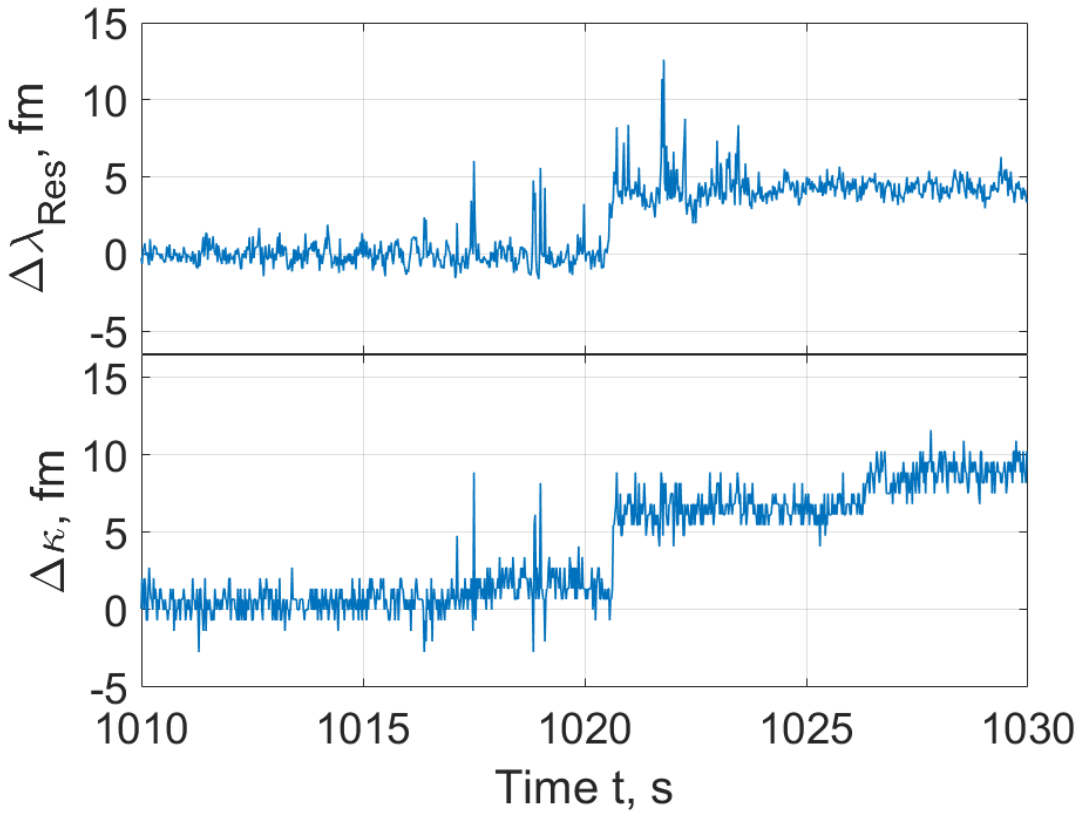

Figure 5.3: Single-molecule events involving 2 μM reduced L-cysteine reacting on a gold 432 helicoid III surface in 0.02% SDS and at pH < 3. Spike amplitudes are on the order of 10 fm.

Large signal amplitudes may be due to the nanoparticle size as well as the sharp edges of the nanoparticle, e.g. inside the crevices, resulting in a greater number of sites with anomolous local field enhancement. Single-molecule binding steps are principally correlated to L-cysteine forming a thiol-gold bond at an acidic pH. The large spike signals from surface reactions continuing throughout the trace have both linewidth broadening and narrowing as can be seen in Figure 5.4. Surprisingly, L-cysteine has a low molecular weight of 121.16 g/mol, i.e. a negligible excess polarisability per molecule, despite it measurably altering the resonance's λ_{Res} and κ. The gold 432 helicoid III has ordered facets and surface irregularities alike due to its extensive surface area, as compared to a nanorod with dimensions on the order of 10's of nm, thus ensuring surface reaction diversity.

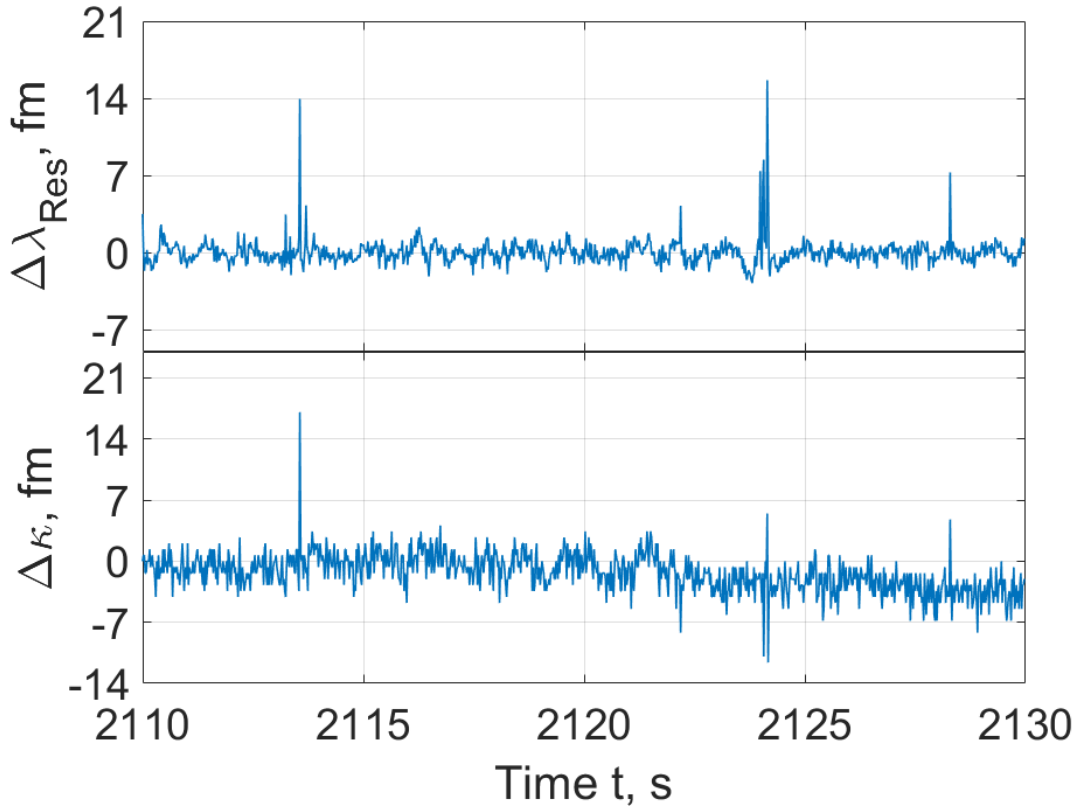

Figure 5.4: Transient interactions between 2 μM of reduced L-cysteine molecules diffusing to the detection sites on gold 432 helicoid III nanoantennae for 0.02% SDS and a pH < 3. The optoplasmonic resonance's linewidth change $\Delta\kappa$ can be either negative or positive.

While introducing a further 2 μM D-cysteine with excess TCEP, binding sites tend towards saturation and the LSP-WGM resonance linewidth κ begins to oscillate. Figure 5.5 shows a series of discrete steps in κ with consistent step height appearing in the trace over time. Dissolved oxygen molecules continuously oxidise thiols into disulfides, while TCEP reducing agent lowers the dimer population in solution. Cysteine can also bind to gold via its amine or thiol group, wherein the former results in an immobilised linker molecule with exposed thiol that can form the disulfide bonds. We can visibly see in Figure 5.5 that TCEP controls the number of electrostatically adsorbed dimers on the plasmonic nanoantennae by direct cleavage within the detection volume. It is important to note that one of the two sulfur atoms of a disulfide bridge can undergo reaction with the phosphorous atom of TCEP along a reduction pathway. This leaves the dwell times relatively random as the separate DL-cysteine/cystine and TCEP reactants are delivered by diffusion. Putting this scheme aside until Chapter 6, one might assume that analysing the optoplasmonic response of any

cyclical single-molecule interaction can provide encoded molecular characteristics, i.e. the chiral state of a participating cysteine molecule within the racemic mixture.

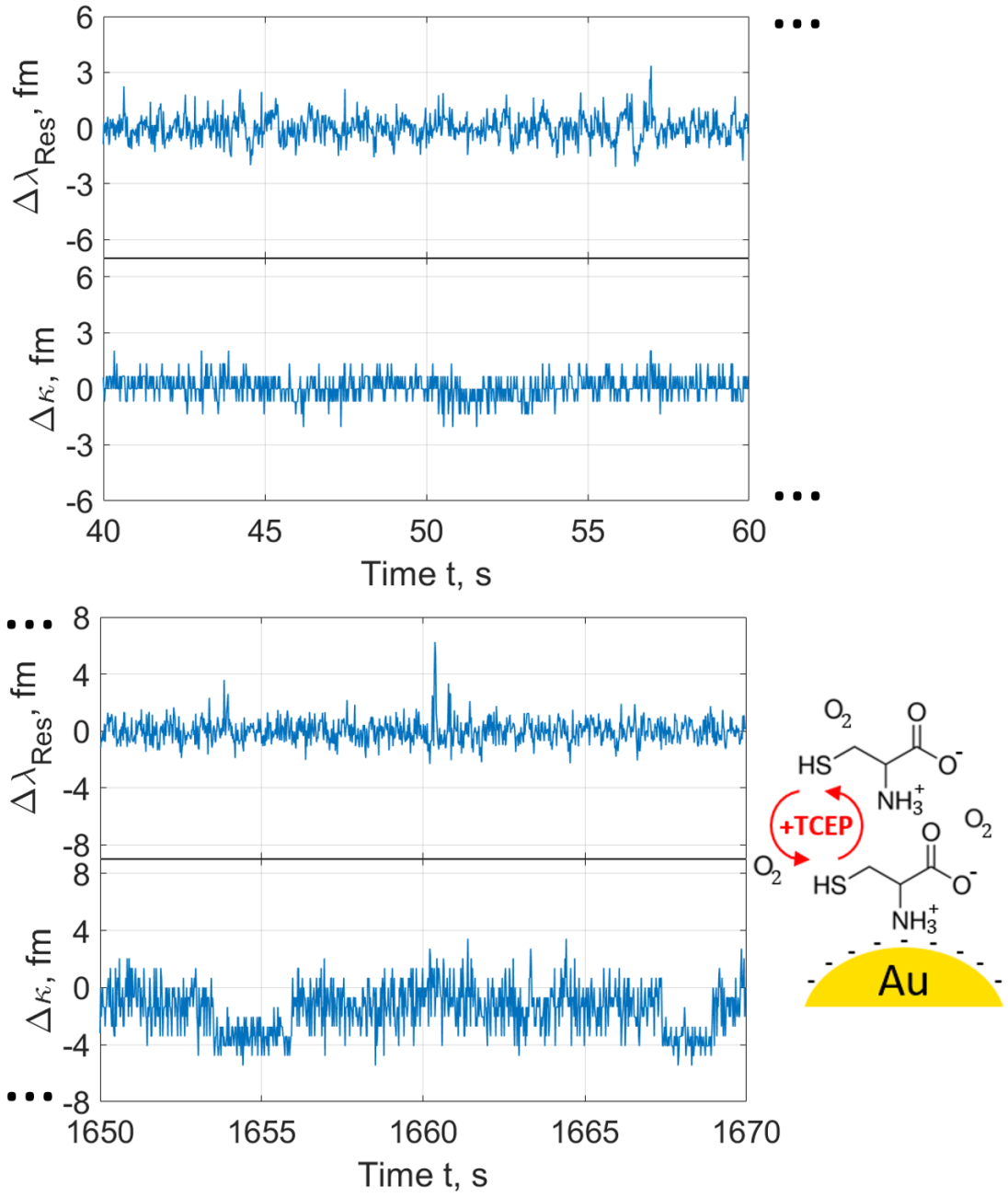

Figure 5.5: Optoplasmonic resonance response due to disulfide interactions between single DL-cysteine linkers and diffusing DL-cysteine/cystine in a 4 μM racemic mixture of equal proportions with 0.02% SDS and pH < 3. Binding sites on the gold 432 helicoid III nanoparticles are approaching saturation and TCEP reducing agent is employed.

5.3 Signal Cross-Comparison for Cysteine and Polylysine

To test the hypothesis that the hybrid LSP-WGM resonance response could characterise perturbing molecules, measurements with a sizeable number of transient events (e.g. > 1,000) were conducted. Gold 432 helicoid III nanoparticles were, again, deposited onto a glass WGM microsphere and the previous 0.02% SDS buffer conditions were mirrored.

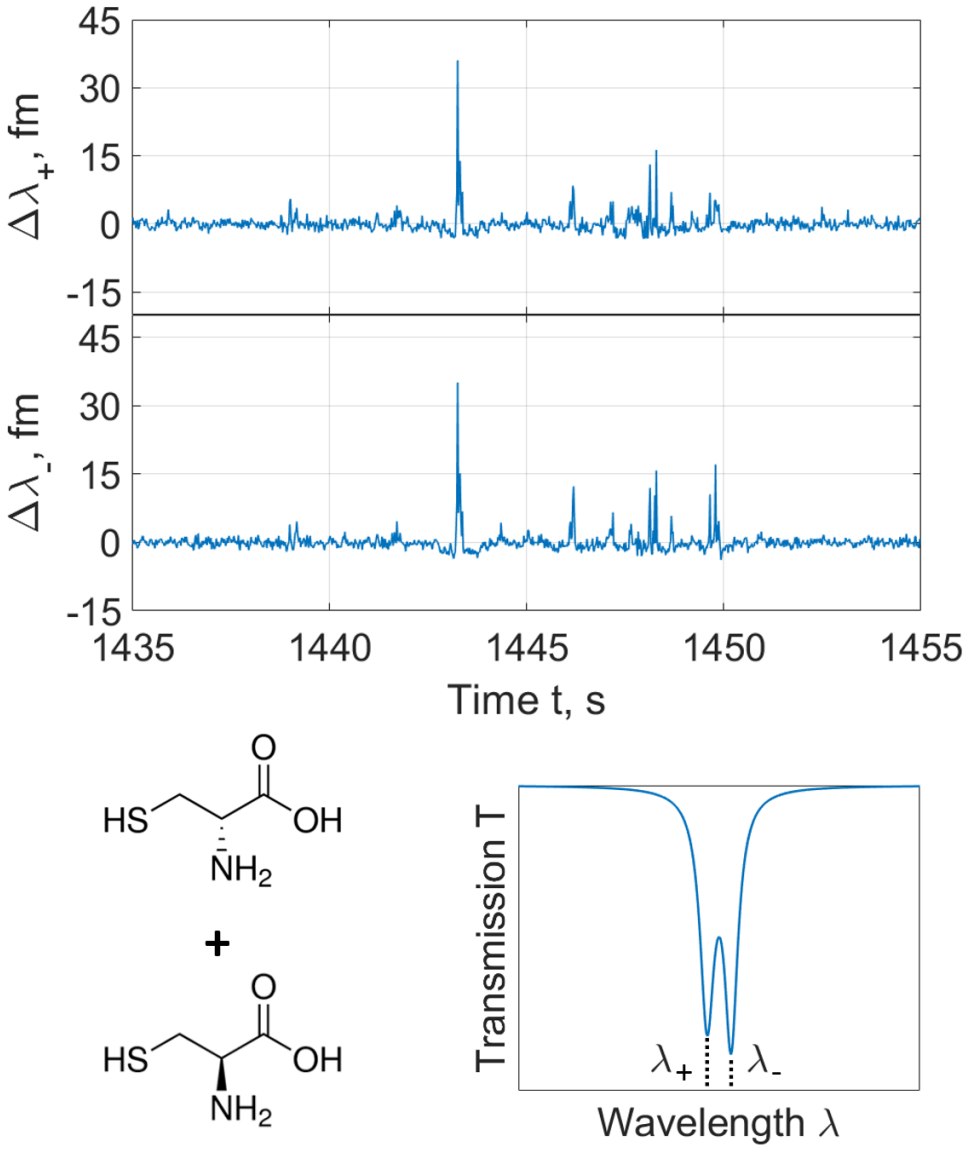

Figure 5.6: Single-molecule events on gold 432 helicoid III nanoparticles for 3 μM D-cysteine and 3 μM L-cysteine with excess TCEP in 0.02% SDS and at pH 4. The resonance is split due to scattering and so clockwise- and counterclockwise-propagating WGMs are simultaneously tracked.

Scattering from the nanoantennae established mode splitting and the surrounding solution's pH was lowered to 4 by adding diluted hydrochloric acid. Once 6 μM of DL-cysteine (i.e. 3 μM D-Cys and 3 μM L-Cys) with excess TCEP was injected into the sample volume, signal activity followed for 10's of minutes. Figure 5.6 represents a trace segment with the strongest observed resonance perturbations in the two split modes.

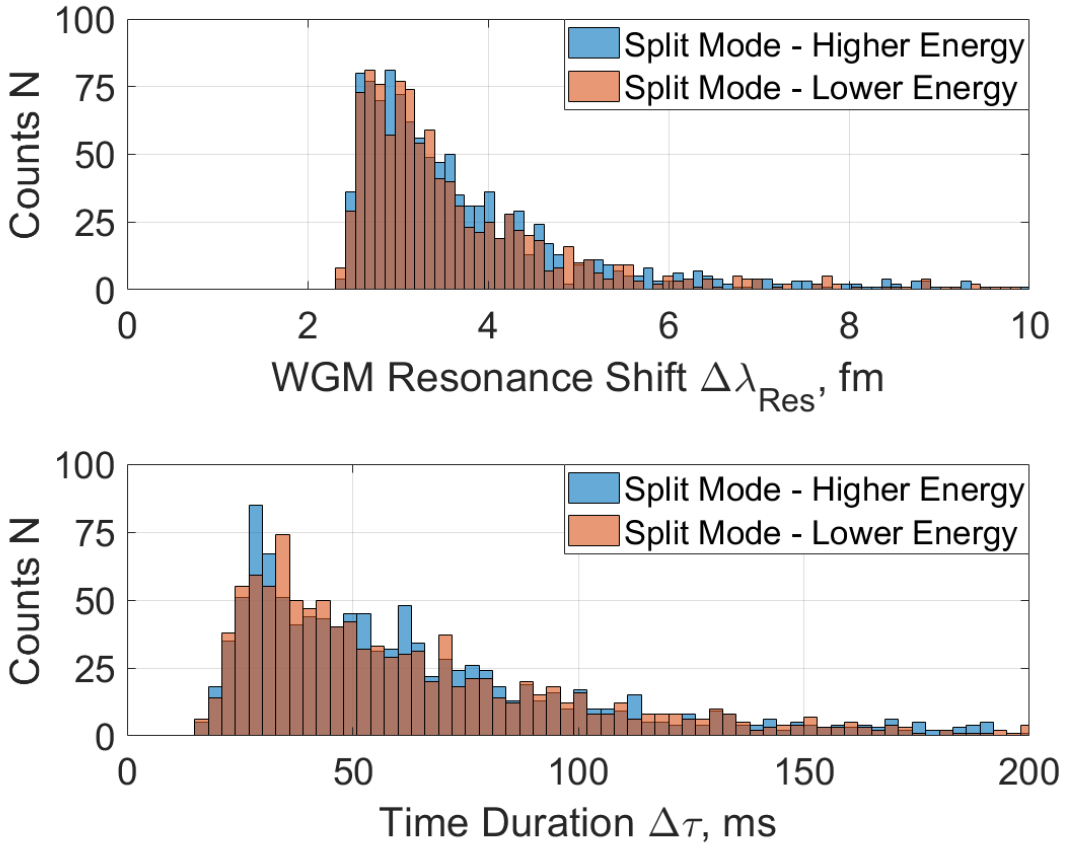

Figure 5.7: Compiled signal histograms for the resonant wavelength shift $\Delta\lambda_{Res}$ and event time duration $\Delta\tau$, with 3 μM of reduced D-Cys and 3 μM of reduced L-Cys in 0.02% SDS and at pH 4. The analysis is based on the trace of Figure 5.6.

If we amass such single-molecule events to plot histograms for the shifts, we can see in Figure 5.7 that there are some immediate parameters that we can extract. The mean $\mu_{\Delta\lambda} \approx$ 4 fm and standard deviation $\sigma_{\Delta\lambda} \approx 2$ fm for the shift value $\Delta\lambda_{Res}$ are comparable between the split modes, while λ_+ has $\mu_{\Delta\tau} = 67.8$ ms, $\sigma_{\Delta\tau} = 48.3$ ms and λ_- has $\mu_{\Delta\tau} = 65.8$ ms, $\sigma_{\Delta\tau}$ = 44.6 ms for the event time duration $\Delta\tau$. A pair of peaks may be resolvable in the $\Delta\lambda_{Res}$ histogram for λ_-; however, it is dubious to assign these to molecular chirality. The intuition here is that since the nanoparticles have a dominant handedness, i.e. from their synthesis

by L-glutathione, chiral interaction with the enantiomers should manifest itself as a split histogram with D- and L-isomer regions bifurcated by the mixed polarisability ξ. Regardless, sensing site heterogeneity on the nanoparticles is likely dominant and the field enhancement variance may alone account for this separation.

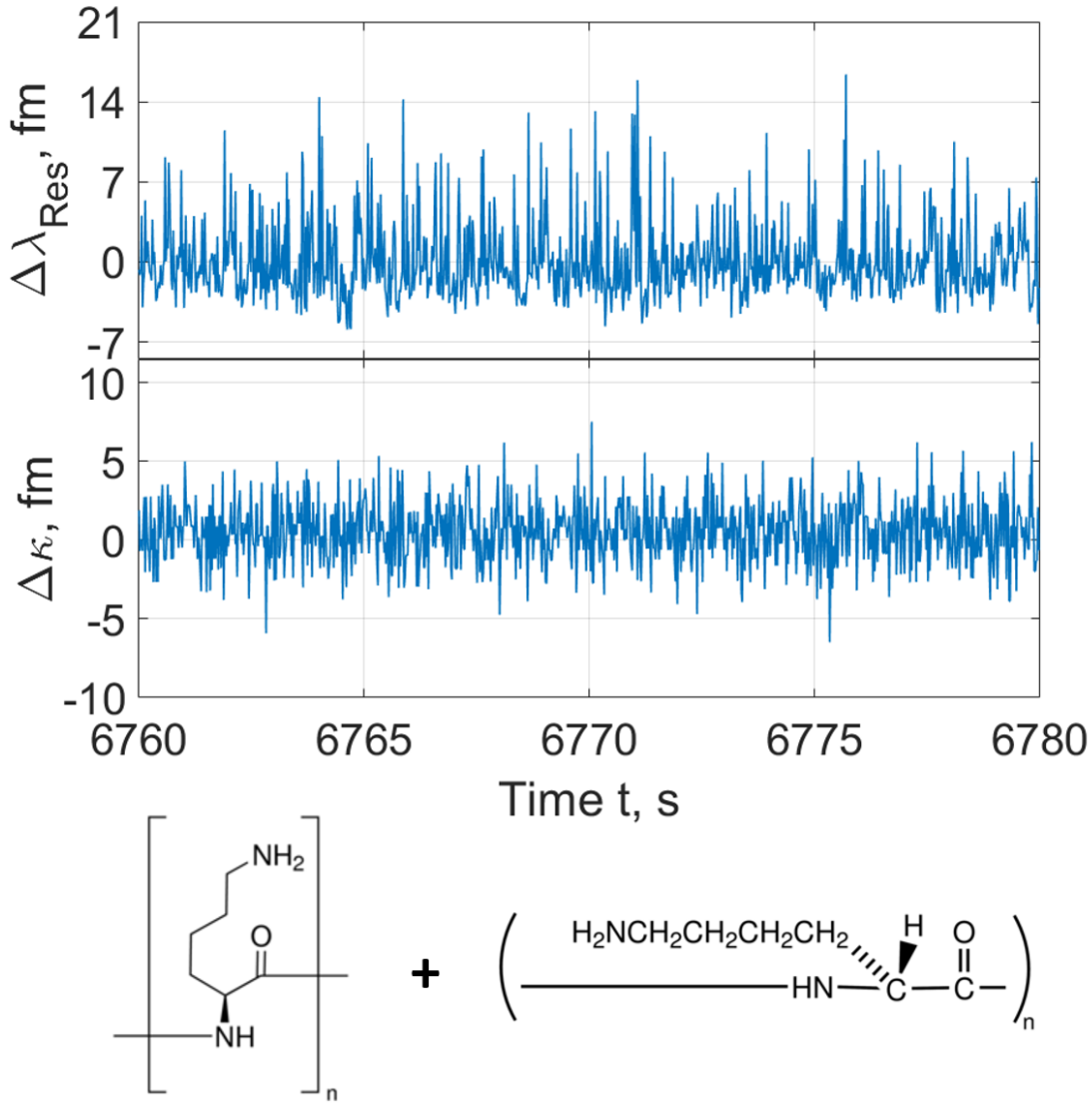

Figure 5.8: Optoplasmonic resonance response from gold 432 helicoid III nanoparticles and single polylysine perturbers (0.9 nM poly-D- and 0.9 poly-L-lysine) in 0.02 %SDS at neutral pH.

Subsequently, an analyte with greater molecular weight and wider size range was considered: poly-D- and poly-L-lysine polymers (incl. reactive primary amine groups) weighing between 30 and 70 kDa . Hinted within the signal interval of Figure 5.8 for 900 μM poly-D-

lysine and 900 μM poly-L-lysine in 0.02% SDS at neutral pH, the mean event rate is at least doubled and the mean spike amplitude increases. Coiled polylysine at this concentration has higher polarisability than cysteine and higher overlap with the near field of the chiral plasmonic nanoantennae. What we can glean from Figure 5.9's $\Delta\lambda_{Res}$ histogram is that the quantities $\mu_{\Delta\lambda}$ = 7.3 fm and $\sigma_{\Delta\lambda}$ = 2.8 fm are in a good agreement with the larger weight and weight variance of polylysine compared to a cysteine analyte. The off-rates are slightly longer as the mean is shifted to $\mu_{\Delta\tau}$ = 75.9 ms and the standard deviation $\sigma_{\Delta\tau}$ = 46.4 ms, which could potentially correlate to polylysine's lower diffusivity. It is asserted that chirality cannot be inferred from these results as the molecules are free to react on the entire surface of the chiral gold nanoparticles. To reiterate, the field enhancements for these detection sites varies significantly. Constraining the surface reactions on the nanoantennae is therefore instrumental in achieving specificity, as we will address in the next chapter.

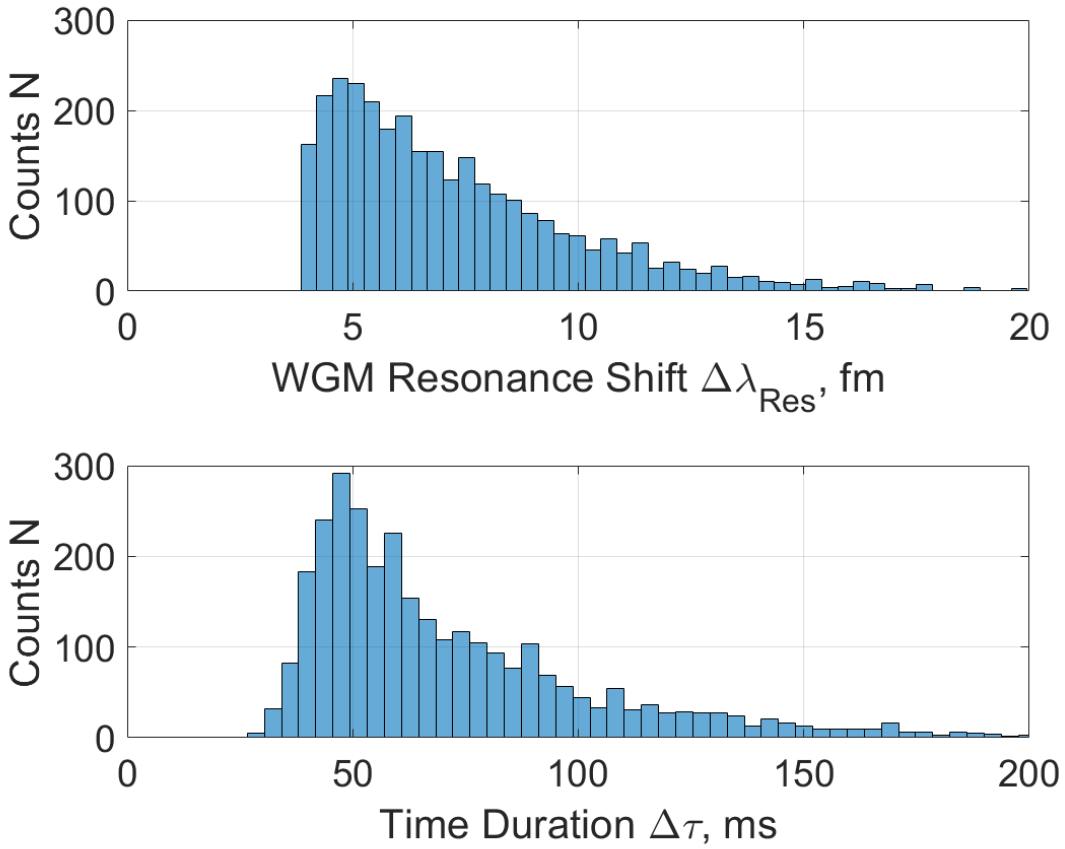

Figure 5.9: Resonance shift and time duration histograms for single-molecule signals from 0.9 nM poly-D- and 0.9 nM in 0.02% SDS and at neutral pH. The trace from Figure 5.8 is used for this data processing.

Chapter 6

Monitoring Thiol-Disulfide Exchange On the Single-Molecule Level

6.1 Publication II on Steering Reaction Pathways of Single Molecules

In Chapter 5, we challenged the notion of whether a hybrid LSP-WGM resonator could be exploited to back out the properties of single molecules, such as polarisability or chirality, when these disturb the resonance. The impact of spatial heterogeneity on the light-matter interactions at the plasmonic nanoparticle raises questions about the meaning of the signal amplitude in a resonance trace. Polylysine's larger polarisability and lower diffusion coefficient with respect to cysteine were reflected in the higher mean resonance shift and event time duration of the signal histograms. Transient interactions with gold also obey time-reversal symmetry — in other words, at steady state, the signal patterns are indistinguishable whether we go forward or backwards in time.

Such progression is not altogether different from the simultaneity of reactions ongoing at chemical equilibrium. Forward and backward reaction rates at equilibrium are counterbalanced as to, in an ensemble, conceal the exceptional pathways a detected molecule can take. A dominant reaction pathway will break this time-reversal symmetry. In practice, rare events can be missed without resorting to a mediating molecule or without shifting reactions away from equilibrium. We may claim that the ideal single-molecule signal could then be a reversible step response in the optoplasmonic resonance wavelength, linewidth, and/or mode splitting, as this clearly demarcates a state transition.

The following manuscript [25] proceeds to abate such uncertainty in surface reactions by way of disulfide bonds. Thiol/disulfide exchange takes place at single thiol sites, i.e. the reactive thiols of cysteamines that are bound to gold via their amine, in a cyclical manner. A pH above the aminothiol's pKa_{NH_2} conserves its anionic state and strongly diminishes the probability of thiol-gold reactions. Reducing agent plays a pivotal role in the cleaving of disulfide bridges formed in the bound dimer complexes as to promote monomerisation over dimerisation. Notably, the conditions that are shown for the loading of cyteamine linkers onto gold nanoantennae permits resolution of binding at concentrations down to 100's of aM — as sparse a number of biomolecules as $\sim$25,000 in the chamber volume. In conjunction with streamlining the characterisation of thiolated molecules, redox cycling with pH-enforced charge states exposes repeated perturbations of the LSP-WGM resonance that are consistent with the physics set out in Chapter 3. The next series of experiments with sub-kDa species were conceived and executed by the thesis author, while the manuscript was written with input from Sivaraman Subramanian and Frank Vollmer.

6.2 Optoplasmonic Characterisation of Reversible Disulfide Interactions at Single Thiol Sites in the Attomolar Regime

Serge Vincent, Sivaraman Subramanian, and Frank Vollmer*

**Living Systems Institute, School of Physics, University of Exeter, Exeter EX4 4QD, UK*
Email: sv316@exeter.ac.uk; f.vollmer@exeter.ac.uk

Abstract

Probing individual chemical reactions is key to mapping reaction pathways. Trace analysis of sub-kDa reactants and products is obfuscated by labels, however, as reaction kinetics are inevitably perturbed. The thiol-disulfide exchange reaction is of specific interest as it has many applications in nanotechnology and in nature. Redox cycling of single thiols and disulfides has been unresolvable due to a number of technological limitations, such as an inability to discriminate the leaving group. Here we demonstrate detection of single-molecule thiol-disulfide exchange using a label-free optoplasmonic sensor. We quantify repeated reactions between sub-kDa thiolated species in real time and at concentrations down to 100's of attomolar. A unique sensing modality is featured in our measurements, enabling the observation of single disulfide reaction kinetics and pathways on a plasmonic nanoparticle surface. Our technique paves the way towards characterising molecules in terms of their charge, oxidation state, and chirality via optoplasmonics.

Introduction

Access to single-molecule reactions to determine the state of participating species and their reaction mechanisms remains a significant technological challenge. The application of fluorescent optical methods to investigate a single molecule's reaction pathway is often non-trivial. Sophisticated fluorescent labelling may not be available, while the temporal resolution is limited by photobleaching and transit times [165, 166]. Monitoring reactions between molecules that weigh less than 1 kDa is further complicated by labels, as adducts can have severely altered reaction kinetics. Non-invasive optical techniques for studying the nanochemistry of single molecules have thus been elusive.

Thiol and disulfide exchange reactions are particularly relevant to the field of nanotechnology [167, 168]. The reversibility of the disulfide bond has, for example, paved the

way to realising molecular walkers and motors [169, 170]. Bottom-up thiol self-assembled monolayers have shown potential as building blocks for sensors and nanostructuring [171]. The precise attachment/detachment of thiolated DNA origami has even extended to the movement of plasmonic nanoparticles (NPs) along an engineered track [172]. In nature, disulfide bonds are a fulcrum for cell biochemistry. Reactions that form these links usually occur post-translation, stabilising folding and providing structure for a number of proteins [173, 174, 175]. The cell regularly controls disulfide bonds between thiol groups, alternately guiding species through reduction and oxidation [176]. Redox potentials and oxidative stress in this context are reflected in the relative concentrations of thiols and disulfides [177].

Thiol/disulfide equilibria can be quantified in bulk, although often at the expense of high kinetic reactivity and the need for fluorescent or absorptive reagents to measure the exchange [178]. One such approach is an enzymatic recycling assay with 5-thio-2-nitrobenzoic acid absorbers capable of detecting thiols and disulfides down to 100's of picomolar concentrations [179]. This trades off quenching of thiol oxidation and exchange with the optimisation of reaction rates and the disruption of the thiol/disulfide equilibrium. As a disulfide bridge consists of two sulfur atoms that can interact with a thiolate (i.e. the conjugate base of a thiol), disulfide exchange is fundamentally intricate and the reaction branches for single molecules have yet to be fully characterised in the literature. Distinguishing leaving groups through a sensing element has so far been unachievable.

State-of-the-art sensors capable of transducing single-molecule interactions into optical [76, 77, 78], mechanical [82, 83, 84], electrical [79, 80, 81], or thermal [85] signals continue to emerge. Here we employ a label-free optoplasmonic system [22] that has the specific advantage of detecting individual disulfide interactions in solution. Due to the hybridisation between an optical whispering-gallery mode (WGM) resonator and localised surface plasmon (LSP) resonance of a NP, perturbations to an LSP are observed through readout of a WGM coupled to it [180, 181, 182]. One strategy we propose is to immobilise thiolates on a gold NP surface with a separate functional group. Following selective covalent binding, immobilised thiolates may participate in redox reactions while under non-destructive probing. Reactions between sub-kDa reactants are monitored in real time and at concentrations as low as 100's of attomolar, hence isolating for the disulfide chemistry of single molecules in vitro. Such reactions frequently result in abrupt changes in hybrid LSP-WGM resonance linewidth/lifetime – a surprising phenomenon that was considered unresolvable by WGM mode broadening or splitting [54, 95, 183]. We clarify in this study that disulfide linkages to bound thiolate receptors can exclusively affect the hybrid LSP-WGM resonance linewidth, beyond a description via an unresolved mode split. Each linewidth transition per exchange also assigns a status to the leaving group. Our data suggests a sensing modality for inferring

kinetics and chains of single disulfide reactions in proximity to a plasmonic NP, paving the way towards assessing molecular charge, oxidation, and chirality states on an integrated platform.

Results

Experimental Scheme

A gold NP surface serves as an effective detection area for biomolecular characterisation on an optoplasmonic sensor. Light field localisation and nanoscale mode volumes at the NP hotspots enable sensitivity to surface modification, wherein covalent bonding to the NP restricts the total number of binding sites. Previously, thiol and amine based immobilisation has been explored on our optoplasmonic sensor [162]. Under particular pH conditions that dictate the molecular charge of the analyte, thiol and amine functional groups were reported to bind to different facets of gold NPs [184, 185, 186, 187]. For thiols, the binding preference is in the (111) and (100) planes of a gold surface which are present in an ordered crystal lattice. For amines, binding preferentially takes place at uncoordinated gold adatoms. Measurements from [162] showed an approximate 2 orders of magnitude larger number of binding sites for thiols compared to amines on gold nanorods (NRs), demonstrating variable selectivity depending on surface regularity. If molecular charge is controlled and the NR surfaces are appropriately deformed, conditions can be reached where molecules containing both amine and thiol groups can predominantly bind onto gold via amine to create recognised thiolates [188]. These nucleophiles may attack disulfide bonds in molecules that diffuse to them. Reducing agents introduced in solution, such as tris(2-carboxyethyl)phosphine (TCEP), can then reduce bound disulfides and complete a redox cycle. This pathway establishes cyclical reactions near the NP surface to be analysed statistically.

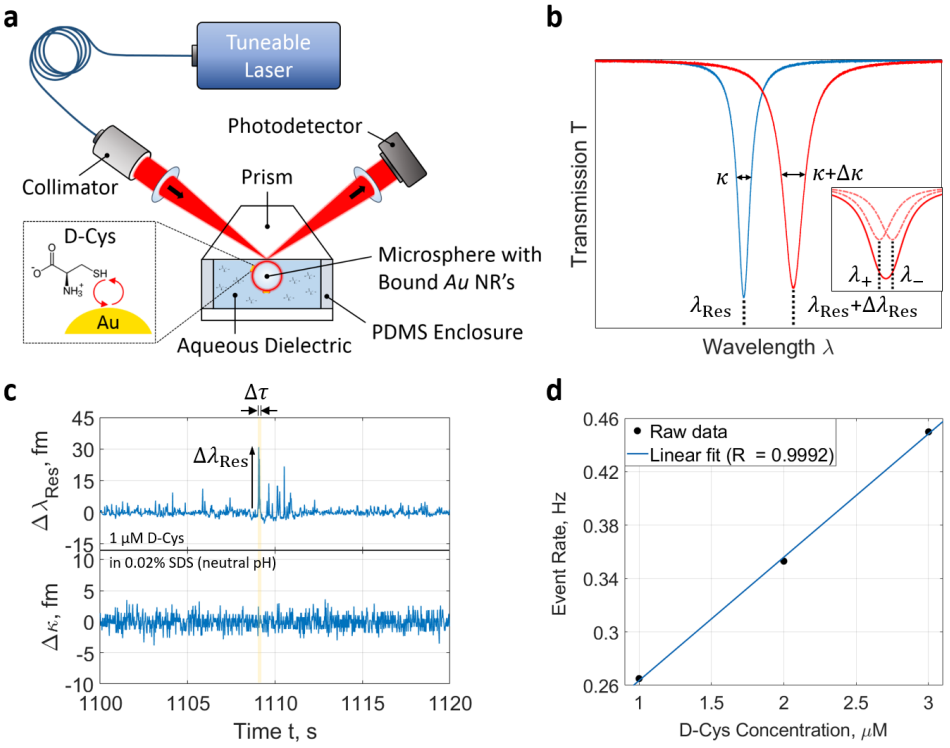

Figure 6.1: Optoplasmonic sensor setup and quantification of adsorbing D-cysteine. (a) Scheme for LSP-WGM based sensing. A beam emitted from a tuneable laser source, with central wavelength of 642 nm, is focused onto a prism face to evanescently couple to a microspherical WGM cavity. The WGM excites the LSPs of Au NRs on the cavity surface and the hybrid system's transmission spectrum is acquired at the output arm of the setup. D-cysteine (D-Cys) analytes have carboxyl, thiol, and amine groups. (b) Sensing through tracking perturbations of the Lorentzian resonance extremum in the transmission spectrum. The resonant wavelength λ_{Res} and linewidth κ that define the quality factor $Q = \lambda_{\mathrm{Res}}/\kappa$ are shown in the subfigure, as is unresolved mode splitting due to scattering. (c) Single-molecule time-domain signatures with signal value $\Delta\lambda_{\mathrm{Res}}$ and duration $\Delta\tau$ from the transit of D-Cys near Au NRs. The solvent used is 0.02% sodium dodecyl sulfate (SDS) in deionised water. (d) Linear dependence of event frequency on analyte concentration that suggests first-order rates. Events conform to a Poisson process (Figure 6.6).

The LSP resonance of a plasmonic NP can be weakly coupled to a WGM resonance of a dielectric microcavity. Through this coupling, molecules that successfully perturb the gold NP surface can be detected as shifts in a LSP-WGM resonance. Light coupled in and out of the hybrid system allows for evaluation of gold NP perturbations, i.e. by laser frequency sweeping across the LSP-WGM resonance and spectrally resolving the resonant lineshape of the transmitted light. In our setup we excite WGMs in a silica microsphere, with diameters in the range of 70-90 μm, using a tuneable external cavity laser with 642-

nm central wavelength. The laser beam is focused onto a prism surface to excite WGMs by frustrated total internal reflection. With a sweep frequency of 50 Hz, the transmission spectrum is acquired through photodetection at the output arm every 20 ms and a Lorentzian-shaped resonance is tracked (Figure 6.1a,b). The evanescent field at the periphery of the microcavity is subsequently enhanced and localised in the vicinity of bound, LSP-resonant gold NRs. The cetyltrimethylammonium bromide-coated NRs have a 10-nm diameter and 24-nm length with longitudinal LSP resonance at $\lambda_0 = 650$ nm. In the event of molecules interacting with the gold NR, the LSP-WGM lineshape position λ_{Res} and/or full width at half maximum κ will vary. Discrete jumps in these parameters may be measured in the time domain and are indicative of molecular bond formation with gold. Groupings of signal fluctuations exceeding 3σ from transient arrival/departure can also arise (Figure 6.1c), where σ is the standard deviation of the noise derived from a representative 20-s trace segment. The resonance shifts of these signal packets are compiled for a series of analyte concentrations to confirm Poissonian statistics and first-order reaction rates (Figure 6.1d). An extrapolation error exists in Figure 6.1d given the chosen concentration range yet the event rate is most closely linear with concentration. Despite the negligible scattering and absorption cross section of a single molecule, the ultrahigh-quality-factor WGM and its back-action on the perturbed LSP acts as a channel to sense loss changes intrinsic to or induced by a gold NP antenna. NP absorption spectroscopy by means of optoplasmonics [96] provides groundwork for such a modality, as the absorption cross section change in a NP due to surface reactions may become detectable. We affirm that signal traces can exhibit 1) simultaneous shifts in resonant wavelength, linewidth, and resolved mode splitting [54, 183] and 2) exclusive linewidth variation when single molecules diffuse within the LSP evanescent field decay length of the NP. Note here that the spectral resolution of our system is set by the laser frequency noise.

Disulfide Reaction Mechanism and Statistical Analysis

Loading of the gold NR surface with thiolate linkers requires a set of restrictions on the solvent environment at room temperature. To promote amine-gold bonds, we use a buffer at a pH that is above an aminothiol's logarithmic acid dissociation constants $\mathrm{pKa_{SH}}$ and $\mathrm{pKa_{NH_2}}$. Within this balance, anionic species with negatively charged S^- and neutral NH_2 groups will dominate as per the Henderson-Hasselbalch equation [189]. A molecule must first reach the gold surface by overcoming Debye screening from surface charges [93], e.g. from the gold NR's coating and pre-functionalisation of the glass microcavity. Such electrostatic repulsive forces can be reduced by electrolyte ions in substantial excess of the molecules under study. Analogous to raising the melting temperature of DNA from ambient conditions by increasing

the salt concentration, the arrival rate of molecules to detection sites plateaus when the salt concentration is on the order of 1 M. Due to indiscriminate attachment of gold NRs onto the glass microcavity in steps preceding single-molecule measurements (Figure 6.7a), molecules in the medium should also be replenished to account for capture by NRs outside of the WGM's evanescent field (i.e. those that do not contribute to LSP-WGM hybridisation). Overall, these factors necessitate high electrolyte concentrations and recurring injection of analyte into a buffer of pH > pKa_{NH_2} to attain a sufficient reaction rate in the subfemtomolar regime.

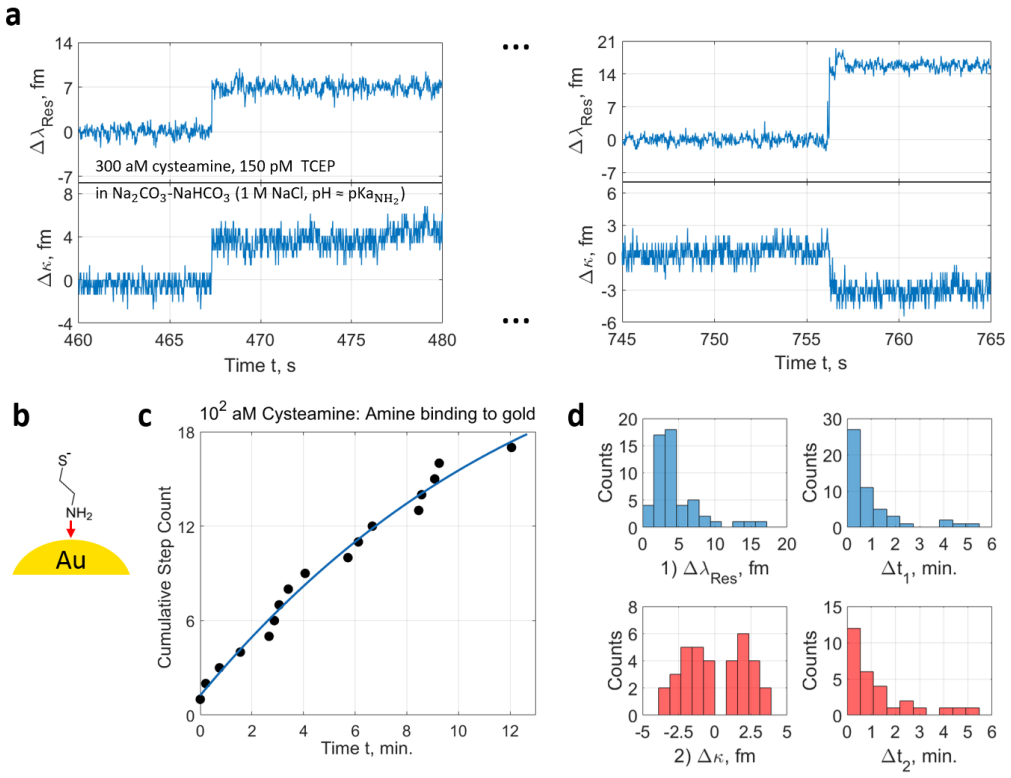

Figure 6.2: Single cysteamine binding to gold NRs via amine at subfemtomolar concentration. (a) Discrete signals in the LSP-WGM resonance trace from covalent bonding of the NH_2 ligands to *Au* in a basic buffer. (b) Conceptual diagram of the cysteamine surface reaction. Cysteamine, with its thiol and amine groups, forms an amine-gold bond as indicated by the red arrow. (c) Exponential decay in cumulative binding step count as the system approaches saturation. In this regime, it is necessary to periodically inject more analyte in solution as scarce analytes are lost to external immobilisation (i.e. from undetected NRs that are not excited by the WGM). (d) Histograms depicting the resonance shift $\Delta\lambda_{\text{Res}}$ and linewidth shift $\Delta\kappa$ for binding events, as well as their related event time separations Δt_1 and Δt_2. The $\Delta\kappa$ distribution shows both positive and negative shifts, while Δt_1 and Δt_2 distributions are Poissonian.

The aminothiol linkers of interest for our experiments are chemically simple amino acids or pharmaceuticals with minimal side chains. For chiral studies, D- and L-cysteine (pKa_{SH} = 8.33 and pKa_{NH_2} = 10.78 [190]) are good candidates as they contain a carboxyl group that does not interfere with disulfide reactions. Nevertheless, for simplicity, we began with cysteamine (pKa_{SH} = 8.19 and pKa_{NH_2} = 10.75 [191]) as it is a stable aminothiol that excludes any side chains. The cysteamine's amine group favourably binds to our optoplasmonic sensor in a sodium carbonate-bicarbonate buffer at a pH slightly above 10.75, with 1 M sodium chloride (Figure 6.2a,b). Typical signal patterns in Figure 6.2a for amine-gold binding are discontinuous steps in both λ_{Res} and κ on the order of 1 to 10 fm, with monotonic redshifts in λ_{Res}. Signal magnitude and direction depends on variables such as the position and orientation of the gold NR detector on the microcavity [22], the detection site on the NR itself, and the analyte's molecular mass/polarisability [86]. As time evolves and analyte is steadily supplied, the binding sites become occupied and event rate decreases (Figure 6.2c). These independent shifts in λ_{Res} and κ are collected in Figure 6.2d to showcase non-monotonic linewidth narrowing and broadening once single molecules bind. This is an unconventional result as there are equally likely signs for $\Delta\kappa$ without apparent proportionality to $\Delta\lambda_{Res}$. A singlet of an unresolved mode split that would generate the linewidth shift is thus unsubstantiated.

An added convenience of choosing cysteamine is its comparable diffusion kinetics with respect to N-acetylcysteine (NAC) – a synthetic precursor of cysteine with acetyl protecting group in place of primary amine. We used NAC as a negative control and the response revealed a negligible rate of thiol-gold bond formation at high pH and high concentration (Figure 6.3). A lack of step discontinuities within the trace supports amine-gold bonding in the basic buffer and therefore thiol-functionalisation of the gold NRs with cysteamine.

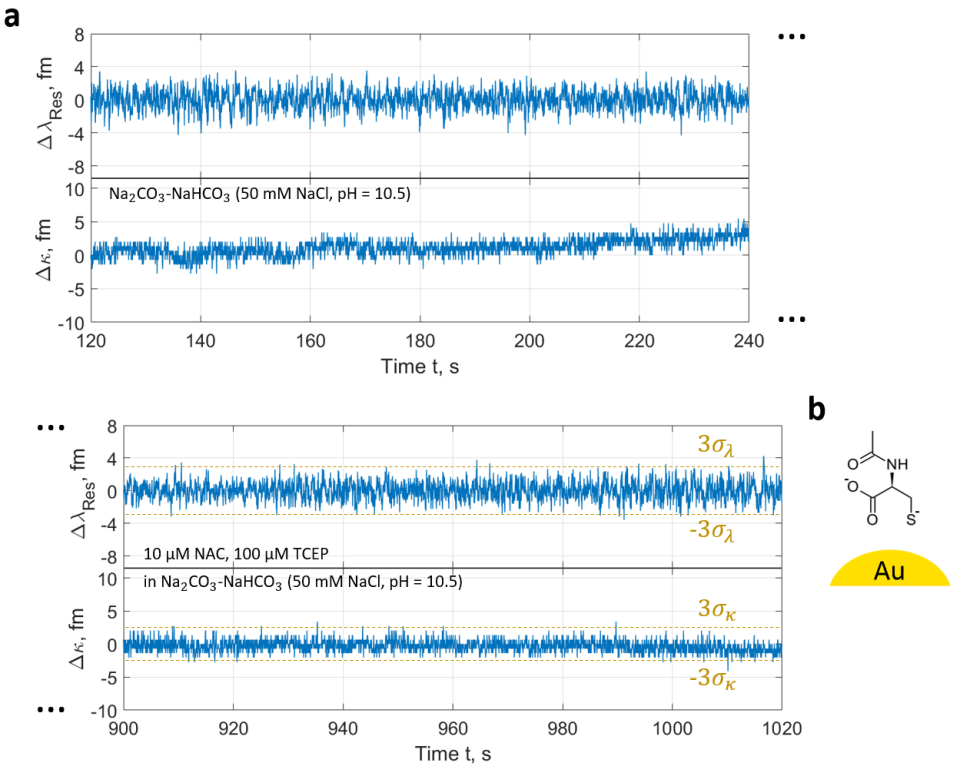

Figure 6.3: Background and negative control measurement with NAC at micromolar concentration. (a) Resonance and linewidth shift traces exhibiting transient signal above 3σ with rates on the order of 0.1 s^{-1} over several minutes; however, these persist in the presence and absence of NAC and TCEP in solution. No permanent binding patterns were found during peak tracking. (b) NAC molecule, with carboxyl, thiol, and (amine-attached) acetyl groups, near a detection site.

pH-Dependent Disulfide Nanochemistry

The charge of single molecules diffusing to the optoplasmonic sensor can lead to a diverse set of reactions and LSP-WGM resonance perturbations. Dimerisation, for instance, is maximised when thiol groups are made nucleophilic through deprotonation at a pH above the pKa_{SH}. To circumvent electrostatic repulsion between primary amines, high aminothiol dimerisation and disulfide exchange rates demand a pH greater than the pKa_{NH_2}. We therefore investigated these effects by way of pH variation near the pKa_{NH_2}. After pre-loading the gold NRs on the glass WGM microcavity with cysteamine in Figure 6.4a, we flushed the chamber volume and replaced the surrounding dielectric with sodium carbonate-bicarbonate buffer, 1 M sodium chloride, at pH 10.19 < pKa_{NH_2}. Figure 6.4b highlights signal activity upon addition of a racemic, subfemtomolar mixture of reduced D- and L-cysteine. Transient peaks

in the linewidth appear in packets that dissipate (see Figure 6.4c) as external capture removes available DL-cysteine. We attribute these peaks to thiolates that fail to form a disulfide bond (Figure 6.4d). The Poisson-distributed events for $t \leq 2$ min. have a mean rate = 0.01 $\text{aM}^{-1}\text{s}^{-1}$ that surpasses diffusion (i.e. $D_{\text{DL-Cys}} \sim 10^{-10}$ m^2s^{-1}, $k_{\text{on}} \sim 1$ $\text{nM}^{-1}\text{s}^{-1}$ [192]), implying molecular trapping near the gold NR hotspots. Charged molecules are, by analogy to atomic ions [93], bounded by an electrostatic potential well whose depth is increased in proportion to ionic strength.

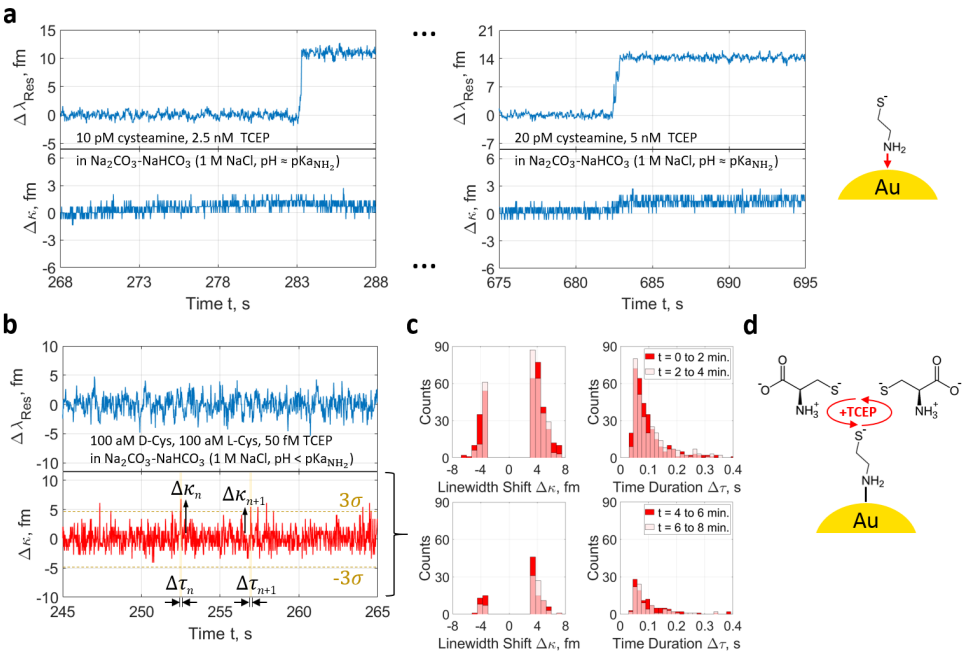

Figure 6.4: Cysteamine pre-functionalisation and disulfide events from converging DL-cysteine. (a) Binding of cysteamine to *Au* NRs via amine in basic buffer. (b) Linewidth fluctuations induced by racemic DL-cysteine interacting with immobilised cysteamine thiolates at $\text{pKa}_{\text{SH}} < \text{pH} < \text{pKa}_{\text{NH}_2}$. TCEP reducing agent is employed here to counteract cysteine oxidation/dimerisation. (c) Linewidth shift $\Delta\kappa$ and event time duration $\Delta\tau$ histograms extracted from the resonance trace of (b). The mean event rate of the Poisson distributions passed through an inflection point, decreasing from 0.01 $\text{aM}^{-1}\text{s}^{-1}$ to 0.003 $\text{aM}^{-1}\text{s}^{-1}$ within an 8-minute interval as the diffusing cysteines were captured. (d) DL-cysteine and bound cysteamine transiently interacting via their thiol groups.

For proof of principle, we increased the environmental pH to 11.09 and raised the analyte concentration. In this regime we expected sustained reversible disulfide reactions with defined signal states in the resonance trace. The neutral amines of the highly anionic cysteamine and L-cysteine indeed result in binding/unbinding state transitions as in Figure 6.5a, with clear linewidth broadening and narrowing steps of roughly equal mean height. The stability of the

disulfide reactions is attributed to an order of magnitude rise in hydroxide ion concentration past the pKa_{NH_2} and the event rate is maintained by electrostatic trapping. Since TCEP continually cleaves bound dimers during redox cycling, the monomer or dimer state of the leaving group can also be identified (cf. Figure 6.9). This trial was repeated in Figure 6.5b for a larger molecule, 5,5'-dithiobis-(2-nitrobenzoic acid) (DTNB/Ellman's reagent), which readily underwent disulfide exchange with bound cysteamine linkers. In all cases, reducing agent concentration was adjusted until switching signals in the linewidth were observed. Resolvable dwell times and hence steady diffusion of reducing agent to the detection site were found at high molar excess > 1000.

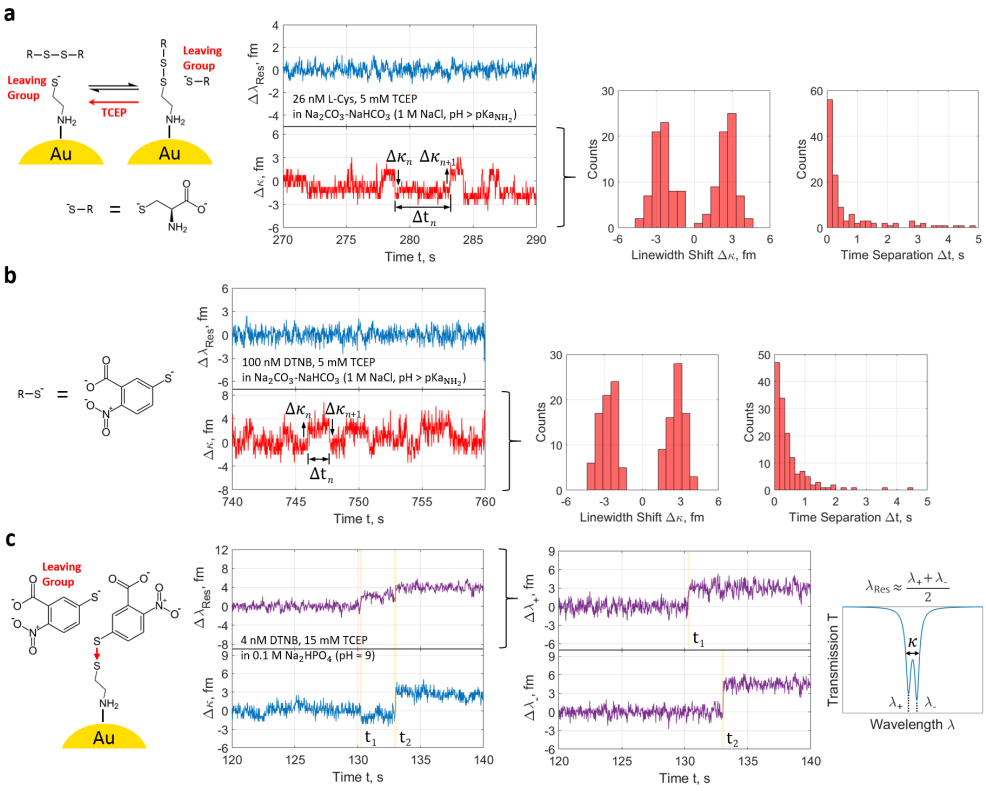

Figure 6.5: Cyclical binding/unbinding and exchange interactions with single mixed disulfides. (a) Real-time linewidth step oscillations in the LSP-WGM resonance trace from redox reactions involving individual cysteamine-L-cysteine disulfides at pH > pKa_{NH_2}. These bridges are formed between cysteamine linkers and L-cysteine thiolates/disulfides (with neutral amines), then promptly cleaved by excess TCEP. (b) Linewidth patterns similar to (a) from individual cysteamine-TNB disulfides. Thiol-disulfide exchange may be triggered by DTNB dimers alone; however, cycling is ensured through reduction with TCEP. TNB has a benzene ring with carboxyl, thiol, and nitro groups. (c) Apparent resonant wavelength and linewidth signal steps, from thiol-disulfide exchange with DTNB and bound cysteamine, in a resolvable LSP-WGM doublet/split mode.

Some insight into oscillation patterns is provided by the mode split traces of Figure 6.5c, the lineshapes for which are discernible when the coupling/scattering rate is larger than the cavity decay rate. The WGM eigenmode degeneracy is lifted here and the resonant wavelength traces for the high-energy and low-energy modes, respectively denoted as λ_+ and λ_-, disclose two separate binding events in time. Such divergence comes from perturbations of two distinct gold NRs lying at different spatial locations along the standing wave formed by counterpropagating WGMs. One nanoparticle is excited near a node of a constituent mode and the second lies near in an antinode, and then the situation inverts for the other constituent mode. Information in the split mode resonance wavelengths is encoded in the linewidth trace during single peak tracking; a shortcoming that, if corrected by available splitting, offers more robust molecular analysis by correlation to split mode properties and further detection site discrimination. Anomalous linewidth signatures of Figure 6.5a,b that exclude resonance wavelength shifting are, however, only superficially explained via mode splitting. In order for the resonant wavelength to stay constant and relative mode splitting to be a contributing factor, either $\Delta\lambda_+ = -\Delta\lambda_-$ or the transmission dip depth must oscillate – two features that we haven't detected in our recorded split mode traces. For the former to hold true, any heterodyne beat note tied to frequency splitting would have to stably oscillate between two beat frequencies. It is instead conceivable that the combination of LSP-WGM resonance energy invariance and lifetime variance implicates a relationship between the localised surface plasmon resonance and molecular vibrational modes [98]. A transition between bound vibrational states that are close in energy and reside in two continuums is possible. With shifts in the electronic resonance-dependent Raman cross-section upon chemical reaction and/or charge transfer, the Raman tensor and hence the optomechanical coupling rate may be decipherable. In this way the charge state of bound cysteamine linkers and their disulfide linkages can influence the optoplasmonic sensor response to grant molecular charge sensitivity [193].

Discussion

Experimental results were presented for single aminothiols binding to gold nanoantennae of an optoplasmonic sensor system at subfemtomolar concentrations. We leveraged these aminothiol linkers (i.e. cysteamine) by way of reaction of their amine groups with gold, followed by repeatable disulfide interactions between the linkers and diffusing thiolates/disulfides incorporating TCEP reducing agent as a counterbalancing reagent. The thiol-functionalisation of gold was reinforced by negative controls performed with thiolated molecules in an equivalent sensor configuration. Statistical analysis of signal patterns at 100's of attomolar concentration revealed finite single-molecule detection due to removal from external adsorption, ligands, or other forms of capture. This recent advance is in part

guided by selection of low-complexity analytes and saturation of environmental conditions to suppress Debye screening. Signatures in the linewidth traces were championed throughout our measurements as they were shown to contain leaving group information imprinted onto LSP-WGM resonance perturbations.

Despite the existence of identifiable disulfide interactions from DTNB, D-cysteine, and L-cysteine, a comprehensive theory to describe the underlying optoplasmonic detection mechanism has yet to emerge. Nonetheless, the dwell times and statistical inferences of cyclical single-molecule interactions in this work remain critical in circumventing site heterogeneity and characterising surface-bound thiolates and disulfides. Reactions near the nanoantennea hotspots have demonstrably lower degrees of freedom via spatial constraints and redox cycling. We foresee future refinements to the temporal resolution by locking the laser frequency to the WGM resonance. Our disulfide quantification paradigm ultimately opens avenues for charge transfer observation, including direct implementation of all sensing channels towards pinpointing single molecules and unravelling their nanochemistry.

Methods

Sample and microsphere preparation

Chemicals were purchased from *Sigma-Aldrich* and *Thermo Scientific*. The principal solvent in which analytes were dissolved was ultrapure water delivered from a *Merck* Q-POD dispenser. Solutions without NRs were passed through a 0.2 μm *Minisart* syringe filter and dilutions were performed with *Gilson* P2L, P20L, and P1000L pipettes. Each microspherical cavity was reflowed from a *Corning* SMF-28 Ultra, single-mode telecommunications fibre by CO_2 laser light absorption. Surface tension during heating yielded a circularly symmetric cavity structure with a smooth dielectric interface. Mechanical stabilisation of the suspended microcavity was provided by prior insertion into a *Thorlabs* CF126-10 ceramic ferrule, which was then secured to an aluminium holder fixed to a three-axis translation stage. The diffusion-limited sample volume of 300-500 μL was enclosed by a glass window, N-SF 11 prism face, and sandwiched polydimethylsiloxane (PDMS) basin.

Surface chemistry protocol

Once the cavity was submerged in aqueous solution and a coupling geometry was found via alignment, cetyltrimethylammonium bromide-coated gold NRs (diameter = 10 nm, length = 24 nm, and LSPR wavelength = 650 nm) from *Nanopartz* were deposited onto the microcavity surface. A desirable linewidth change $\Delta\kappa$ accumulated during deposition was roughly 40-60 fm. Microsphere surface functionalisation and passivation are further detailed in the Supplementary Methods 2. All aminothiol linkers were bound to the gold NRs in sodium carbonate-bicarbonate buffer at a pH above 10.75 with 1 M of sodium chloride ions. Additionally, washing steps were interspersed throughout each experiment to expel extraneous adsorbents.

Resonance Tracking

In experiment, the whispering-gallery mode resonance extremum of our sensor is monitored using a bespoke centroid method [93, 101]:

$$\text{First Moment} = \frac{\sum_{i=1}^{n} i\,[T_{\text{Threshold}} - T(i)]}{\sum_{i=1}^{n} [T_{\text{Threshold}} - T(i)]} \tag{6.1}$$

where $T_{\text{Threshold}}$ is the fixed transmission threshold and n is the number of points defined to be in the resonant mode. The external cavity laser is swept linearly across an $\sim$8.5 pm wavelength range as driven by a triangular scan waveform, wherein hysteresis is averted by selective recording of the upscan. The transmission spectra are acquired with a sampling rate of 2.5 MHz and bit depth of 14. Given that laser diode emission intensity differs over the wavelength scan, 200 spectra are first averaged prior to coupling. Flattening of the spectrum is then executed and a fixed transmission threshold for peak detection is set. A resonance dip is only recognised if it falls below the transmission threshold and its width exceeds a successive point minimum. If these conditions are satisfied, the time trace of the computed lineshape position and width can be visualised in real-time and stored for post-analysis. Many noise sources in the frequency domain are also put into account during our measurements, e.g. temperature drift (i.e. thermorefractivity and thermoelasticity), mechanical vibrations, laser mode hopping, and nanorod displacement.

Data Availability

Data supporting the findings of this study are available within the article and the associated Supplementary Information. Any other data are available from the corresponding authors upon reasonable request.

Code Availability

The code used in this study is available from the corresponding authors upon reasonable request.

Acknowledgments

The authors acknowledge funding from the University of Exeter, the Engineering and Physical Sciences Research Council (Ref. EP/R031428/1), and from the European Research Council under an H2020-FET open grant (ULTRACHIRAL, ID: 737071). Spectral data was acquired and step signals were evaluated using LabVIEW software developed by M.D. Baaske.

Author Contributions

S.V. designed and performed the experiments, completed the data analysis, and composed the manuscript. S.S. wrote the MATLAB application for transient signal analysis, while F.V. supervised the project and revised the manuscript. All authors discussed and interpreted the results.

Competing Interests

The authors declare no competing interests.

Corresponding Authors

Correspondence to Serge Vincent and Frank Vollmer.

Supplementary Information

Supplementary Methods 1: Single-Molecule Data Analysis

Empirical determination of spike and step signal properties is in compliance with selection criteria. Reference measurements are conducted before each step of an experiment to calculate noise floor figures, such as the background's standard deviation σ. Following the detrending of the resonance trace via a Savitzky-Golay filter, the shift value, time stamp, and time duration of transient signals (in either the resonant wavelength or linewidth) are extracted if fluctuations are smaller than -3σ or larger than 3σ. Spike packets are grouped when their time stamps lie within a specified time interval, e.g. neighbouring fluctuations less than 50 ms apart. The time scale for single-molecule interactions with the plasmonic nanoantennea is often shorter than our system's time resolution – a disparity that is crucial when identifying patterns. Steps in the resonance trace present themselves as discontinuous jumps that correlate to the sub-ms transport of analytes to the hybrid resonator, or simply molecular activity once an analyte is bound inside a plasmonic hotspot. The temporal axis thus provides a basis for comparison between signal states when discerning different interaction events that perturb the optoplasmonic sensor.

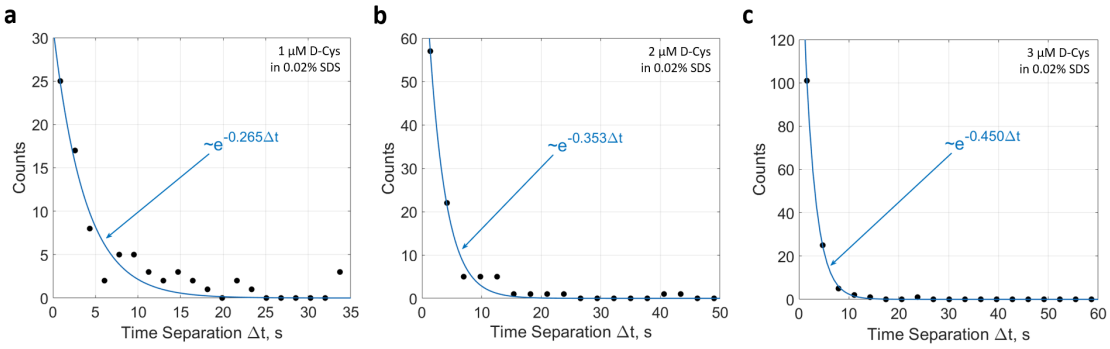

Figure 6.6: Single D-cysteine statistics. Event time separations at (a) 1 μM, (b) 2 μM, and (c) 3 μM are Poisson-distributed and the mean event rates are those used for Figure 6.1d

Statistical assessment of the trace data is carried out by histogram plotting. If 1) each instance of an event is stochastically independent to every other occurrence of that event and 2) the rate scales linearly with reactant concentration, we deem the interaction associated with single molecules. Under this assertion the Poissonion probability distribution for k events to transpire in a time interval Δt should have the form:

$$P(k,R,\Delta t) = \frac{(R\Delta t)^k}{k!} e^{-R\Delta t} \tag{6.2}$$

where R is the mean event rate. Figure 6.6 above displays this behaviour for ramping concentration and the implied convergence to a Poisson distribution as events accumulate. Signal extent and duration similarly fall within probability distributions to be approximated by bin discretisation. For all analyses of resonance parameters, we apply the Freedman-Diaconis rule to calculate histogram bin widths.

Supplementary Methods 2: Microcavity Surface Preparation

Earlier functionalisation techniques [22] for the optoplasmonic resonator incorporated electrostatic adsorption of gold nanorods (NRs) to a fused silica surface. This was a standard even for observing kinetics of enzymes on immobilised DNA [163]. At a basic pH above 7, however, the NRs' cetyltrimethylammonium bromide coating destabilises [194] as to cause further noise and eventual desorption of the NRs. Going forward, we sought suitable alternatives to electrostatic adsorption which were proven resistant to environmental pH. One option was to bind the plasmonic NRs to the amine groups of an amine-functionalised silica. This wet-chemical procedure is initiated immediately after CO_2 laser reflow of the microsphere by full immersion into a 1% (v/v) solution of 97% N-[3-(Trimethoxysilyl)propyl]ethylenediamine (in ultrapure water) for 45 s.

After aminosilanising the silica microcavity, the gold NRs are immobilised and detected as in Figure 6.7a. Depending on the exact shape of these NRs, resonance shifts may be positive, negative, or zero depending on where the localised surface plasmon resonance lies with respect to the excitation wavelength. The absorption/scattering losses experienced by the whispering-gallery mode from bound gold NRs is substantial, hence broadening in the linewidth on the order of 1-10 fm is common as long as the nanoparticles are close to the equator and overlap with the evanescent field. Finally, primary amines of the partial aminosilane coating are modified with methyl-terminated, N-hydroxysuccinimide (NHS) ester-activated polyethylene glycol (PEG) to neutralise surface charges and passivate the microcavity surface. Bulk binding is measured in Figure 6.7b, as is single methyl-NHS-PEG binding around the gold NRs in Figure 6.7c as these events far outnumber the available plasmonic sensing sites. Two classes of signal appear here: 1) frequent redshifts in the resonant wavelength and 2) redshifts accompanied by linewidth narrowing or broadening.

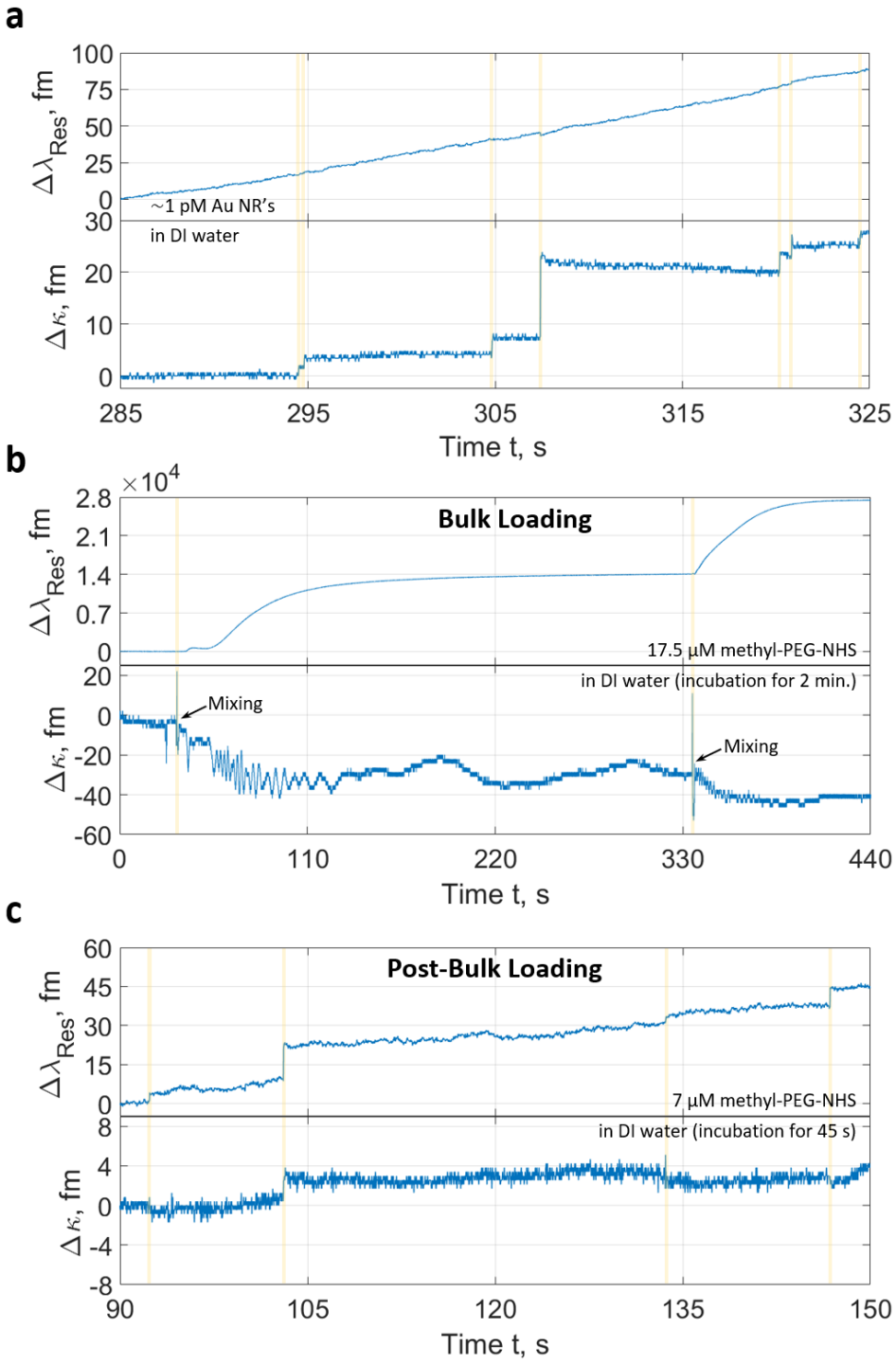

Figure 6.7: Surface functionalisation of the glass microsphere. (a) Gold NR deposition onto the microcavity via binding to the amine terminals of an aminosilane multilayer. (b) Bulk capping of surplus amines of the aminosilane multilayer with methyl-PEG-NHS ester compounds. Saturation occurs in accordance with the reactive sensing principle [86]. (c) Single methyl-NHS-PEG binding steps in proximity to plasmonic detection sites. Traces are shown in their raw form and so environmental noise, such as thermal drift, is visible.

Supplementary Notes 1: Additional Aminothiol Control

The functional groups of cysteine have been modelled in the past with density functional theory as to gauge how these interact with gold atom clusters [188]. Amine-gold anchoring was concluded therein to be energetically favourable for complex stabilisation and that lone pair electrons are transferred to the antibonding orbitals of gold. Peptide/amide bonds can be formed between carboxyl and amine groups through dehydration synthesis and carboxyl group interactions with gold clusters have been found to be non-negligible for some molecular charge states [195]. To eliminate this ambiguity and illustrate the importance of implementing reducing agents, we studied dimer formation/cleavage solely with cysteamine in a basic buffer.

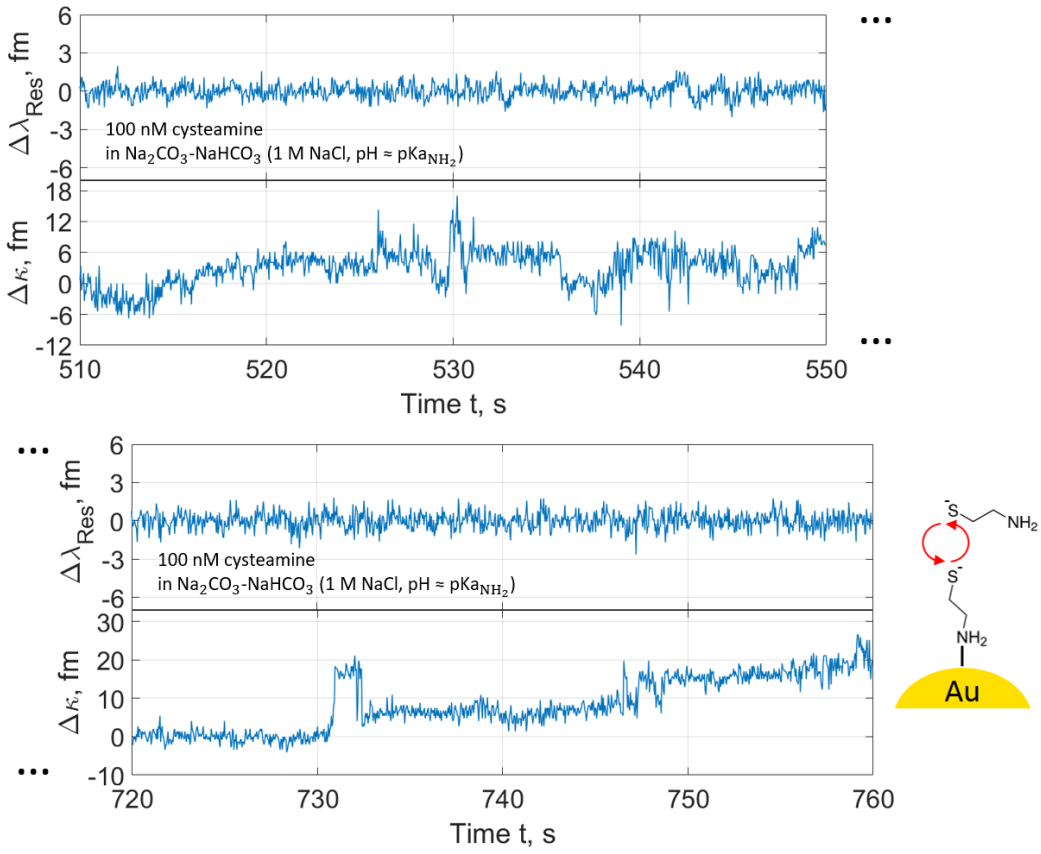

Figure 6.8: Sample trace for cysteamine disulfide reactions. Signal levels in κ vary widely in the absence of tris(2-carboxyethyl)phosphine. The vulnerability of one of the two sulfur atoms in a disulfide bond to a nucleophilic thiolate attack, whether the dimer is immobilised onto gold or not, provides reaction bi-directionality and stochastic population of the detection sites with bound dimers. The optoplasmonic linewidth thus walks off during the trace segment.

Figure 6.8 depicts short bursts of linewidth oscillations for 100 nM cysteamine akin to the pulse train of Figure 6.5a,b. These sporadic disulfide binding/unbinding events are reproducible at high analyte concentration without tris(2-carboxyethyl)phosphine, albeit step transitions are unpredictable with increased dwell time variance. Negatively charged thiolates in solution, like dithiothreitol, act as reducing agents by thiol-disulfide exchange with the outermost aminothiol of a bound disulfide. This reaction pathway could leave bound thiolate linkers and close a redox cycle, translating to pulse outliers in the resonant linewidth channel (i.e. an amalgamation of the events expounded in Figure 6.9). Spike activity is also interspersed throughout the trace in agreement with the pH value being close to the pKa_{NH_2}, as a proportion of the cysteamines' amines are protonated as in Figure 6.4b. The resonant wavelength does not drastically change in this control and therefore we interpret that cysteamine, in this case, seldom interacts with the gold directly.

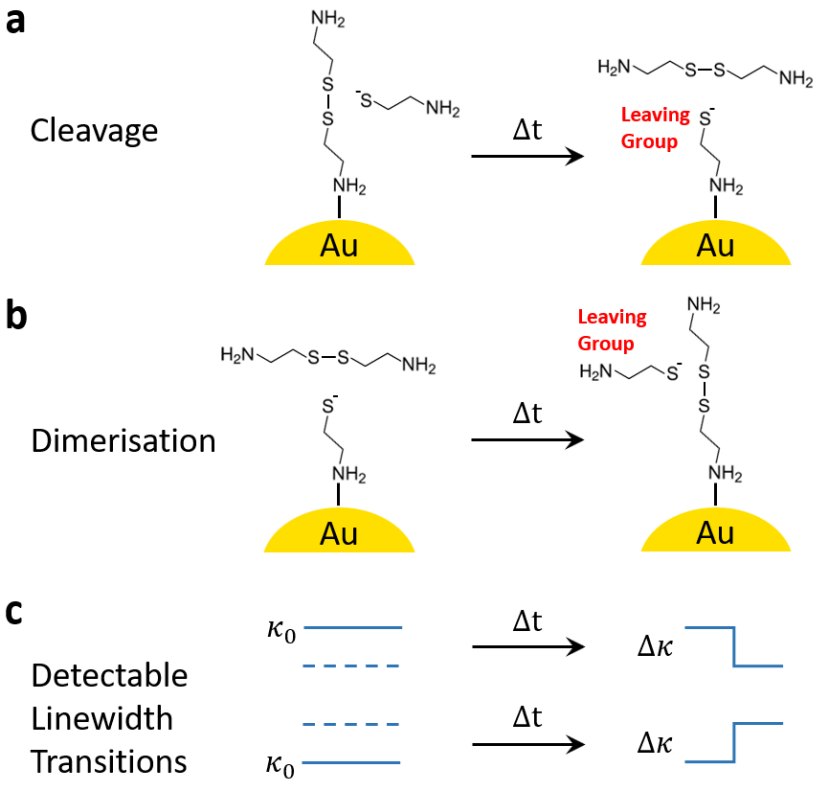

Figure 6.9: Thiol-disulfide exchange pathways. The leaving group may be discriminated based on the optoplasmonic linewidth signal post-disulfide exchange, i.e. a discrete step signifies (a) a single bound dimer that is cleaved or (b) a bound monomer that is dimerised. Further deductions in (c) require knowledge of the initial molecule state as binding can either narrow or broaden the linewidth (cf. Figure 6.2).

Supplementary Notes 2: Dilution Uncertainties

As this work involves trace element analysis nearing extreme concentration limits, we must consider propagating experimental uncertainties. Serial dilutions will amplify the absolute error Δc_i at each concentration stage c_i:

$$\frac{\Delta c_i}{c_i} = \sqrt{\left(\frac{\Delta V_i}{V_i}\right)^2 + \left(\frac{\Delta V_{\mathrm{T},i}}{V_{\mathrm{T},i}}\right)^2} \tag{6.3}$$

wherein we dilute a volume of dissolved analyte V_i, with absolute error ΔV_i, in a total volume $V_{\mathrm{T},i}$, with absolute error $\Delta V_{\mathrm{T},i}$. The variable pipettes for dispensing liquids in this protocol are *Gilson* P2L, P20L, and P1000L assemblies with respective maximal errors of ±0.030 μL for 1.0 μL, ±0.11 μL for 10 μL, and ±8.1 μL for 1000 μL. In all cases, the stock solution concentration is on the order of 1 mM. The concentration uncertainty then attained in the process of diluting to 100 aM, by diluting three times by a factor of 10^3 and once by a factor of 10^2, becomes:

$$\begin{aligned}\Delta c_{100\mathrm{aM}} &= (100\ \mathrm{aM})\sqrt{3\left(\frac{\pm 0.030\ \mu\mathrm{L}}{1.0\ \mu\mathrm{L}}\right)^2 + \left(\frac{\pm 0.11 \mu\mathrm{L}}{10\ \mu\mathrm{L}}\right)^2 + 4\left(\frac{\pm 8.1\ \mu\mathrm{L}}{1000\ \mu\mathrm{L}}\right)^2} \\ &= \pm 5.6\ \mathrm{aM}\end{aligned}$$

This estimated uncertainty, which is less than an order of magnitude, delineates the worst case deviation from expected concentrations for single-molecule detection when approaching 100 aM. The main manuscript omits such deviations for brevity purposes; notwithstanding, it is clear here that all stated concentrations inherent at most a 5.6% relative error.

6.2.1 Comments on Publication II

The reactive sensing principle predicts a WGM resonance wavelength shift proportional to the excess polarisability overlapping with the evanescent field. If nanoplasmonic enhancement of the near field estimates the sensitivity gain, then we can contemplate the possibility of unresolved mode splitting and that independent shifts in the split modes may cause an overall linewidth broadening or narrowing. This is unlikely, as we have seen that the LSP-WGM resonant wavelength shift does not scale linearly with the analyte's molecular mass when there is full overlap. Another experiment to test this claim would be to scan through scattering conditions by positioning a scatterer/tip near the WGM cavity while performing single-molecule measurements. With strong splitting signals like those in Figure 6.5c, the perturbation per molecule could be extensively decomposed.

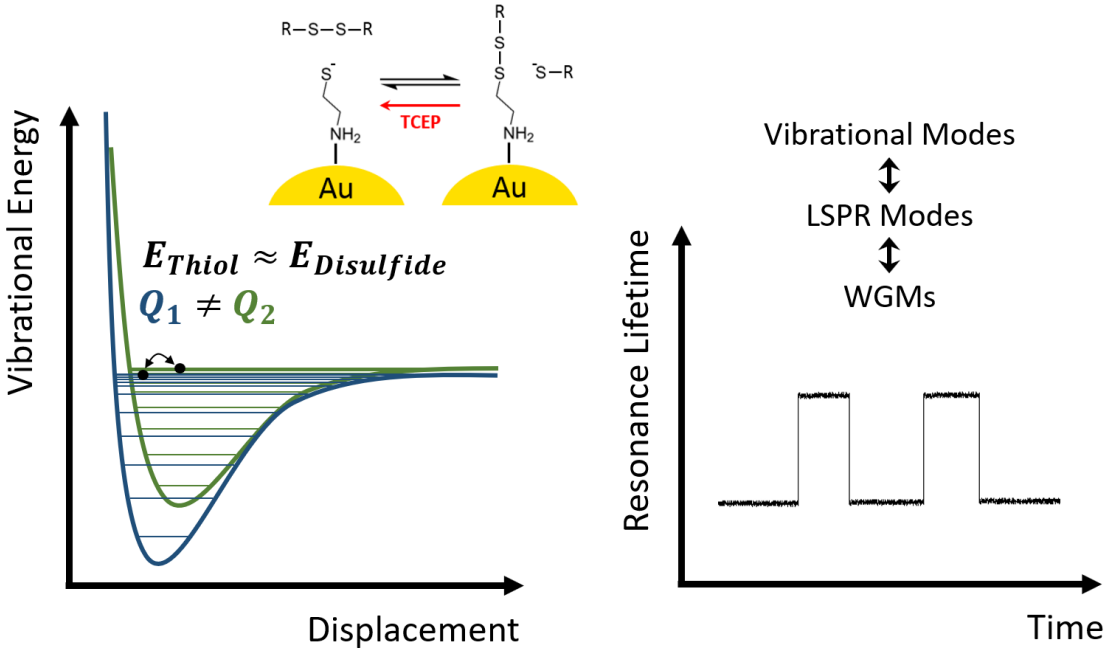

Figure 6.10: Optoplasmonic linewidth oscillation hypothesis. With thiol-disulfide exchange, the force extension/potential of the molecule is modified and so the quantised energy levels of the vibrational modes are reorganised. Through coupling of vibrational modes near the continuum limits to localised surface plasmon resonance (LSPR) modes, then from LSPR modes to the whispering-gallery modes (WGMs), we observe step signals in the measured WGM lifetime correlated to these potentials.

Furthermore, an optoplasmonic linewidth response from optomechanical plasmon-vibration coupling (Figure 6.10) can be researched in a pump-probe arrangement. When the pump is approximately blue-detuned from an LSP resonance by the vibrational frequency of a

single molecule, dynamical backaction enhancement will occur. Scanning the probe about the thiol-gold and amine-gold Raman peaks of the aminothiol can confirm specific surface binding and whether the amplitude of the linewidth step response depends on detuning. The extent of linewidth narrowing and/or broadening from the interacting molecule can be recorded by the probe, i.e. to verify that there is a sharp onset for the feedback mechanism and that the power dependence is nonlinear. The tuning should divulge the molecule's Raman spectrum without the necessity of far-field excitation, as it is possible to prism couple multiple wavelength-tuneable laser beams to the WGMs in order to pump and probe the plasmonic nanoantennae.

Chapter 7

Conclusions and Outlook

The research in this thesis demonstrates the potential for single-molecule fingerprinting by optoplasmonics. In Chapter 2, we put forward the remarkable temporal and spatial confinement capabilities of optical microcavities. Then, we showed how these could be married to the light amplification and shrinking properties of plasmonic nanoparticles. For a light-emitting atom in a cavity, the local density of optical modes can increase and so the emission rate can be enhanced. The physics there is similar to how light is recirculated in a whispering-gallery mode. Accordingly, it is the weak coupling of these modes with localised surface plasmon resonances of gold nanoparticles that permits us to eavesdrop onto the single-molecule reactions occurring near the nanoparticles. Optoplasmonic mechanisms for characterising single molecules were also outlined in Chapter 3.

In Chapter 4, we considered a magneto-optical microcavity system for discriminating chirality states. The intracavity Faraday effect was confirmed in a soft-glass microcavity; however, due to sensitivity limitations, we proceeded to opt for a hybrid resonator modality using chiral gold nanoantennae. The transient signals in Chapter 5 for single DL-cysteine and poly-DL-lysine were consistent with the molecular weight and diffusivity discrepancies between the analytes. Molecular chirality in the signal response was still obscured by factors such as the spatial heterogeneity of the sensing sites. Lastly, in Chapter 6, we tackled specificity by taking advantage of thiol/disulfide nanochemistry. This led to unprecedented signal patterns in the optoplasmonic resonant wavelength, linewidth, and mode splitting from reactions at gold-bound thiol sites. We hypothesised that an unchanging resonant wavelength with oscillating steps in the linewidth could be the byproduct of transitions between vibrational states in a molecule. When the states are very close in energy due to being in two separate potentials near the continuum, there can be two separate lifetimes/linewidths.

To expand on the work in this thesis, one could conduct a pump-probe experiment. The current excitation/tracking of the LSP-WGM resonance would act as the probe whereas a

guided mode or free-space beam would pump the plasmonic nanoparticles. Among these scenarios, two beam inputs at the prism coupler would abate photothermal absorption from the nanoantennae. With precise tuning of the pump, peaks in the linewidth oscillation amplitude (i.e. equivalent to Raman spectral peaks) would identify the vibrational modes specific to a detected molecule. 4-Aminothiophenol is a Raman active molecule whose spectrum is well studied through SERS, making it a fitting analyte for comparison with thiol-disulfide exchange based characterisation through the optoplasmonic sensor. Thiolated molecules can also be reversibly tethered to the thiol sites of the nanoantennae, suggesting that a variety of force extension measurements may be possible on this platform in the future. Wild-type or mutant proteins with disulfide cross-links between their domains could be investigated under thiol oxidation and disulfide reduction. As disulfides are formed or cleaved, structural information can be deduced from the sequence of signal steps. Several reaction branches could be profiled at the single-molecule level, along with more energetically unfavourable transitions. This has applications in drug discovery and viral infection where an isolated molecule has markedly different dynamics from an ensemble. If the time resolution is lowered far below milliseconds, the slowed oscillations in the chirality of a single hydrogen peroxide molecule may even become resolvable.

Appendix A

Full-Vector Finite-Difference Mode Solver

The Helmholtz equations for an electromagnetic wave can be rearranged into eigenvector/eigenvalue equations. Starting from (2.7) and (2.8) in Chapter 2, we can put aside boundary conditions to treat the fields as a scalar:

$$\nabla^2 \psi + k_0^2 \varepsilon_r \psi = 0 \tag{A.1}$$

In a cylindrical coordinate system that naturally applies to axisymmetric structures, with axial distance ρ, azimuth ϕ, and height z, we consider $\psi(\rho,\phi,z) = \psi(\rho,z)e^{\pm im\phi}$ such that the scalar Helmholtz equation becomes

$$\frac{\partial^2 \psi}{\partial \rho^2} + \frac{1}{\rho}\frac{\partial \psi}{\partial \rho} + \frac{\partial^2 \psi}{\partial z^2} + \left(k_0^2 \varepsilon_r - \frac{m^2}{\rho^2}\right)\psi = 0 \tag{A.2}$$

In the above geometry, any ρ-z cross-sectional plane may be discretised into an M-by-N grid. This leads to a matrix $\mathbf{A}$ and column vector $\boldsymbol{\psi}$ which we can relate in terms of

$$\begin{aligned} \mathbf{A}\boldsymbol{\psi} &= -k_o^2 \boldsymbol{\psi} \\ \mathbf{A}\begin{bmatrix} \psi_{1,1} \\ \vdots \\ \psi_{M,N} \end{bmatrix} &= -k_0^2 \begin{bmatrix} \psi_{1,1} \\ \vdots \\ \psi_{M,N} \end{bmatrix} \end{aligned} \tag{A.3}$$

It is straightforward to show that the first and second partial derivative operators applied to the field $\boldsymbol{\psi}$ by $\mathbf{A}$ are approximated by truncated Taylor series. At a point (i,j) in a ρ-z cross-section we can take central differences about the point with a stencil size, i.e. a grouping

with nearest neighbours, chosen according to the rate of convergence that we desire. As is elucidated in the author's MASc thesis [196], a 7-point stencil with uniform grid spacings $\Delta\rho = \Delta z$ is sufficient to achieve convergence of order 2.

Discontinuities in the permittivity profile $\varepsilon(\rho,z) = \varepsilon_0\varepsilon_r(\rho,z)$ absorbed into $\mathbf{A}$ force us to re-evaluate the boundary conditions we previously ignored. Optical media I and II on each side of an interface have continuity relations for the vector fields $\vec{E}$ and $\vec{H}$,

$$\hat{n} \times \left(\vec{E}_{\mathrm{I}} - \vec{E}_{\mathrm{II}}\right) = \vec{0} \tag{A.4}$$

$$\hat{n} \cdot \left(\varepsilon_{\mathrm{I}}\vec{E}_{\mathrm{I}} - \varepsilon_{\mathrm{II}}\vec{E}_{\mathrm{II}}\right) = 0 \tag{A.5}$$

$$\hat{n} \times \left(\vec{H}_{I} - \vec{H}_{\mathrm{II}}\right) = \vec{0} \tag{A.6}$$

$$\hat{n} \cdot \left(\vec{H}_{I} - \vec{H}_{\mathrm{II}}\right) = 0 \tag{A.7}$$

where $\hat{n}$ is the unit normal vector perpendicular to the interface. Application of (A.4)-(A.7) across this interface requires alignment of the field via local coordinate transformation. If a stencil contains points from multiple media, we would expand the Taylor series from the source node to the interface, rotate by a fixed angle θ towards the $\hat{n}$ unit vector, use the continuity relations, rotate by $-\theta$ back to the original coordinate system, then expand to the destination node. We can thus successively multiply matrix operators on E_ρ and E_z from a source node on side I to reach the destination node on side II as follows:

$$\begin{bmatrix} \mathrm{E}_{\rho|\mathrm{II}} \\ 0 \\ 0 \\ 0 \\ 0 \\ 0 \\ \mathrm{E}_{z|\mathrm{II}} \\ 0 \\ 0 \\ 0 \\ 0 \\ 0 \end{bmatrix} = \mathbf{T}_{i,j|\mathrm{II}}\mathbf{R}_{i,j}(-\theta)\mathbf{C}_{i,j}\mathbf{R}_{i,j}(\theta)\mathbf{T}_{i,j|\mathrm{I}} \begin{bmatrix} \mathrm{E}_{\rho|\mathrm{I}} \\ \partial_\rho \mathrm{E}_{\rho|\mathrm{I}} \\ \partial_z \mathrm{E}_{\rho|\mathrm{I}} \\ \partial_\rho^2 \mathrm{E}_{\rho|\mathrm{I}} \\ \partial_{\rho z} \mathrm{E}_{\rho|\mathrm{I}} \\ \partial_z^2 \mathrm{E}_{\rho|\mathrm{I}} \\ \mathrm{E}_{z|\mathrm{I}} \\ \partial_\rho \mathrm{E}_{z|\mathrm{I}} \\ \partial_z \mathrm{E}_{z|\mathrm{I}} \\ \partial_\rho^2 \mathrm{E}_{z|\mathrm{I}} \\ \partial_{\rho z} \mathrm{E}_{z|\mathrm{I}} \\ \partial_z^2 \mathrm{E}_{z|\mathrm{I}} \end{bmatrix} \tag{A.8}$$

where $\mathbf{T}_{i,j}$, $\mathbf{R}_{i,j}$, and $\mathbf{C}_{i,j}$ are the Taylor series, rotation, and continuity relation matrices, respectively. Since we can condense the operators into $\mathbf{B}_{i,j} = \mathbf{T}_{i,j|\mathrm{II}}\mathbf{R}_{i,j}(-\theta)\mathbf{C}_{i,j}\mathbf{R}_{i,j}(\theta)\mathbf{T}_{i,j|\mathrm{I}}$

and invert $\mathbf{B}_{i,j}$, collecting $\mathbf{T}_{i,j}^{-1}$ and $\mathbf{B}_{i,j}^{-1}$ to express a central stencil field in terms of a linear combination of stencil fields at every grid point will complete $\mathbf{A}$. We can now modify (A.3) to account for all the E- and H-field components by computing the eigenvectors $\boldsymbol{E_\rho}$ and $\boldsymbol{E_z}$ with eigenvalue $2\pi/k_0 = \lambda_0 \to \lambda_{Res}$:

$$\begin{aligned} \mathbf{A}\begin{bmatrix} \boldsymbol{E_\rho} \\ \boldsymbol{E_z} \end{bmatrix} &= -k_0^2 \begin{bmatrix} \boldsymbol{E_\rho} \\ \boldsymbol{E_z} \end{bmatrix} \\ \mathbf{A}\begin{bmatrix} \mathrm{E}_\rho|_{(1,1)} \\ \vdots \\ \mathrm{E}_\rho|_{(M,N)} \\ \mathrm{E}_z|_{(1,1)} \\ \vdots \\ \mathrm{E}_z|_{(M,N)} \end{bmatrix} &= -k_0^2 \begin{bmatrix} \mathrm{E}_\rho|_{(1,1)} \\ \vdots \\ \mathrm{E}_\rho|_{(M,N)} \\ \mathrm{E}_z|_{(1,1)} \\ \vdots \\ \mathrm{E}_z|_{(M,N)} \end{bmatrix} \end{aligned} \tag{A.9}$$

which serves as an input for Maxwell's equations to compute $\boldsymbol{E_\phi}$, $\boldsymbol{H_\rho}$, $\boldsymbol{H_z}$, and $\boldsymbol{H_\phi}$. Here, we assume the azimuthal mode order m to be a purely real integer; by consequence, the eigenvalue λ_{Res} becomes complex. The calculation of the ratio

$$Q = \frac{\mathrm{Re}\,(\lambda_{Res})}{2\mathrm{Im}\,(\lambda_{Res})} \tag{A.10}$$

provides a rough estimate of a computed mode's quality factor [197].

A.1 Predicted Intracavity Faraday Effect

Under realistic experimental circumstances, a fabricated WGM microsphere is either oblate or prolate as to lift $l-m$ degeneracy. Quasi-TE and quasi-TM WGMs, however, have different penetration depths into their surroundings and so the nonzero difference between their eigenvalues $\lambda_{Res,TE} - \lambda_{Res,TM}$ factors into the geometrical birefringence $\Delta n_g = n_{TE} - n_{TM}$. For a tellurite sphere with radius $a = 50$ μm and Verdet constant $V \approx 25$ rad/(T·m) at a wavelength $\lambda = 633$ nm, the geometrical birefringence operating point of Figure 4.5a comes from

$$\Delta n_g \approx \frac{m}{2\pi a}\left(\lambda_{Res,TE} - \lambda_{Res,TM}\right) = 0.00146 \tag{A.11}$$

for a fundamental quasi-TE and quasi-TM WGM at m =975 computed from the full-vector mode solver. The coupled mode theory from [121] accounts for this quenching of the Faraday

rotation through the term

$$\Delta\beta = \frac{2\pi}{\lambda}\Delta n_g \tag{A.12}$$

and the matrix elements that determine the polarisation rotation of the output field $\boldsymbol{E}_{out}$. For a TE-polarised input, matrix equation (4.3) is used to plot

$$\theta_F = \arctan \frac{\left| |\kappa|^2 \frac{2F}{\phi} g(\theta,\gamma) \right|}{\left| t - |\kappa|^2 \left[f(\theta,\gamma) - i\frac{\Delta\beta}{\phi} g(\theta,\gamma) \right] \right|} \tag{A.13}$$

for $0 \leq \Delta n_g \leq 0.002$ and the external magnetic fields $B = 2$, 5, 10, and 20 G. Remaining parameters, such as the coefficients t and κ, conform to the literature [121].

Alternatively, for a fused silica microsphere of radius $a = 500\ \mu$m with $V \approx 0.56$ rad/(T·m) near $\lambda = 1550$ nm, we can set Δn_g to 3.54×10^{-4} and inspect the shifting TE and TM resonances in the normalised transmitted power spectrum. In Figure A.1, a B-field oscillation frequency of 16.7 mHz is shown to result in a partial-wave rectified signal response at twice the oscillation frequency.

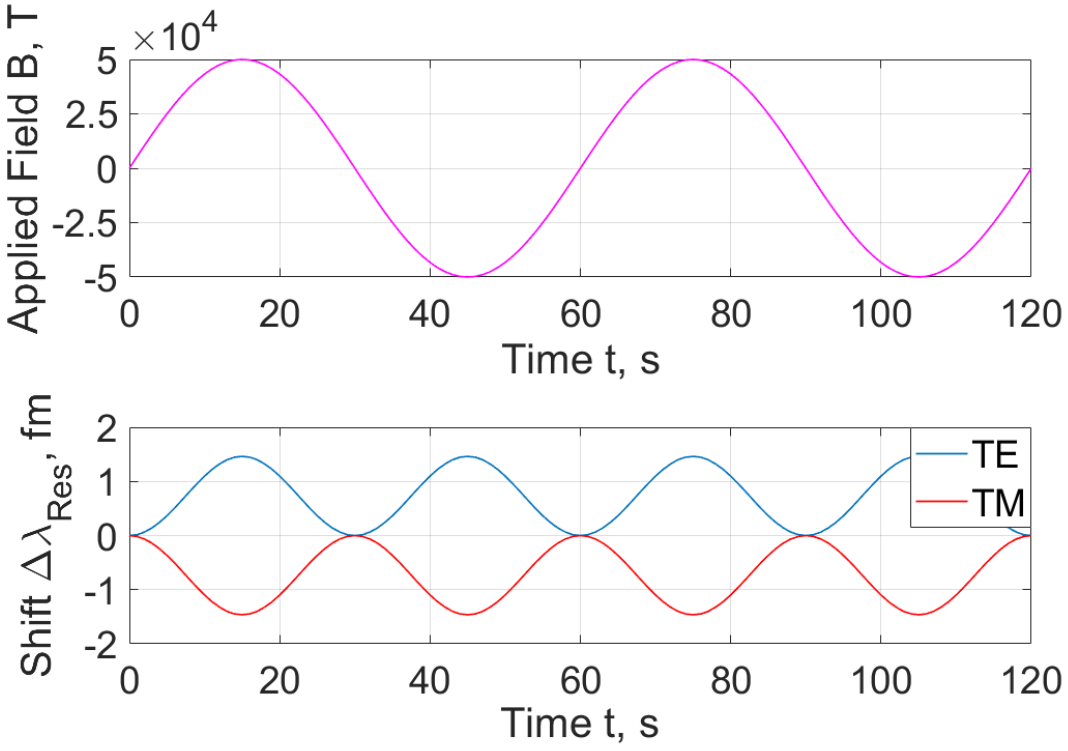

Figure A.1: Analytical TE and TM resonance perturbations from the intracavity Faraday effect for a 500-μm silica microsphere with excitation wavelength close to 1550 nm.

The TE and TM resonances deviate from the $\Delta n_g = 0$ degeneracy point with increasing magnitude of B. As there are two half cycles for the signal $\Delta\lambda_{Res,TE} - \Delta\lambda_{Res,TM}$ tied to orthogonal, optical chirality states, this mode mixing should discriminate the light-matter interaction with a chiral species depending on the analyte's mixed electric-magnetic dipole polarisability ξ. For the detection of a single biomolecule, no matter whether it is achiral or chiral, the baseline sensitivity of a WGM sensor is a limiting factor as the resonance perturbation must be large enough to surpass the laser frequency noise of the probing light source. Sensitivity is therefore a figure of merit warranting revision. The prospect of hybridising WGMs with LSPs by depositing plasmonic nanoparticles onto the surface of a magneto-optical WGM cavity and carrying out chiral polarimetry of single biomolecules, while preserving optical chirality, may be one of many platforms for discriminating single-molecule chirality. Such a system does not yet, to the best of the author's knowledge, have a theoretical or numerical grounding.

Appendix B

Glass Melting

WGM microspheres are traditionally formed by CO_2 laser reflow of a commercial optical fibre tip. Cohesive forces of surface tension dominate during melting to establish a smooth surface with a scattering loss contingent on contamination. Since greater temperature control and isotropic heating were required when melting soft glasses, a microheater was favoured over an optical absorption based approach. The first candidate magneto-optical glass selected for fabrication was tellurite ($78TeO_2$-$12ZnO$-$10Na_2O$) drawn into tubules. A metal, such as a 100-μm diameter gold wire, was then placed inside these tubules only to have the tellurite crystallise when heated (cf. Figure B.1).

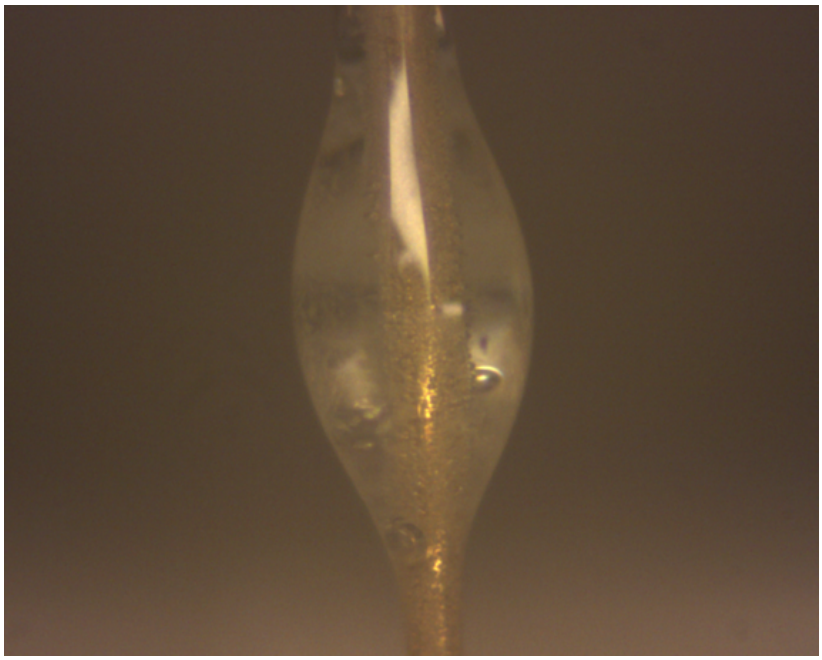

Figure B.1: Crystallisation of a tellurite microdroplet about a 50-μm radius gold wire during convective heating.

It was hypothesised that crystallisation occurs due to nitrogen entering the soft glass during melting of the capillaries. Without purging the atmosphere in the microheater's furnace, there are nitrogen centres in the glass that will expand at melting temperatures as to seed nucleation sites. Crystal growth then takes hold as the microdroplet develops. Such centres near the glass/metal interface are displayed in Figure B.2.

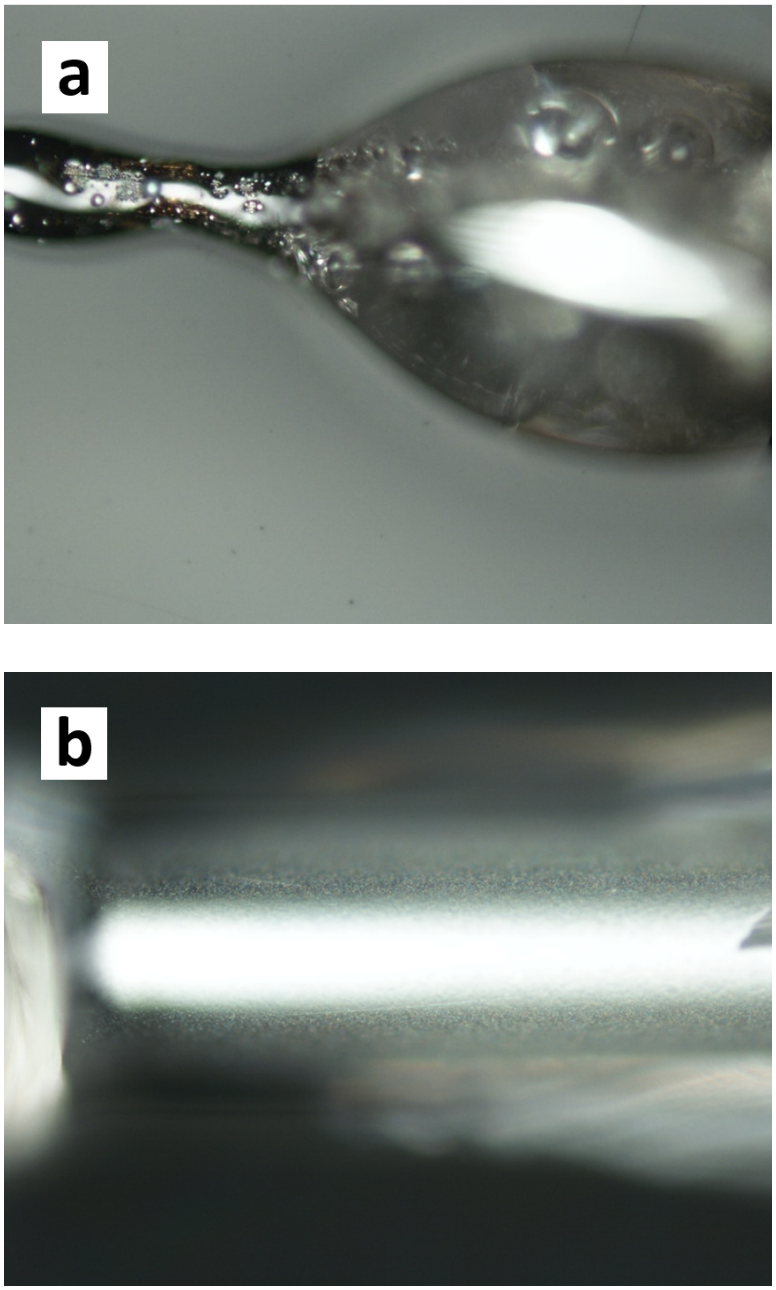

Figure B.2: Optically resolved image of a crystallised tellurite microdroplet surrounding a 50-μm radius tungsten wire through a (a) 10x objective and (b) 40x objective.

If a soft glass indeed contains colour centres, their existence may be validated through photoluminescence. The electronic spin state of the centres can be excited by absorption around a given wavelength, for example, to then transition back and produce sharp fluorescence intensity peaks. Exploiting colour centres in soft glasses, however, lies outside the scope of this thesis. The author refers the reader to works in which tellurite is embedded with nanodiamonds for use in quantum and sensing studies [198, 199].

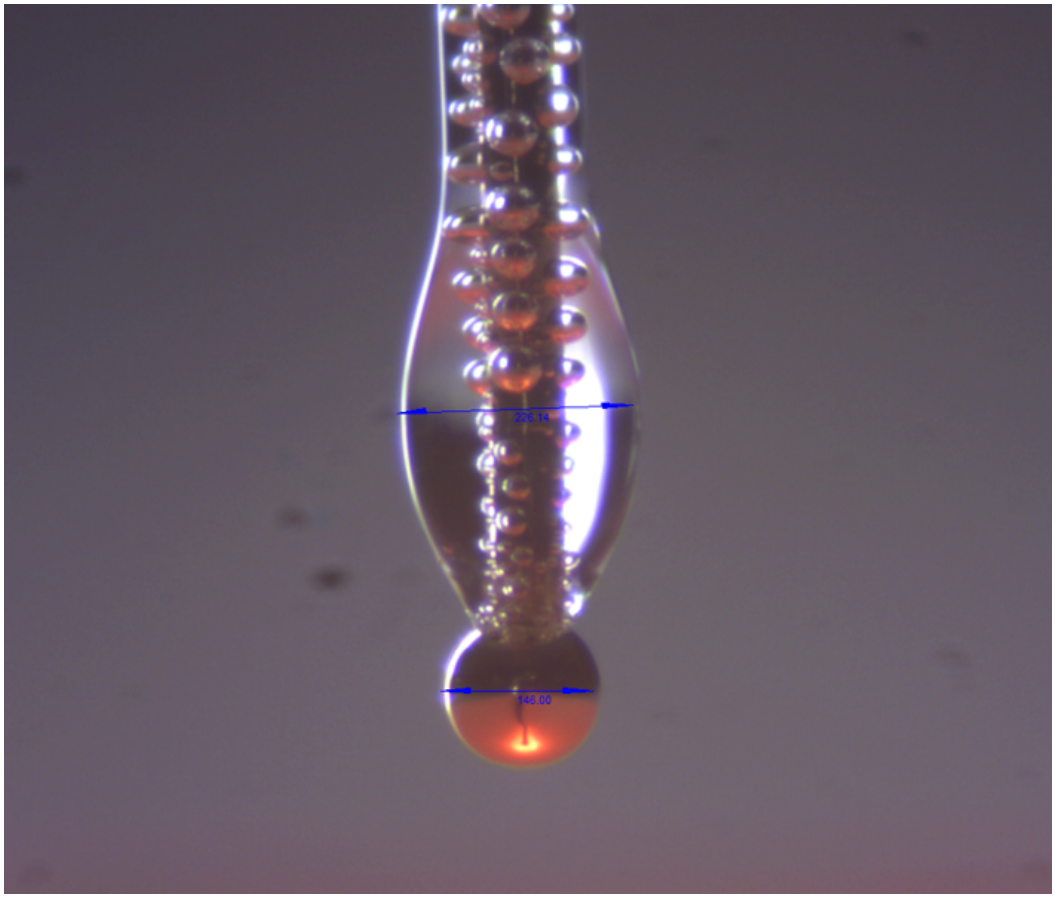

Figure B.3: Inhibited resonator fabrication when borosilicate glass is paired with gold.

The melting point of the glass versus the metal is a determinant in successfully fabricating a cavity-wire construct. A glass with a higher melting point than the conducting wire can reshape the latter before the glass softens. Moreover, oxidisation of the metal in air prior to reaching softening temperatures precludes certain pairings of materials. Figure B.3 shows such ramifications for microcavity fabrication of a borosilicate capillary about a gold wire. Lowering of the nucleation barrier is evident here as is the reshaping of the wire protrusion into a sphere that precedes glass microdroplet formation.

B.1 Operational Soft Glass Microcavities

To host high-Q WGMs, a microstructure should retain circular symmetry about its zenith (i.e. if single-clamped, the surface coordinate opposite to its stem connection) and the cavity material should be amorphous. A glass with slower crystallisation rate, such as a germanate ($56GeO_2$-$31PbO$-$9Na_2O$-$4Ga_2O_3$), also lessens crystal growth within the time needed to form a microdroplet resonator. Despite this the integration of a conductor within the WGM cavity (Figure B.4) compromises the quality factor, placing it on the order of 10^5 as confirmed by WGM resonances recorded in the transmission spectrum. As germanate's refractive index again exceeds that of the N-SF 11 that often makes up a coupling prism, we must rely on a high-index prism material (e.g. diamond or titanium dioxide) to satisfy frustrated total internal reflection conditions.

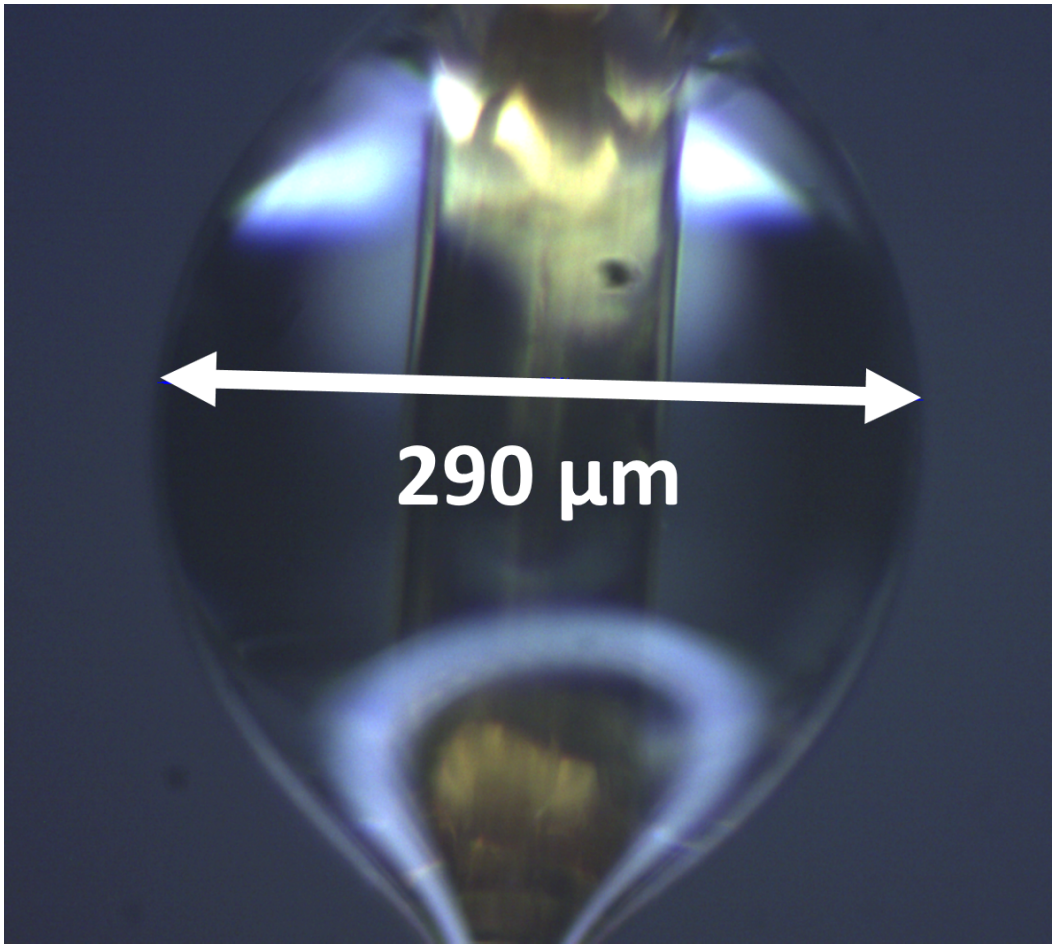

Figure B.4: A germanate microdroplet encapsulating a 100-μm diameter gold conductor.

Bibliography

1. Abbe, E. Beiträge zur Theorie des Mikroskops und der mikroskopischen Wahrnehmung. *Archiv für Mikroskopische Anatomie* **9,** 413–468 (1873).

2. Moerner, W. E. & Kador, L. Optical detection and spectroscopy of single molecules in a solid. *Physical Review Letters* **62,** 2535–2538 (1989).

3. Betzig, E., Chichester, R. J., Lanni, F. & Taylor, D. L. Near-field fluorescence imaging of cytoskeletal actin. *Bioimaging* **1,** 129–135 (1993).

4. Betzig, E. & Chichester, R. J. Single Molecules Observed by Near-Field Scanning Optical Microscopy. *Science* **262,** 1422–1425 (1993).

5. Rust, M., Bates, M. & Zhuang, X. Sub-diffraction-limit imaging by stochastic optical reconstruction microscopy (STORM). *Nature Methods* **3,** 793–796 (2006).

6. Betzig, E. *et al.* Imaging Intracellular Fluorescent Proteins at Nanometer Resolution. *Science* **313,** 1642–1645 (2006).

7. Hess, S. T., Girirajan, T. P. K. & Mason, M. D. Ultra-High Resolution Imaging by Fluorescence Photoactivation Localization Microscopy. *Biophysical Journal* **91,** 4258–4272 (2006).

8. Arroyo, J. O., Cole, D. & Kukura, P. Interferometric scattering microscopy and its combination with single-molecule fluorescence imaging. *Nature Protocols* **11,** 617–633 (2016).

9. Zhang, P. *et al.* Plasmonic scattering imaging of single proteins and binding kinetics. *Nature Methods* **17,** 1010–1017 (2020).

10. Wales, T. E. & Engen, J. R. Hydrogen exchange mass spectrometry for the analysis of protein dynamics. *Mass Spectrometry Reviews* **25,** 158–170 (2006).

11. Kay, L. E. NMR studies of protein structure and dynamics. *Journal of Magnetic Resonance* **173,** 193–207 (2005).

12. Kikhney, A. G. & Svergun, D. I. A practical guide to small angle X-ray scattering (SAXS) of flexible and intrinsically disordered proteins. *FEBS Letters* **589,** 2570–2577 (2015).

13. Neuman, K. C. & Nagy, A. Single-molecule force spectroscopy: optical tweezers, magnetic tweezers and atomic force microscopy. *Nature Methods* **5,** 491–505 (2008).

14. Lipfert, J., Kerssemakers, J. W. J., Jager, T. & Dekker, N. H. Magnetic torque tweezers: measuring torsional stiffness in DNA and RecA-DNA filaments. *Nature Methods* **7,** 977–980 (2010).

15. Janssen, X. J. A. *et al.* Electromagnetic torque tweezers: a versatile approach for measurement of single-molecule twist and torque. *Nano Letters* **12,** 3634–3639 (2012).

16. Bullard, B. *et al.* Association of the Chaperone αB-crystallin with Titin in Heart Muscle. *The Journal OF Biological Chemistry* **279,** 7917–7924 (2004).

17. Bullard, B. *et al.* The molecular elasticity of the insect flight muscle proteins projectin and kettin. *Proceedings of the National Academy of Sciences* **103,** 4451–4456 (2006).

18. C.Leake, M., Grötzner, A., Krüger, M. & A.Linke, W. Mechanical properties of cardiac titin's N2B-region by single-molecule atomic force spectroscopy. *Journal of Structural Biology* **155,** 263–272 (2006).

19. Shopova, S. I., Rajmangal, R., Holler, S. & Arnold, S. Plasmonic enhancement of a whispering-gallery-mode biosensor for single nanoparticle detection. *Applied Physics Letters* **98,** 243104 (2011).

20. Santiago-Cordoba, M. A., Boriskina, S. V., Vollmer, F. & Demirel, M. C. Nanoparticle-based protein detection by optical shift of a resonant microcavity. *Applied Physics Letters* **99,** 073701 (2011).

21. Swaim, J. D., Knittel, J. & Bowen, W. P. Detection limits in whispering gallery biosensors with plasmonic enhancement. *Applied Physics Letters* **99,** 243109 (2011).

22. Baaske, M. D., Foreman, M. R. & Vollmer, F. Single-molecule nucleic acid interactions monitored on a label-free microcavity biosensor platform. *Nature Nanotechnology* **9,** 933–939 (2014).

23. Vincent, S., Jiang, X., Russell, P. & Vollmer, F. Thermally tunable whispering-gallery mode cavities for magneto-optics. *Applied Physics Letters* **116,** 161110 (2020).

24. Lee, H.-E. *et al.* Amino-acid- and peptide-directed synthesis of chiral plasmonic gold nanoparticles. *Nature* **556,** 360–365 (2018).

25. Vincent, S., Subramanian, S. & Vollmer, F. Optoplasmonic characterisation of reversible disulfide interactions at single thiol sites in the attomolar regime. *Nature Communications* **11,** 2043 (2020).

26. Yablonovitch, E. Inhibited Spontaneous Emission in Solid-State Physics and Electronics. *Physical Review Letters* **58,** 2059–2062 (1987).

27. Gérard, J. *et al.* Enhanced Spontaneous Emission by Quantum Boxes in a Monolithic Optical Microcavity. *Physical Review Letters* **81,** 1110–1113 (1998).

28. Spillane, S. M., Kippenberg, T. J. & Vahala, K. J. Ultralow-threshold Raman laser using a spherical dielectric microcavity. *Nature* **415,** 621–623 (2002).

29. Vernooy, D. W., Furusawa, A., Georgiades, N. P., Ilchenko, V. S. & Kimble, H. J. Cavity QED with high-Q whispering gallery modes. *Physical Review A* **57,** R2293–R2296 (1998).

30. Rayleigh, L. CXII. The problem of the whispering gallery. *The London, Edinburgh, and Dublin Philosophical Magazine and Journal of Science* **20,** 1001–1004 (1910).

31. Richtmyer, R. D. Dielectric Resonators. *Journal of Applied Physics* **10,** 391–398 (1939).

32. Ashkin, A. & Dziedzic, J. M. Observation of Resonances in the Radiation Pressure on Dielectric Spheres. *Physical Review Letters* **38,** 1351–1354 (1977).

33. Benner, R. E., Barber, P. W., Owen, J. F. & Chang, R. K. Observation of Structure Resonances in the Fluorescence Spectra from Microspheres. *Physical Review Letters* **44,** 475–478 (1980).

34. Braginsky, V., Gorodetsky, M. & Ilchenko, V. Quality-factor and nonlinear properties of optical whispering-gallery modes. *Physics Letters A* **137,** 393–397 (1989).

35. Smith, G. *Grant Smith Photography.* http://www.grant-smith.com. Accessed 20 February 2020.

36. Lam, C. C., Leung, P. T. & Young, K. Explicit asymptotic formulas for the positions, widths, and strengths of resonances in Mie scattering. *Journal of the Optical Society of America B* **9,** 1585–1592 (1992).

37. Schiller, S. Asymptotic expansion of morphological resonance frequencies in Mie scattering. *Applied Optics* **32,** 2181–2185 (1993).

38. Strekalov, D. V., Thompson, R. J., Baumgartel, L. M., Grudinin, I. S. & Yu, N. Temperature measurement and stabilization in a birefringent whispering gallery mode resonator. *Optics Express* **19,** 14495–14501 (2011).

39. Weng, W. *et al.* Nano-Kelvin Thermometry and Temperature Control: Beyond the Thermal Noise Limit. *Physical Review Letters* **112,** 160801 (2014).

40. Muljarov, E. A. & Langbein, W. Exact mode volume and Purcell factor of open optical systems. *Physical Review B* **94,** 235438 (2016).

41. Gorodetsky, M. L., Savchenkov, A. A. & Ilchenko, V. S. Ultimate Q of optical microsphere resonators. *Optics Letters* **21,** 453–455 (1996).

42. Cai, M., Painter, O. & Vahala, K. J. Observation of Critical Coupling in a Fiber Taper to a Silica-Microsphere Whispering-Gallery Mode System. *Physical Review Letters* **85,** 74–77 (2000).

43. Collot, L., Lefèvre-Seguin, V., Brune, M., Raimond, J. M. & Haroche, S. Very High-*Q* Whispering-Gallery Mode Resonances Observed on Fused Silica Microspheres. *Europhysics Letters (EPL)* **23,** 327–334 (1993).

44. Haus, H., Huang, W., Kawakami, S. & Whitaker, N. Coupled-mode theory of optical waveguides. *Journal of Lightwave Technology* **LT-5,** 16–23 (1987).

45. Haus, H. & Huang, W. Coupled-mode theory. *Proceedings of the IEEE* **79,** 1505–1518 (1991).

46. Kippenberg, T. J. *Nonlinear Optics in Ultra-high-Q Whispering-Gallery Optical Microcavities.* PhD thesis (California Institute of Technology, 2004).

47. Qian, S.-X., Snow, J. B., Tzeng, H.-M. & Chang, R. K. Lasing Droplets: Highlighting the Liquid-Air Interface by Laser Emission. *Science* **231,** 486–488 (1986).

48. Zhang, J.-Z. & Chang, R. K. Generation and suppression of stimulated Brillouin scattering in single liquid droplets. *Journal of the Optical Society of America B* **6,** 151–153 (1989).

49. Campillo, A. J., Eversole, J. D. & Lin, H.-B. Cavity quantum electrodynamic enhancement of stimulated emission in microdroplets. *Physical Review Letters* **67,** 437–440 (1991).

50. Lin, H.-B. & Campillo, A. J. cw Nonlinear Optics in Droplet Microcavities Displaying Enhanced Gain. *Physical Review Letters* **73,** 2440–2443 (1994).

51. Lin, H.-B. & Campillo, A. Microcavity enhanced Raman gain. *Optics Communications* **133,** 287–292 (1997).

52. Grudinin, I., Lee, H., Chen, T. & Vahala, K. Compensation of thermal nonlinearity effect in optical resonators. *Optics Express* **19,** 7365–7372 (2011).

53. Carmon, T., Yang, L. & Vahala, K. J. Dynamical thermal behavior and thermal self-stability of microcavities. *Optics Express* **12,** 4742–4750 (2004).

54. Zhu, J. *et al.* On-chip single nanoparticle detection and sizing by mode splitting in an ultrahigh-Q microresonator. *Nature Photonics* **4,** 46–49 (2009).

55. Foreman, M. R., Keng, D., Treasurer, E., Lopez, J. R. & Arnold, S. Whispering gallery mode single nanoparticle detection and sizing: the validity of the dipole approximation. *Optics Letters* **42,** 963–966 (2017).

56. Diddams, S. A. *et al.* Direct Link between Microwave and Optical Frequencies with a 300 THz Femtosecond Laser Comb. *Physical Review Letters* **84,** 5102–5105 (2000).

57. Kippenberg, T. J., Holzwarth, R. & Diddams, S. A. Microresonator-Based Optical Frequency Combs. *Science* **332,** 555–559 (2011).

58. Lu, T., Yang, L., van Loon, R. V. A., Polman, A. & Vahala, K. J. On-chip green silica upconversion microlaser. *Optics Letters* **34,** 482–484 (2009).

59. Grudinin, I. S., Matsko, A. B. & Maleki, L. Brillouin Lasing with a CaF_2 Whispering Gallery Mode Resonator. *Physical Review Letters* **102,** 043902 (2009).

60. Peng, B. *et al.* Parity–time-symmetric whispering-gallery microcavities. *Nature Physics* **10,** 394–398 (2014).

61. Chen, W., Özdemir, Ş. K., Zhao, G., Wiersig, J. & Yang, L. Exceptional points enhance sensing in an optical microcavity. *Nature* **548,** 192–196 (2017).

62. Carmon, T., Rokhsari, H., Yang, L., Kippenberg, T. J. & Vahala, K. J. Temporal Behavior of Radiation-Pressure-Induced Vibrations of an Optical Microcavity Phonon Mode. *Physical Review Letters* **94,** 223902 (2005).

63. Kippenberg, T. J., Rokhsari, H., Carmon, T., Scherer, A. & Vahala, K. J. Analysis of Radiation-Pressure Induced Mechanical Oscillation of an Optical Microcavity. *Physical Review Letters* **95,** 033901 (2005).

64. Schliesser, A., Del'Haye, P., Nooshi, N., Vahala, K. J. & Kippenberg, T. J. Radiation Pressure Cooling of a Micromechanical Oscillator Using Dynamical Backaction. *Physical Review Letters* **97,** 243905 (2006).

65. Bahl, G. *et al.* Brillouin cavity optomechanics with microfluidic devices. *Nature Communications* **4,** 1994 (2013).

66. Dahan, R., Martin, L. L. & Carmon, T. Droplet optomechanics. *Optica* **3,** 175–178 (2016).

67. Yu, W., Jiang, W. C., Lin, Q. & Lu, T. Cavity optomechanical spring sensing of single molecules. *Nature Communications* **7,** 12311 (2016).

68. Stockman, M. I. Nanoplasmonics: The physics behind the applications. *Physics Today* **64,** 39–44 (2011).

69. Tobiška, P., Hugon, O., Trouillet, A. & Gagnaire, H. An integrated optic hydrogen sensor based on SPR on palladium. *Sensors and Actuators B: Chemical* **74,** 168–172 (2001).

70. Baldelli, S., Eppler, A. S., Anderson, E., Shen, Y.-R. & Somorjai, G. A. Surface enhanced sum frequency generation of carbon monoxide adsorbed on platinum nanoparticle arrays. *The Journal of Chemical Physics* **113,** 5432–5438 (2000).

71. Novotny, L. & Hecht, B. *Principles of Nano-Optics* (Cambridge University Press, Cambridge, 2006).

72. Bohren, C. F. & Huffman, D. R. *Absorption and Scattering of Light by Small Particles* (Wiley, New York, 1998).

73. Maier, S. A. *Plasmonics: Fundamentals and Applications* (Springer, New York, 2007).

74. Ashkin, A., Dziedzic, J. M., Bjorkholm, J. E. & Chu, S. Observation of a single-beam gradient force optical trap for dielectric particles. *Optics Letters* **11,** 288–290 (1986).

75. Block, S. M., Goldstein, L. S. B. & Schnapp, B. J. Bead movement by single kinesin molecules studied with optical tweezers. *Nature* **348,** 348–352 (1990).

76. Kneipp, K. *et al.* Single Molecule Detection Using Surface-Enhanced Raman Scattering (SERS). *Physical Review Letters* **78,** 1667–1670 (1997).

77. Nie, S. & Emory, S. R. Probing Single Molecules and Single Nanoparticles by Surface-Enhanced Raman Scattering. *Science* **275,** 1102–1106 (1997).

78. Zijlstra, P., Paulo, P. M. R. & Orrit, M. Optical detection of single non-absorbing molecules using the surface plasmon resonance of a gold nanorod. *Nature Nanotechnology* **7,** 379–382 (2012).

79. Xu, B. & Tao, N. J. Measurement of Single-Molecule Resistance by Repeated Formation of Molecular Junctions. *Science* **301,** 1221–1223 (2003).

80. Garaj, S. *et al.* Graphene as a subnanometre trans-electrode membrane. *Nature* **467,** 190–193 (2010).

81. Sorgenfrei, S. *et al.* Label-free single-molecule detection of DNA-hybridization kinetics with a carbon nanotube field-effect transistor. *Nature Nanotechnology* **6,** 126–132 (2011).

82. Gross, L., Mohn, F., Moll, N., Liljeroth, P. & Meyer, G. The Chemical Structure of a Molecule Resolved by Atomic Force Microscopy. *Science* **325,** 1110–1114 (2009).

83. Hanay, M. S. *et al.* Single-protein nanomechanical mass spectrometry in real time. *Nature Nanotechnology* **7,** 602–608 (2012).

84. Ndieyira, J. W. *et al.* Surface-stress sensors for rapid and ultrasensitive detection of active free drugs in human serum. *Nature Nanotechnology* **9,** 225–232 (2014).

85. Cui, L. *et al.* Thermal conductance of single-molecule junctions. *Nature* **572,** 628–633 (2019).

86. Arnold, S., Khoshsima, M., Teraoka, I., Holler, S. & Vollmer, F. Shift of whispering-gallery modes in microspheres by protein adsorption. *Optics Letters* **28,** 272–274 (2003).

87. Luchansky, M. S. *et al.* Characterization of the evanescent field profile and bound mass sensitivity of a label-free silicon photonic microring resonator biosensing platform. *Biosensors and Bioelectronics* **26,** 1283–1291 (2010).

88. Keng, D., Tan, X. & Arnold, S. Whispering gallery micro-global positioning system for nanoparticle sizing in real time. *Applied Physics Letters* **105,** 071105 (2014).

89. Arnold, S., Ramjit, R., Keng, D., Kolchenko, V. & Teraoka, I. MicroParticle photophysics illuminates viral bio-sensing. *Faraday Discussions* **137,** 65–83 (2008).

90. Foreman, M. R., Jin, W.-L. & Vollmer, F. Optimizing detection limits in whispering gallery mode biosensing. *Optics Express* **22,** 5491–5511 (2014).

91. Drever, R. W. P. *et al.* Laser phase and frequency stabilization using an optical resonator. *Applied Physics B Photophysics and Laser Chemistry* **31,** 97–105 (1983).

92. Santiago-Cordoba, M. A., Cetinkaya, M., Boriskina, S. V., Vollmer, F. & Demirel, M. C. Ultrasensitive detection of a protein by optical trapping in a photonic-plasmonic microcavity. *Journal of Biophotonics* **5,** 629–638 (2012).

93. Baaske, M. D. & Vollmer, F. Optical observation of single atomic ions interacting with plasmonic nanorods in aqueous solution. *Nature Photonics* **10,** 733–739 (2016).

94. Foreman, M. R., Swaim, J. D. & Vollmer, F. Whispering gallery mode sensors. *Advances in Optics and Photonics* **7,** 168–240 (2015).

95. Shao, L. *et al.* Detection of Single Nanoparticles and Lentiviruses Using Microcavity Resonance Broadening. *Advanced Materials* **25,** 5616–5620 (2013).

96. Heylman, K. D. *et al.* Optical microresonators as single-particle absorption spectrometers. *Nature Photonics* **10,** 788–795 (2016).

97. Kenkre, V. M., Tokmakoff, A. & Fayer, M. D. Theory of vibrational relaxation of polyatomic molecules in liquids. *The Journal of Chemical Physics* **101,** 10618–10629 (1994).

98. Roelli, P., Galland, C., Piro, N. & Kippenberg, T. J. Molecular cavity optomechanics as a theory of plasmon-enhanced Raman scattering. *Nature Nanotechnology* **11,** 164–169 (2015).

99. Humbert, C., Pluchery, O., Lacaze, E., Tadjeddine, A. & Busson, B. A multiscale description of molecular adsorption on gold nanoparticles by nonlinear optical spectroscopy. *Phys. Chem. Chem. Phys.* **14,** 280–289 (2012).

100. Zhu, W. & Crozier, K. B. Quantum mechanical limit to plasmonic enhancement as observed by surface-enhanced Raman scattering. *Nature Communications* **5,** 5228 (2014).

101. Kukanskis, K. *et al.* Detection of DNA Hybridization Using the TISPR-1 Surface Plasmon Resonance Biosensor. *Analytical Biochemistry* **274,** 7–17 (1999).

102. Pasteur, L. Sur les relations qui peuvent exister entre la forme cristalline, la composition chimique et le sens de la polarisation rotatoire. *Annales de Chimie et de Physique* **24,** 442–459 (1848).

103. Frank, F. On spontaneous asymmetric synthesis. *Biochimica et Biophysica Acta* **11,** 459–463 (1953).

104. Soai, K., Shibata, T., Morioka, H. & Choji, K. Asymmetric autocatalysis and amplification of enantiomeric excess of a chiral molecule. *Nature* **378,** 767–768 (1995).

105. Blackmond, D. G., McMillan, C. R., Ramdeehul, S., Schorm, A. & Brown, J. M. Origins of Asymmetric Amplification in Autocatalytic Alkylzinc Additions. *Journal of the American Chemical Society* **123,** 10103–10104 (2001).

106. Bailey, J. *et al.* Circular Polarization in Star- Formation Regions: Implications for Biomolecular Homochirality. *Science* **281,** 672–674 (1998).

107. Wu, C. S., Ambler, E., Hayward, R. W., Hoppes, D. D. & Hudson, R. P. Experimental Test of Parity Conservation in Beta Decay. *Physical Review* **105,** 1413–1415 (1957).

108. Greenfield, N. J. Using circular dichroism spectra to estimate protein secondary structure. *Nature Protocols* **1,** 2876–2890 (2006).

109. Neidig, M. L., Wecksler, A. T., Schenk, G., Holman, T. R. & Solomon, E. I. Kinetic and Spectroscopic Studies of N694C Lipoxygenase: A Probe of the Substrate Activation Mechanism of a Nonheme Ferric Enzyme. *Journal of the American Chemical Society* **129,** 7531–7537 (2007).

110. Solomon, E. I. & Lever, A. B. P. *Inorganic Electronic Structure and Spectroscopy, Volume I: Methodology.* ISBN: 978-0-471-97124-5 (Wiley, New York, 2006).

111. Berova, N., Nakanishi, K. & Woody, R. W. *Circular Dichroism: Principles and Applications.* ISBN: ISBN: 978-0-471-33003-5 (Wiley, New York, 2000).

112. Janssen, M. H. M. & Powis, I. Detecting chirality in molecules by imaging photoelectron circular dichroism. *Physical Chemistry Chemical Physics* **16,** 856–871 (2014).

113. Rhee, H. *et al.* Femtosecond characterization of vibrational optical activity of chiral molecules. *Nature* **458,** 310–313 (2009).

114. Tang, Y. & Cohen, A. E. Enhanced Enantioselectivity in Excitation of Chiral Molecules by Superchiral Light. *Science* **332,** 333–336 (2011).

115. Busch, K. & Busch, M. *Chiral Analysis.* ISBN: 9780444516695 (Elsevier, Amsterdam, 2006).

116. Bougas, L., Katsoprinakis, G. E., von Klitzing, W., Sapirstein, J. & Rakitzis, T. P. Cavity-Enhanced Parity-Nonconserving Optical Rotation in Metastable Xe and Hg. *Physical Review Letters* **108,** 210801 (2012).

117. Bougas, L., Katsoprinakis, G. E., von Klitzing, W. & Rakitzis, T. P. Fundamentals of cavity-enhanced polarimetry for parity-nonconserving optical rotation measurements: Application to Xe, Hg, and I. *Physical Review A* **89,** 052127 (2014).

118. Sofikitis, D. *et al.* Evanescent-wave and ambient chiral sensing by signal-reversing cavity ringdown polarimetry. *Nature* **514,** 76–79 (2014).

119. Durand, M., Morville, J. & Romanini, D. Shot-noise-limited measurement of sub–parts-per-trillion birefringence phase shift in a high-finesse cavity. *Physical Review A* **82,** 031803 (2010).

120. Bougas, L. *et al.* Chiral cavity ring down polarimetry: Chirality and magnetometry measurements using signal reversals. *The Journal of Chemical Physics* **143,** 104202 (2015).

121. Lan, S. & Hossein-Zadeh, M. Faraday Effect in High-Q Whispering-Gallery Mode Optical Cavities. *IEEE Photonics Journal* **3,** 872–880 (2011).

122. Oraevsky, A. N. Whispering-gallery waves. *Quantum Electronics* **32,** 377–400 (2002).

123. Vahala, K. J. Optical microcavities. *Nature* **424,** 839–846 (2003).

124. Rokhsari, H., Kippenberg, T. J., Carmon, T. & Vahala, K. J. Radiation-pressure-driven micro-mechanical oscillator. *Optics Express* **13,** 5293–5301 (2005).

125. Ma, L. *et al.* Tuning of optical resonances in asymmetric microtube cavities. *Optics Letters* **36,** 3840–3842 (2011).

126. Gil-Santos, E. *et al.* Scalable high-precision tuning of photonic resonators by resonant cavity-enhanced photoelectrochemical etching. *Nature Communications* **8,** 14267 (2017).

127. Von Klitzing, W., Long, R., Ilchenko, V. S., Hare, J. & Lefèvre-Seguin, V. Frequency tuning of the whispering-gallery modes of silica microspheres for cavity quantum electrodynamics and spectroscopy. *Optics Letters* **26,** 166–168 (2001).

128. Rezac, J. & Rosenberger, A. Locking a microsphere whispering-gallery mode to a laser. *Optics Express* **8,** 605–610 (2001).

129. Ioppolo, T. & Ötügen, M. V. Pressure tuning of whispering gallery mode resonators. *Journal of the Optical Society of America B* **24,** 2721–2726 (2007).

130. Pöllinger, M., O'Shea, D., Warken, F. & Rauschenbeutel, A. Ultrahigh-Q Tunable Whispering-Gallery-Mode Microresonator. *Physical Review Letters* **103,** 053901 (2009).

131. Rabiei, P., Steier, W., Zhang, C. & Dalton, L. Polymer micro-ring filters and modulators. *Journal of Lightwave Technology* **20,** 1968–1975 (2002).

132. Savchenkov, A., Ilchenko, V., Matsko, A. & Maleki, L. Tunable filter based on whispering gallery modes. *Electronics Letters* **39,** 389–391 (2003).

133. Fang, Z. *et al.* Real-time electrical tuning of an optical spring on a monolithically integrated ultrahigh Q lithium nibote microresonator. *Optics Letters* **44,** 1214–1217 (2019).

134. Ward, J. M. & Chormaic, S. N. Thermo-optical tuning of whispering gallery modes in Er:Yb co-doped phosphate glass microspheres. *Applied Physics B* **100,** 847–850 (2010).

135. Liu, Y. *et al.* All-optical tuning of a magnetic-fluid-filled optofluidic ring resonator. *Lab on a Chip* **14,** 3004–3010 (2014).

136. Xu, L. *et al.* High-Q silk fibroin whispering gallery microresonator. *Optics Express* **24,** 20825–20830 (2016).

137. Shi, L., Zhu, T., Huang, D. & Liu, M. Thermo–Optic Tuning of Integrated Polymethyl Methacrylate Sphere Whispering Gallery Mode Resonator. *IEEE Photonics Journal* **8,** 2701307 (2016).

138. Lee, B. S. *et al.* On-chip thermo-optic tuning of suspended microresonators. *Optics Express* **25,** 12109–12120 (2017).

139. Lu, T. *et al.* High sensitivity nanoparticle detection using optical microcavities. *Proceedings of the National Academy of Sciences* **108,** 5976–5979 (2011).

140. Kim, E., Foreman, M. R., Baaske, M. D. & Vollmer, F. Thermal characterisation of (bio)polymers with a temperature-stabilised whispering gallery mode microsensor. *Applied Physics Letters* **106,** 161101 (2015).

141. Forstner, S. *et al.* Cavity Optomechanical Magnetometer. *Physical Review Letters* **108,** 120801 (2012).

142. Forstner, S. *et al.* Ultrasensitive Optomechanical Magnetometry. *Advanced Materials* **26,** 6348–6353 (2014).

143. Lin, W. *et al.* Laser-tuned whispering gallery modes in a solid-core microstructured optical fibre integrated with magnetic fluids. *Scientific Reports* **5,** 17791 (2015).

144. Mahmood, A. *et al.* Magnetic field sensing using whispering-gallery modes in a cylindrical microresonator infiltrated with ferronematic liquid crystal. *Optics Express* **25,** 12195–12202 (2017).

145. Haigh, J. A. *et al.* Magneto-optical coupling in whispering-gallery-mode resonators. *Physical Review A* **92,** 063845 (2015).

146. Osada, A. *et al.* Cavity Optomagnonics with Spin-Orbit Coupled Photons. *Physical Review Letters* **116,** 223601 (2016).

147. Zhang, X., Zhu, N., Zou, C.-L. & Tang, H. X. Optomagnonic Whispering Gallery Microresonators. *Physical Review Letters* **117,** 123605 (2016).

148. Dillon, J. F., Remeika, J. P. & Staton, C. R. Linear Magnetic Birefringence in Cubic Magnetic Crystals. *Journal of Applied Physics* **40,** 1510–1511 (1969).

149. Povinelli, M. L. *et al.* High-Q enhancement of attractive and repulsive optical forces between coupled whispering-gallery-mode resonators. *Optics Express* **13,** 8286–8295 (2005).

150. Vandendriessche, S. *et al.* Giant Faraday Rotation in Mesogenic Organic Molecules. *Chemistry of Materials* **25,** 1139–1143 (2013).

151. Rodgers, C. T. & Hore, P. J. Chemical magnetoreception in birds: The radical pair mechanism. *Proceedings of the National Academy of Sciences* **106,** 353–360 (2009).

152. Lipkin, D. M. Existence of a New Conservation Law in Electromagnetic Theory. *Journal of Mathematical Physics* **5,** 696–700 (1964).

153. Gansel, J. K. *et al.* Gold Helix Photonic Metamaterial as Broadband Circular Polarizer. *Science* **325,** 1513–1515 (2009).

154. Gansel, J. K. *et al.* Tapered gold-helix metamaterials as improved circular polarizers. *Applied Physics Letters* **100,** 101109 (2012).

155. Hendry, E. *et al.* Ultrasensitive detection and characterization of biomolecules using superchiral fields. *Nature Nanotechnology* **5,** 783–787 (2010).

156. Zhao, R., Zhang, L., Zhou, J., Koschny, T. & Soukoulis, C. M. Conjugated gammadion chiral metamaterial with uniaxial optical activity and negative refractive index. *Physical Review B* **83,** 035105 (2011).

157. Yin, X., Schäferling, M., Metzger, B. & Giessen, H. Interpreting Chiral Nanophotonic Spectra: The Plasmonic Born–Kuhn Model. *Nano Letters* **13,** 6238–6243 (2013).

158. Guerrero-Martınez, A. *et al.* Intense Optical Activity from Three-Dimensional Chiral Ordering of Plasmonic Nanoantennas. *Angewandte Chemie International Edition* **50,** 5499–5503 (2011).

159. Querejeta-Fernández, A., Chauve, G., Methot, M., Bouchard, J. & Kumacheva, E. Chiral Plasmonic Films Formed by Gold Nanorods and Cellulose Nanocrystals. *Journal of the American Chemical Society* **136,** 4788–4793 (2014).

160. Shen, X. *et al.* Rolling Up Gold Nanoparticle-Dressed DNA Origami into Three-Dimensional Plasmonic Chiral Nanostructures. *Journal of the American Chemical Society* **134,** 146–149 (2011).

161. Kuzyk, A. *et al.* DNA-based self-assembly of chiral plasmonic nanostructures with tailored optical response. *Nature* **483,** 311–314 (2012).

162. Kim, E., Baaske, M. D. & Vollmer, F. In Situ Observation of Single-Molecule Surface Reactions from Low to High Affinities. *Advanced Materials* **28,** 9941–9948 (2016).

163. Kim, E., Baaske, M. D., Schuldes, I., Wilsch, P. S. & Vollmer, F. Label-free optical detection of single enzyme-reactant reactions and associated conformational changes. *Science Advances* **3,** e1603044 (2017).

164. Hammouda, B. Temperature Effect on the Nanostructureof SDS Micelles in Water. *Journal of Research of the National Institute of Standards and Technology* **118,** 151–167 (2013).

165. Elson, E. Fluorescence Correlation Spectroscopy: Past, Present, Future. *Biophysical Journal* **101,** 2855–2870 (2011).

166. Lerner, E. *et al.* Toward dynamic structural biology: Two decades of single-molecule Förster resonance energy transfer. *Science* **359,** eaan1133 (2018).

167. Hillmering, M. *et al.* Off-stoichiometry improves the photostructuring of thiol–enes through diffusion-induced monomer depletion. *Microsystems & Nanoengineering* **2,** 15043 (2016).

168. McBride, M. K. *et al.* A readily programmable, fully reversible shape-switching material. *Science Advances* **4,** eaat4634 (2018).

169. Pulcu, G. S., Mikhailova, E., Choi, L.-S. & Bayley, H. Continuous observation of the stochastic motion of an individual small-molecule walker. *Nature Nanotechnology* **10,** 76–83 (2014).

170. Kassem, S. *et al.* Artificial molecular motors. *Chemical Society Reviews* **46,** 2592–2621 (2017).

171. Pensa, E. *et al.* The Chemistry of the Sulfur–Gold Interface: In Search of a Unified Model. *Accounts of Chemical Research* **45,** 1183–1192 (2012).

172. Zhou, C., Duan, X. & Liu, N. A plasmonic nanorod that walks on DNA origami. *Nature Communications* **6,** 8102 (2015).

173. Betz, S. F. Disulfide bonds and the stability of globular proteins. *Protein Science* **2,** 1551–1558 (1993).

174. Carl, P., Kwok, C. H., Manderson, G., Speicher, D. W. & Discher, D. E. Forced unfolding modulated by disulfide bonds in the Ig domains of a cell adhesion molecule. *Proceedings of the National Academy of Sciences* **98,** 1565–1570 (2001).

175. Song, J., Yuan, Z., Tan, H., Huber, T. & Burrage, K. Predicting disulfide connectivity from protein sequence using multiple sequence feature vectors and secondary structure. *Bioinformatics* **23,** 3147–3154 (2007).

176. Winterbourn, C. C. & Hampton, M. B. Thiol chemistry and specificity in redox signaling. *Free Radical Biology and Medicine* **45,** 549–561 (2008).

177. Fu, X. *et al.* Cysteine Disulfides (Cys-ss-X) as Sensitive Plasma Biomarkers of Oxidative Stress. *Scientific Reports* **9,** 115 (2019).

178. Winther, J. R. & Thorpe, C. Quantification of thiols and disulfides. *Biochimica et Biophysica Acta (BBA) - General Subjects* **1840,** 838–846 (2014).

179. Rahman, I., Kode, A. & Biswas, S. K. Assay for quantitative determination of glutathione and glutathione disulfide levels using enzymatic recycling method. *Nature Protocols* **1,** 3159–3165 (2006).

180. Foreman, M. R. & Vollmer, F. Theory of resonance shifts of whispering gallery modes by arbitrary plasmonic nanoparticles. *New Journal of Physics* **15,** 083006 (2013).

181. Foreman, M. R. & Vollmer, F. Level repulsion in hybrid photonic-plasmonic microresonators for enhanced biodetection. *Physical Review A* **88,** 023831 (2013).

182. Klusmann, C., Suryadharma, R. N. S., Oppermann, J., Rockstuhl, C. & Kalt, H. Hybridizing whispering gallery modes and plasmonic resonances in a photonic metadevice for biosensing applications [Invited]. *Journal of the Optical Society of America B* **34,** D46–D55 (2017).

183. Lu, T., Su, T.-T. J., Vahala, K. J. & Fraser., S. E. *US Patent* 8593638 (2013).

184. Leff, D. V., Brandt, L. & Heath, J. R. Synthesis and Characterization of Hydrophobic, Organically-Soluble Gold Nanocrystals Functionalized with Primary Amines. *Langmuir* **12,** 4723–4730 (1996).

185. Pong, B.-K., Lee, J.-Y. & Trout, B. L. First Principles Computational Study for Understanding the Interactions between ssDNA and Gold Nanoparticles: Adsorption of Methylamine on Gold Nanoparticulate Surfaces. *Langmuir* **21,** 11599–11603 (2005).

186. Venkataraman, L. *et al.* Single-Molecule Circuits with Well-Defined Molecular Conductance. *Nano Letters* **3,** 458–462 (2006).

187. Kim, Y., Hellmuth, T. J., Bürkle, M., Pauly, F. & Scheer, E. Characteristics of Amine-Ended and Thiol-Ended Alkane Single-Molecule Junctions Revealed by Inelastic Electron Tunneling Spectroscopy. *ACS Nano* **5,** 4104–4111 (2011).

188. Xie, H.-J., Lei, Q.-F. & Fang, W.-J. Intermolecular interactions between gold clusters and selected amino acids cysteine and glycine: a DFT study. *Journal of Molecular Modeling* **18,** 645–652 (2011).

189. Nelson, J. W. & Creighton, T. E. Reactivity and Ionization of the Active Site Cysteine Residues of DsbA, a Protein Required for Disulfide Bond Formation in vivo. *Biochemistry* **33,** 5974–5983 (1994).

190. O'Neil, M. J. *The Merck Index* 15th edn (Royal Society of Chemistry, Cambridge, 2013).

191. Serjeant, E. P. & Dempsey, B. *Ionisation constants of organic acids in aqueous solution* (Pergamon Press, Oxford/New York, 1979).

192. Jin, W. & Chen, H. A new method of determination of diffusion coefficients using capillary zone electrophoresis (peak-height method). *Chromatographia* **52,** 17–21 (2000).

193. Mauranyapin, N. P., Madsen, L. S., Taylor, M. A., Waleed, M. & Bowen, W. P. Evanescent single-molecule biosensing with quantum-limited precision. *Nature Photonics* **11,** 477–481 (2017).

194. Ding, H. *et al.* Gold Nanorods Coated with Multilayer Polyelectrolyte as Contrast Agents for Multimodal Imaging. *The Journal of Physical Chemistry C* **111,** 12552–12557 (2007).

195. Pakiari, A. H. & Jamshidi, Z. Interaction of Amino Acids with Gold and Silver Clusters. *The Journal of Physical Chemistry A* **111,** 4391–4396 (2007).

196. Vincent, S. *Full-Vector Finite Dierence Mode Solver for Whispering-Gallery Resonators* MA thesis (University of Victoria, 2015).

197. Srinivasan, K., Borselli, M., Painter, O., Stintz, A. & Krishna, S. Cavity Q, mode volume, and lasing threshold in small diameter AlGaAs microdisks with embedded quantum dots. *Optics Express* **14,** 1094 (2006).

198. Ruan, Y. *et al.* Atom–Photon Coupling from Nitrogen-vacancy Centres Embedded in Tellurite Microspheres. *Scientific Reports* **5,** 11486 (2015).

199. Ruan, Y. *et al.* Magnetically sensitive nanodiamond-doped tellurite glass fibers. *Scientific Reports* **8,** 1268 (2018).